To the Graduate Council:

I am submitting herewith a dissertation written by Xiaohang Peng entitled "Particle Simulation of Grid Erosion in an Ion Thruster."I have examined the final copy of this dissertation for form and content and recommend that it be accepted in partial fulfillment of the requirements for the degree of Doctor of Philosophy, with a major in Mechanical Engineering.

Dennis Keefer, Major Professor

We have read this dissertation
and recommend its acceptance:

Accepted for the Council:

Vice Provost
and Dean of the Graduate School

PARTICLE SIMULATION OF GRID EROSION IN AN ION THRUSTER

A Dissertation

Presented for the

Doctor of Philosophy

Degree

The University of Tennessee, Knoxville

Xiaohang Peng

December 1991

To My Beloved

Grandmother

ACKNOWLEDGMENTS

The author is especially grateful to his major professor, Dr. Dennis Keefer, for his direction, and for his advice, encouragement, and invaluable help throughout the course of this study.

The author is also grateful to the other committee members, Drs. G. W. Garrison, T. D. McCay, R. A. Crawford, F. G. Collins, and B. A. Kupershmidt, for their comments on the manuscript.

Special gratitude is expressed to Dr. Wim M. Ruyten, for his many valuable suggestions during the code development and his constructive criticism towards the completion of this dissertation. Also, the cordial assistance provided by other UTSI and CSTAR staff is gratefully acknowledged.

The author would like to give special thanks to his wife, Quan, for her support, encouragement, patient, and love, and to his two children, Mong-Mong and Aaron.

The work reported herein was jointly supported by Boeing Defense & Space Group, Seattle, WA (grant monitor Dr. J. S. Meserole), and the University of Tennessee–Calspan Center for Space Transportation and Applied Research under NASA Grant NAGW-1195. The author would like to thank Dr. George W. Garrison for providing him with the opportunity to work on this project.

ABSTRACT

A particle simulation computational code has been developed to study the effect of charge-exchange-induced grid erosion in electron bombardment ion thrusters. The code is based on the particle-in-cell (PIC) method to simulate the ion flow and a Monte Carlo method to calculate the charge exchange collisions. Both two- and three-dimensional versions of this code have been developed. The two-dimensional model provides a qualitative description of the details of the ion flow and the charge exchange collisions. The three-dimensional version has successfully predicted the experimentally observed erosion pattern in which the maximum erosion occurs at the geometric centers of accelerator grid apertures.

TABLE OF CONTENTS

LIST OF FIGURES

LIST OF SYMBOLS

$\hat{a}$	normal vector
A	area
$\mathbf{B}$	magnetic induction
c	speed of light
e	electronic charge
$\mathbf{E}$	electric field
$\mathbf{F}$	body force
I_{sp}	specific impulse
j	current density
$\mathbf{j}$	electric current vector
k	Bolzmann's constant
m	mass
n_e	electron number density
n_i	ion number density
$p(t)$	probability density function
q	charge
r	radius
R	flux
r, z	spatial cylindrical coordinates
S	PIC shape function
T	temperature
u, v	velocity components
$\mathbf{v}$	velocity vector
x, y, z	spatial Cartesian coordinates

ϵ_0	dielectric constant
μ_0	magnetic permeability
ν	collision frequency
ρ	charge density
σ	collision cross-section
ϕ	electric potential

Subscripts

e	electron
e	exit plane
i	ion
0	neutral plasma
p	particle
r, z	coordinate directions
t	transverse direction

CHAPTER I

INTRODUCTION

Essentially all space vehicles are launched from the earth's surface by chemical rockets because of their high thrust. Chemical rockets are characterized as *energy-limited* devices since the energy required to accelerate the rockets comes from the on-board propellant and the attainable vehicle kinetic energy is limited by the energy released in chemical reactions. In other words, the specific impulse of chemical rockets is limited to about 450 sec because of the strength of the chemical bonds of the propellants (Oates 1984 and Hill and Peterson 1965).

For those lengthy and/or very high energy missions such as orbit transfer from low Earth orbit (LEO) to geosynchronous Earth orbit (GEO), interplanetary flights, and station keeping and attitude control of synchronous satellites, the required fraction of propellant mass to overall vehicle mass using chemical propulsion becomes excessive. Since electrical propulsion provides higher specific impulse and, therefore, low mass ratios (defined as initial mass divided by final mass), it has a weight advantage over chemical propulsion in those missions mentioned above.

Electrical propulsion devices convert electrical energy developed from either nuclear or solar generators into directed kinetic energy of the propellant. Electric thrusters can be generally classified into three categories, *electrothermal, electromagnetic, or electrostatic.* Different types of thrusters fit different mission profiles because of different specific impulse and thrust. For example, arcjets can produce a specific impulse (I_{sp}) up to about 1500 sec with a thrust greater than 1 newton. Arcjets, in the available ranges of specific impulse and thrust, are suited for station keeping and orbit transfer.

Electrostatic thrusters can have specific impulses in the 2,000 to 10,000 sec range, but at very low thrust level. These devices are best suited for interplanetary missions. Electrostatic thrusters achieve vehicle acceleration by the interaction of electrostatic fields with the charged propellant particles. The electron bombardment ion thruster is one of these thrusters presently under development. It is the subject of this dissertation and will be discussed in more detail in section **1.2**.

1.1. About the Topic

Ion propulsion inherently provides low thrust and therefore low vehicle acceleration ($\sim 10^{-4}$ to $10^{-5}g$), with high specific impulse ($\sim$2,000 to 10,000 sec). This propulsion system is best suited for lengthy missions such as the heliocentric portion of interplanetary flights (Brewer 1970). Kaufman and Robinson (1984) and Rawlin and Patterson (1985) also indicated that ion thrusters are an excellent candidate for orbit-raising applications. Ion thrusters also can be used for station keeping and attitude control of synchronous satellites. The missions that ion thrusters could accomplish strongly imply that the ion propulsion system have long life (more than 10,000 hours). Therefore, the engine lifetime is one of the critical issues for applications of ion propulsion.

A recent xenon ion thruster lifetime experiment conducted at NASA Lewis Research Center (Patterson and Verhey 1990) has shown that accelerator grid erosion poses the most likely limitation to ion engine lifetime. During the test, the accelerator grid suffered a mass loss of 17.759 gm $\pm$ 0.004 gm over the 956.8 hour test period, and erosion pits penetrated the entire thickness of the molybdenum accelerator grid (0.36 mm) at the geometric centers between apertures. It has been well established that such grid erosion is due to charge exchange collisions between fast beam ions and slow neutral propellant atoms (Brewer 1970). The charge

exchange process leading to this grid erosion is sensitive to background neutral densities and downstream plasma conditions, both of which may be substantially different in space operation than those in ground tests. Therefore, it is difficult to estimate accurate effective lifetimes for space operation from such ground tests. Furthermore, because lifetime testing is long and expensive, parametric studies are not usually affordable.

In order to facilitate the interpretation of ground tests and to aid in the extrapolation from ground test results to space conditions, it would be desirable to have a detailed analytical model to simulate the sputtering of the accelerator grid in an ion thruster. Because of the low density and the small rate of charge exchange collisions in an ion thruster, a direct particle simulation numerical method with a microscopic Monte Carlo model for charge exchange collisions is a proper way to approach this problem.

The objective of this dissertation is, therefore, to develop an analytical model based on a particle method to simulate these erosion processes.

1.2. Background

1.2.1. The Ion Thruster

Electrostatic ion thrusters are characterized by the separate acceleration of positive and negative charges. Therefore this class of electric thruster must include means for ionizing the propellant atoms, a means for accelerating the ions by electric fields, and a way to neutralize the ion beams after these ions have been accelerated to the desired exhaust velocity. To accomplish this, the thruster includes an ion source, an ion accelerator system, and a neutralizer. The electron bombardment ion thruster is shown schematically in Fig. 1.1. The propellant is

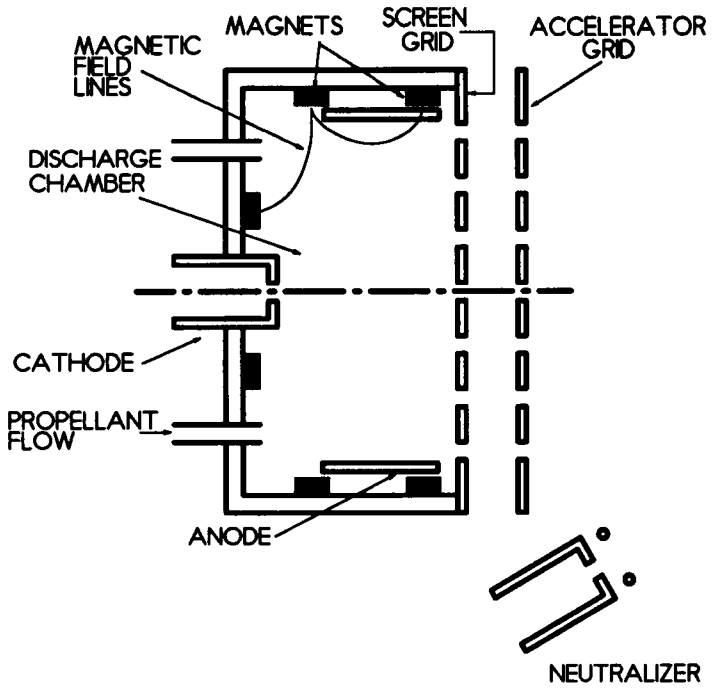

Figure 1.1. Ion Thruster Schematic.

introduced into one end of the discharge chamber and the ions are extracted by the accelerator grid system from the other end of the discharge chamber. During thruster operation, neutral propellant gas is injected into the discharge chamber and electrons are emitted by the hollow cathode. These electrons, which are called primary electrons, are accelerated by an electric field and as the electrons strike the atoms of the propellant gas, the particles are ionized and the electrons lose energy. Since the mean free path for ionization is much larger than the dimensions of the discharge chamber, an applied magnetic field is used to restrict the direct access of primary electrons to the anode without first having had inelastic collisions with neutral propellant atoms. The ionized particles thus form a neutral plasma which essentially fills the discharge chamber.

At the downstream end of the discharge chamber, two electrodes (two-grid system) are used to extract the ions from the discharge chamber plasma to form an ion beam. The inner electrode is referred to as the screen grid and the outer one is called the accelerator grid. There exists a plasma sheath region between the plasma and the screen grid from which the ions are extracted from the plasma and subsequently accelerated through the grid apertures by the applied negative potential on the accelerator grid. At the same time, the electrons will be retarded by the screen grid surface. Electrons are injected into the positive ion beam by a neutralizer positioned downstream of the accelerator grid in order to neutralize the ion beam.

In this study, only the accelerator system is simulated.

1.2.2. Charge-Exchange Ion Erosion

The ion thruster will always have some neutral propellant gas flowing out through the grid apertures. These neutral propellant atoms may undergo charge exchange collisions with the beam ions throughout the beam flow region. This charge exchange collision process transforms high velocity ions into high velocity neutral atoms, and low velocity neutrals into low velocity ions (charge-exchange ions) which assume the neutral gas thermal velocity. If these charge-exchange (CE) ions are produced in the negative potential region downstream of the accelerator grid, they are largely attracted to the most negative electrode of the thruster. In the usual electrode potential configuration, this is the accelerator grid. Fig. 1.2 shows schematically the trajectories of charge exchange ions created in the downstream region of the accelerator grid. These charge-exchange ions give rise to sputtering erosion of the accelerator grid and provide a limitation on the life expectancy of this grid.

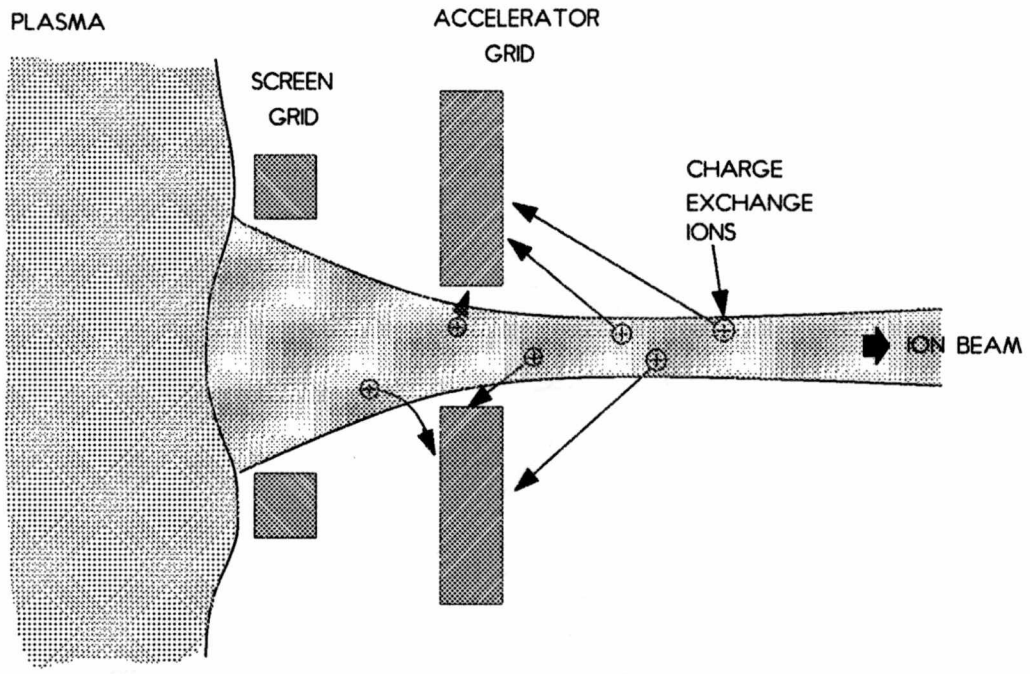

Figure 1.2. Illustration of the trajectories of charge exchange ions.

In the case of ground testing, charge exchange collisions may occur not only between beam ions and neutral propellant atoms but also with atoms of the residual gas in the test facility. The charge exchange sputtering erosion observed in the ground tests depends to a significant extent on the neutral background density of residual gas in the test facility.

1.2.3. Literature Review

It has long been realized that accelerator grid erosion by charge exchange ions might be the most serious and fundamental life limitation for ion engines (Patterson and Verhey, 1990, Brewer, 1970 and Pawlik and Reader, 1967). To quantify such erosion, a number of experimental studies have been conducted

recently for ion thrusters operating on xenon propellant (Patterson and Verhey, 1990, Rawlin, 1988, and Patterson, 1986). Similar studies have been conducted previously on earlier thrusters which operated with mercury propellant (Pawlik and Reader, 1967, King et al. 1967 and 1966, Maloy et al., 1981, Beattie, 1979, and Rawlin and Mantenieks, 1978). For a two-grid accelerator system, the erosion pattern is similar for ion thrusters operating on either xenon or mercury; the maximum erosion sputtering occurs at the geometric centers between apertures (Pawlik and Reader, 1967 and Patterson and Verhey, 1990).

Many electron-bombardment ion thruster systems have been designed using empirical techniques (Kerslake 1962; Kerslake and Pawlik 1963; Kaufman 1965). Since this early work, various analog techniques (Hollway 1965; Loukochkov 1956; Van Duzer and Brewer 1959; Staggs 1965) and digital computer programs (Hamza and Richley 1962; Kirstein and Hornsby 1963; Hamza 1963; Bogart and Richley 1966) have become available to aid in the accelerator system design. Both approaches solve essentially the same problem but differ considerably in the method of solution. Each method offers certain advantages over the other, and each is subject to certain limitations.

Briefly, the computer simulation method, developed in the 1960s (Hamza and Richley 1962; Hamza 1963; Bogart and Richley 1966) was used to express Poisson's equation in finite difference form at computational mesh points. The simulation procedure begins by solving the Laplace equation. Then iterations are employed to obtain local values of current density j and ion speed v, which in turn are used to provide estimates of the local space charge density ρ ($\rho = j/v$). Final iterative procedures then yield the solution to Poisson's equation.

For the electrolytic tank analog method, simulation of an ion accelerator system is accomplished by placing a scale-model in a tray which is filled with tap

water that serves as the electrolyte. The simulation of the space charge of the ion beam can be made by injecting currents into the electrolyte. This technique allows the simulation of the total electric field in the accelerator region, the measurement of which provides information for the computation of the exact trajectories that ions will follow, including those created by charge-exchange collisions.

The outstanding feature of the digital computer method (Hamza and Richley 1962; Hamza 1963; Bogart and Richley 1966) is the capacity for fine detail and accuracy. The primary disadvantages compared to the analog method are computer time and a satisfactory method for dealing with charge-exchange ion trajectories. For the electrolytic tank analog method, the capacity for accuracy or fine detail is considerably less than that possible with the digital computer approach, but the unique advantage is the simplicity with which charge-exchange ion trajectories can be obtained. These two techniques were combined (Staggs, Richley and Gula 1967; Lathem 1968a,b and 1969) and became a new approach for analyzing an ion accelerator system. The salient features of both methods were used and the need for certain complex equipment formerly required with the electrolytic tank analog method was eliminated.

The computer simulation method which this study uses (Peng, Ruyten, and Keefer 1991a,b,c, and d) is different from the one described above. About 1960 Buneman and Dawson developed a method of simulating a plasma by following the motion of many particles in their own and applied fields in one dimension. After that, the field of computer plasma simulations using particles developed very fast, incorporating theories for the effects of spatial grids and temporal differencing, and in applications to instabilities and transport in fusion plasmas (Birdsall 1985; Hockney and Eastwood 1989). The advantage of this particle simulation method compared to the one developed in the 1960s and 1970s is that collisions among the

simulation particles can be directly modeled. And, because of the integral nature of the simulation code, there are no *a priori* limitations on the relative densities of primary and charge-exchange ions, and space charge effects are accounted for implicitly.

1.3. Overview

This dissertation is organized in the following manner. In Chapter **II**, the simulation problem is described and the detailed simulation methods are developed. The simulation methods include the Particle-In-Cell (PIC) method and the Monte Carlo method. In Chapter **III**, the two-dimensional axisymmetric model is presented, and sample calculations are given. In Chapter **IV**, the three-dimensional model for the usual hexagonal symmetry grid system is described. Sample calculations and comparisons between two-dimensional and three-dimensional models are discussed. Finally, the conclusions of this study are summarized in Chapter **V**.

CHAPTER II

DESCRIPTION OF THE METHOD

2.1. Problem to be Simulated

An ion engine is a plasma thruster which produces thrust by extracting ions from a plasma and subsequently focusing and accelerating the ion beams to high velocities by a negative electric potential applied to the accelerator grid. Fig. 2.1 schematically shows a portion of the two-grid accelerator system with the usual hexagonal structure of the aperture arrays. The problem with the accelerator grid system is that some of the beam ions, during this accelerating process, undergo charge-exchange collisions with neutral propellant atoms and produce slow moving "charge-exchange "(CE) ions. many of these slow CE ions are accelerated toward the accelerator grid and cause grid sputtering. This CE ion erosion process is the subject of this study. Therefore, the problem to be simulated includes the electrostatic fields, the motion of charged particles, charge exchange collisions between fast moving beam ions and slow moving neutral particles, and the accelerator grid sputtering.

In the remaining part of this section, the computational domain is discussed. Then in section **2.2** the governing equations are described, including the electric field equations and the charged particle equations of motion. In section **2.3**, the simulation methods for the electric field and charge exchange collisions are described.

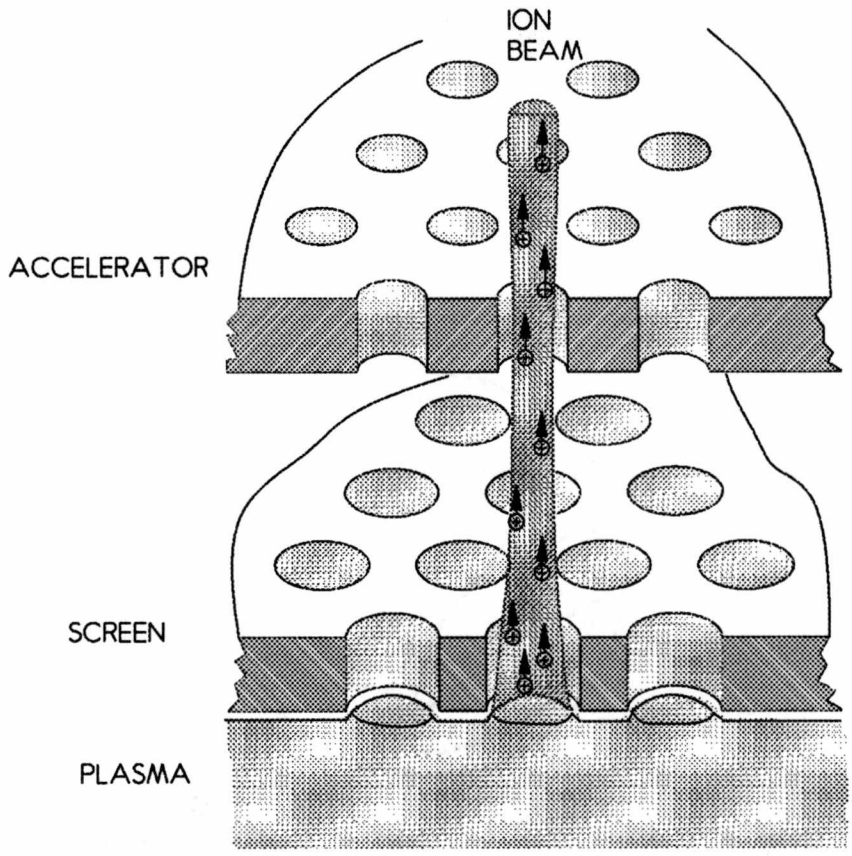

Figure 2.1. Illustration of multi-aperture accelerator system.

2.1.1. Computational Domain

There are two simulation models in this study: a two-dimensional axisymmetric model, in which a single set of screen and accelerator grid apertures is considered, and a three-dimensional model, in which the hexagonal symmetry geometry of the aperture arrays is utilized. Fig. 2.2 schematically shows the computational domain for the two-dimensional axisymmetric model which includes a neutral plasma region, an upstream plasma sheath region near the screen grid, the screen and accelerator grids, and the downstream deceleration region. This computational domain is subdivided into smaller cells with nonuniform spacing.

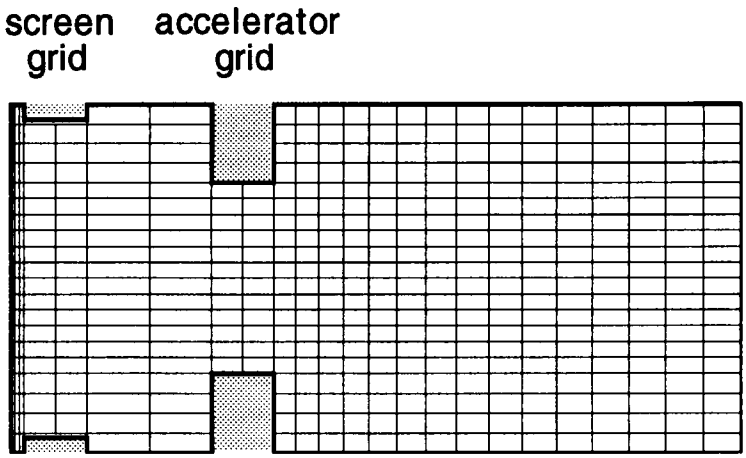

Figure 2.2. Schematic of the two-dimensional computational domain. Ion flow is from left to right.

Poisson's equation is solved at these computational mesh points.

For the three-dimensional model, rather than modeling an entire grid system, the usual hexagonal symmetry of the aperture arrays is exploited to choose as small a three-dimensional domain as is possible. Fig. 2.3a shows three apertures in such an array, and indicates the 30 degree by 60 degree right triangle that constitutes the minimum cross sectional cell of the 3D domain. Fig. 2.3b shows how this cell is subdivided into smaller triangular cells. Fig. 2.4 shows the complete wedge-shaped computational domain for the 3D model, including the screen and accelerator grid apertures. In both methods, the computational cross-section is constant along the direction of ion flow.

2.1.2. Assumptions

Upstream of the screen grid, shown in Fig. 2.1, a neutral plasma is assumed, with properties determined by the discharge chamber conditions. Ions are extracted through a plasma sheath that is formed just upstream of the screen grid. In the simulation codes, this is accomplished by thermal sampling from the plasma

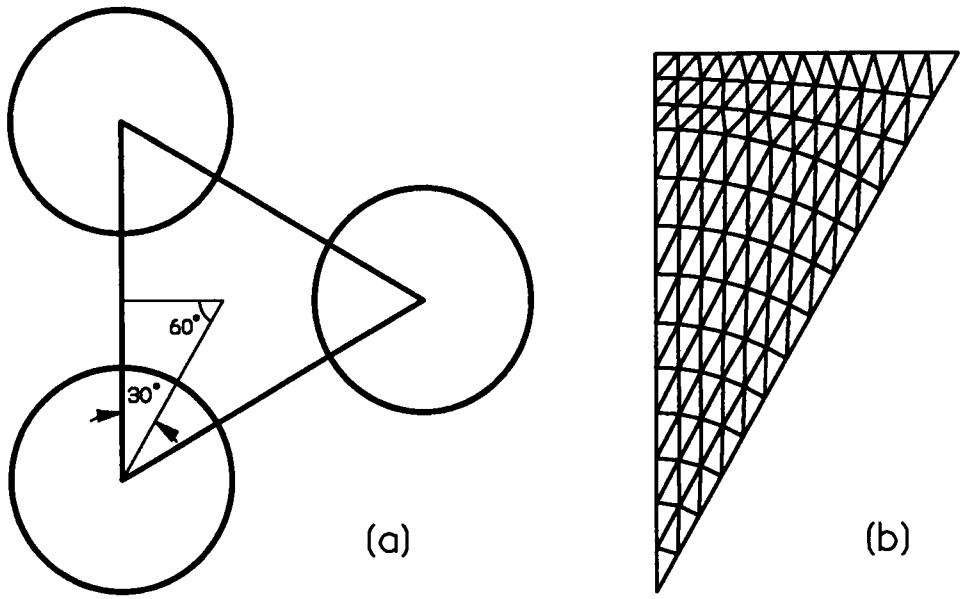

Figure 2.3. Minimum area cross-section of the three-dimensional model (a) , and the non-uniform triangular mesh in this cross-section (b).

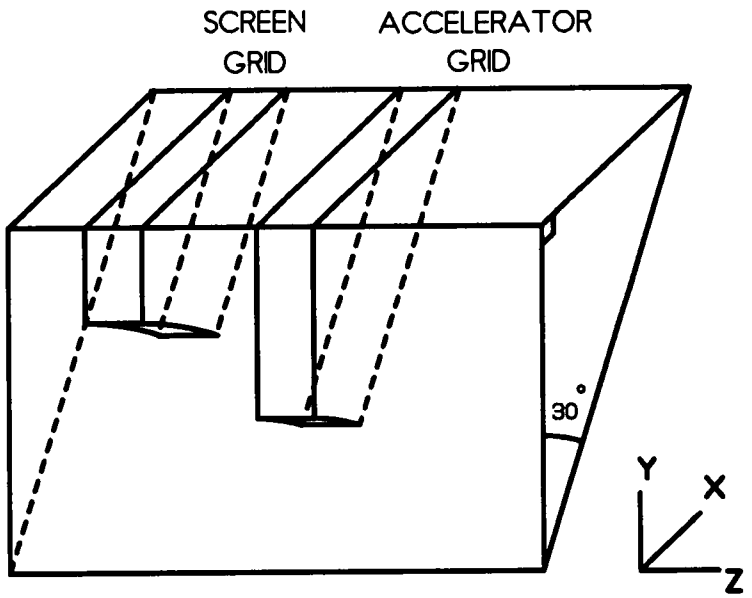

Figure 2.4. View of the complete three-dimensional domain, including screen and accelerator grid apertures.

on the far upstream surface of the computational grid. Thus, ion velocities are chosen randomly from a Maxwellian distribution at the ion temperature, with a mean extraction velocity in the axial direction. The mean extraction velocity and the initial ion density are chosen to provide the desired beam current. The particle entry positions are chosen randomly as well, but such that, on average, the ion flow has a uniform density over the computational domain. Ions then pass through the screen and accelerator grids, and reach a zero potential region, which is taken to be a plane (different downstream boundary conditions are discussed in section 3.3). This neutralization plane bounds the computational domain on the far downstream side.

To incorporate the charge exchange collisions into the simulation model, a Monte Carlo method is used to simulate the interaction between the ion beam and neutral propellant atoms. For simplicity, this background neutral gas is assumed to have a constant density throughout the computational domain.

2.2. The Equations to be Solved

2.2.1. The Field Equations

The relationships between the electric and magnetic fields ($\mathbf{E}$ and $\mathbf{B}$) and the charge and current density (ρ and $\mathbf{j}$) are given by Maxwell's equations:

$$\nabla \cdot \mathbf{B} = 0 \tag{2.1a}$$

$$\nabla \times \mathbf{B} = \mu_0 \mathbf{j} + \frac{1}{c^2} \frac{\partial \mathbf{E}}{\partial t} \tag{2.1b}$$

$$\nabla \cdot \mathbf{E} = \rho / \epsilon_0 \tag{2.1c}$$

$$\nabla \times \mathbf{E} = -\frac{\partial \mathbf{B}}{\partial t} \tag{2.1d}$$

where ϵ_0 is the dielectric constant, μ_0 is the magnetic permeability, and c is the velocity of light in free space,

$$c = (\epsilon_0 \mu_0)^{-1/2}.$$

For the electrostatic problem, Eqs.(2.1) can be reduced to:

$$\nabla \cdot \mathbf{E} = \frac{\rho}{\epsilon_0} \tag{2.2a}$$

and

$$\nabla \times \mathbf{E} = 0. \tag{2.2b}$$

Thus there exists a scalar, ϕ, such that

$$\mathbf{E} = -\nabla \phi, \tag{2.3}$$

where ϕ is called the electric potential. From Eqs.(2.2.a) and (2.3), ϕ satisfies the Poisson equation,

$$\nabla^2 \phi = -\frac{\rho}{\epsilon_0}, \tag{2.4}$$

where ρ is the charge density,

$$\rho = -e(n_i - n_e), \tag{2.5}$$

e is the magnitude of electronic charge, n_e is the electron density, and n_i is the ion density.

Eq.(2.4) is the field equation for the electrostatic problem. This equation is solved over the computational mesh by a numerical method. The discretization of this field equation is discussed in chapters **III** and **IV** for two-dimensional axisymmetric and three-dimensional (hexagonal geometry symmetry) models, respectively.

2.2.2. The Equations of Motion

The equation of motion for a single charged particle is determined from the forces acting on the particle. Only the electric field is involved in the electrostatic problem, and Newton's second law can be written as

$$m\frac{d\mathbf{v}}{dt} = q\mathbf{E}. \tag{2.6}$$

Hence, a particle motion is described by two first order differential equations, Eq.(2.6) and

$$\frac{d\mathbf{x}}{dt} = \mathbf{v}. \tag{2.7}$$

The differential equations (2.6) and (2.7) are replaced by linear algebraic relationships in the numerical simulation program. Consequently, continuous functions $\mathbf{x}$ and $\mathbf{v}$ are replaced by values at discrete time intervals. The most commonly used scheme, which is used in this model, is the finite-difference approximation leapfrog scheme, so called because it uses time-staggered centering of position and velocity (Hockney and Eastwood 1989). The leapfrog finite-difference approximation to Eqs.(2.6) and (2.7) are:

$$m\frac{\mathbf{v}^{n+1/2} - \mathbf{v}^{n-1/2}}{dt} = q\mathbf{E}(\mathbf{x}^n) \tag{2.8}$$

$$\frac{\mathbf{x}^{n+1} - \mathbf{x}^n}{dt} = \mathbf{v}^{n+1/2} \tag{2.9}$$

where dt is the time step and the superscript designates discrete time.

2.3. Simulation Methods

2.3.1. Particle In Cell Method

To obtain the charge density on the right hand side of Eq.(2.4), a particle simulation method was chosen. Currently, only ions are included as computational

particles in the simulation model. Immediate thermalization of the electron gas on the time scale of a computational time step is assumed. Furthermore, in the grid extraction region of the thruster, few electrons are present since they are repelled by the negative potential applied to the grids. However, in the ion extraction sheath formed upstream of the screen grid, the sheath structure is determined by the electron density. In this model, the electron density, n_e, is assumed to be in a Boltzmann equilibrium with the ion density n_{i_0} in the neutral plasma (Bohm 1949):

$$n_e = n_{i_0} \exp\left(- e(\phi_0 - \phi)/kT_e \right), \tag{2.10}$$

where ϕ_0 is the plasma potential, ϕ is the local potential, T_e is the electron temperature, and k is the Boltzmann constant.

The particle simulation method utilizes a large number of simulation particles whose trajectories are followed in time to simulate a plasma or ion flow. Each simulation particle carries a representative charge which is generally located within the cells defined by the computational mesh. Since the electric field equations (Eqs.(2.3) and (2.4)) are only solved at each computational mesh point but the particle positions are not located exactly at those points, the Particle-In-Cell (PIC) method is used to obtain the potentials and forces at particle positions by interpolating on the array of mesh-defined values. Mesh-defined charges are obtained by the opposite process of assigning the particle charges to nearby mesh points. These calculations are called weighting, which implies that some form of interpolation has to be used between the computational mesh points and the simulation particles. Such interpolation is governed by a particle shape factor. Generally, the particle shape factor is not defined *a priori*, and there is considerable flexibility in choosing an appropriate expression (Hockney and Eastwood 1988 and Birdsall and Langdon 1985). Usually, the requirement for these particle shape factors is

the conservation of charge. Ruyten (1991) has shown that the conservation of charge density is another reasonable requirement for the PIC weighting schemes in cylindrical and spherical coordinates. The weighting factors used in this study are discussed in chapters **III** and **IV** for the two- and three-dimensional models, respectively.

Finally, the principal steps of the PIC simulation procedure are:

1. Assign particle charges to the mesh.
2. Obtain the mesh-defined electric potentials by solving Poisson's equation (which will be discussed in Chapters **III** and **IV**).
3. Obtain the mesh-defined electric fields from the mesh-defined potentials.
4. Calculate the electric field of each simulation particle by interpolating from the mesh-defined electric fields.
5. Move each of the simulation particles. In the present study, this process is repeated until a steady state condition has been achieved. Also, at each time step, new particles are introduced from the upstream plasma sheath, and other particles exit the neutralization plane or are lost upon colliding into one of the two grids.

2.3.2. Monte Carlo Method

The purpose of the Monte Carlo method in this particle simulation code is to simulate the charge exchange collisions between ions, are moving under the influence of an electrostatic field, and neutral particles. Therefore, the simulation procedure must give the free-flight time interval between collisions and the change in the ion velocity due to the collision.

The selection of free-flight times between two collisions is considerably simplified if the collision frequency is constant. In this case, the probability of a free

flight lying between t and $t + dt$ is

$$p(t)dt = \nu \exp(-\nu t)dt, \tag{2.11}$$

where $p(t)$ is the collision probability density function and ν is a constant collision frequency.

The only problem with Eq.(2.11) is how to select a set of numbers with a given nonuniform probability density function $p(t)$ using a uniform distributed random number generator. To solve this problem, the cumulative distribution function of $p(t)$ is calculated first,

$$C(t) = \int_0^t p(t')dt'. \tag{2.12}$$

Since $C(\infty) = 1$, then

$$0 \leq C < 1, \tag{2.13}$$

and

$$dC = p(t)dt. \tag{2.14}$$

If the value of C is chosen as a random number which is uniformly distributed in the range $0 \leq C < 1$, then the probability of selecting a value in the range dC is just dC. Thus, according to Eq.(2.14), the probability of selecting a value within the range dt is $p(t)dt$. Hence, substituting dC for $p(t)dt$, Eq.(2.11) becomes,

$$dC = \nu \exp(-\nu t)dt. \tag{2.15}$$

Integrating Eq.(2.15) one obtains,

$$\begin{aligned} C(t) &= \int_0^t \nu \exp(-\nu t')dt' \\ &= 1 - \exp(-\nu t). \end{aligned} \tag{2.16}$$

Thus, the free flight time, t, is

$$t = -\nu^{-1} \ln(1 - C(t)). \tag{2.17}$$

Let

$$r = 1 - C(t); \tag{2.18}$$

then

$$t = -\nu^{-1} \ln(r), \tag{2.19}$$

where r is a random number uniformly distributed on the interval $0 < r \leq 1$.

However, since the charge exchange collision frequency is time dependent (it is energy-dependent, and, consequently, time-dependent during acceleration), the simple expression from Eq.(2.16) is not valid. To resolve this difficulty, a null collision technique (Skullerud 1968) is introduced. In this concept, a null collision frequency is defined, such that the sum of the real (energy-dependent) collision frequency and the (also energy-dependent) null collision frequency adds to a constant (that is, energy-independent) collision frequency ν:

$$\nu_{null} = \nu - \nu_{real}. \tag{2.17}$$

Thus, Eq.(2.11) can be used after all, and Eq.(2.17) determines the distribution of collisions between real collisions and null collisions. The simulation procedure now is, first of all, to choose a random number r_1 which determines a free flight time according to Eq.(2.15). Then, the particle is allowed to move to a new position under the influence of the electric field. At the new position, the real collision frequency ν_{real} is calculated:

$$\nu_{real} = nv\sigma(v), \tag{2.18}$$

where n is the neutral density, v is the relative velocity, and σ is the cross-section of the charge exchange collision (Hasted 1964), given by

$$\sigma(v) = \sqrt{a - b\ln(v^2)}, \tag{2.19}$$

where a and b are constants.

Next, a second random number r_2 is chosen. If

$$r_2 > \frac{\nu_{real}}{\nu} \tag{2.20}$$

the event is assumed to be in the null collision regime (Fig. 2.5), and no change occurs. Otherwise, the collision is counted as a real charge exchange and a new slow ion is added to the test particles at this location, with a randomly chosen thermal velocity. The charge exchange rate for xenon, as a function of ion velocity, was obtained from Hasted (1964), and is plotted in Fig. 2.5.

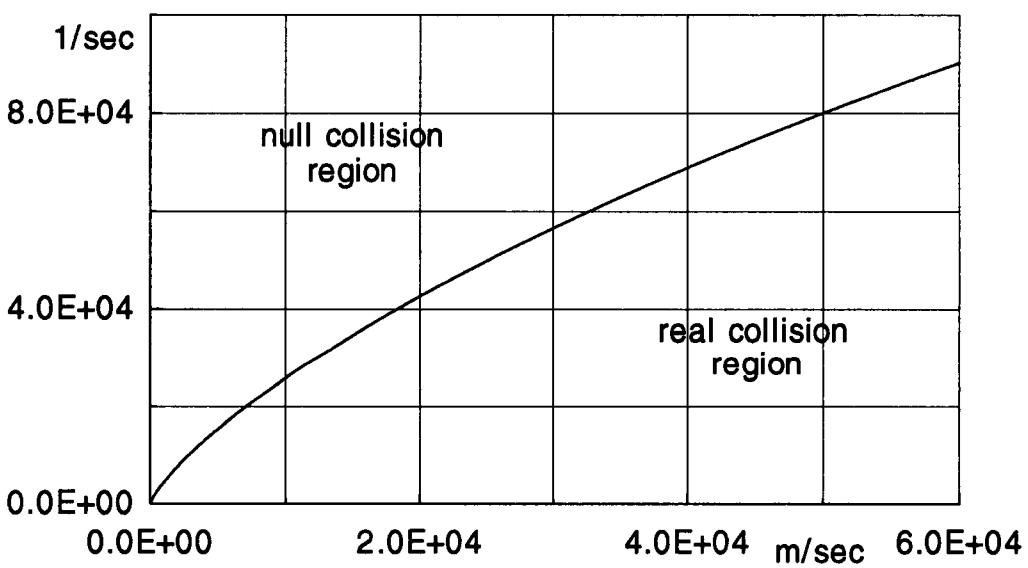

Figure 2.5. Xenon-xenon charge exchange rate as a function of relative collision velocity for a background neutral density of $5 \times 10^{18} m^{-3}$ (from Hasted, *Physics of Atomic Collisions*, 1964).

Sputtering rates for xenon ions impinging on a molybdenum surface where obtained from a General Mill's Report (1962), and are shown in Fig. 2.6. It is assumed that this sputtering is independent of the angle of incidence of the ion.

These simulation methods are incorporated in the two and three dimensional computer codes described in Chapters **III** and **IV**.

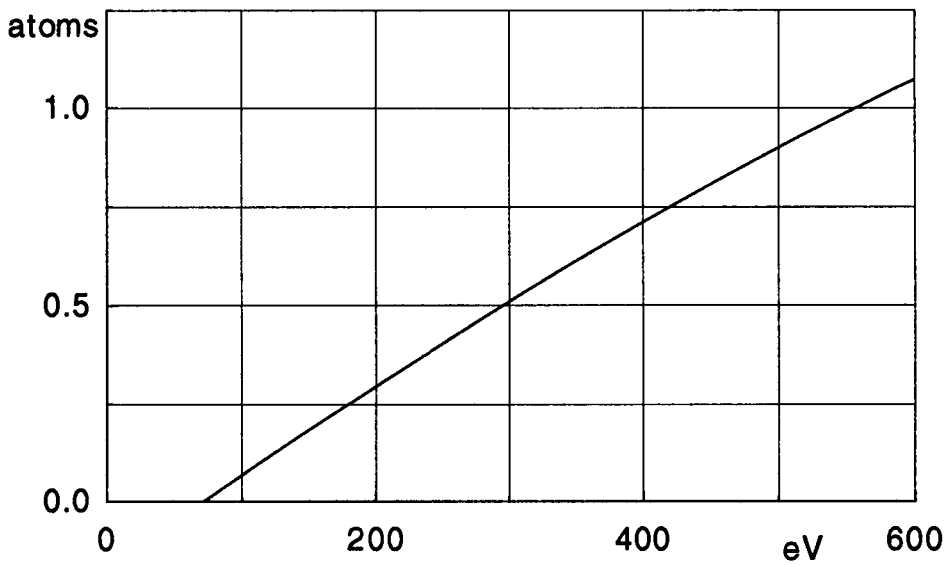

Figure 2.6. Molybdenum sputtering rate (in atoms per impacting ion) as a function of the incident kinetic energy of the xenon ions (from General Mill's Report, 1962).

CHAPTER III

TWO-DIMENSIONAL AXISYMMETRIC MODEL

The two-dimensional axisymmetric model was developed to simulate a single set of apertures in an accelerator grid system. The two-dimensional model does not produce a quantitative measure for the grid erosion in a grid system consisting of an array of apertures with the usual hexagonal symmetry geometry; however, it can provide insight into the erosion processes including ion flow, charge exchange collisions, and grid sputtering. The two-dimensional model solves the electric field equation, Eq.(2.4), and the charged particle dynamic equations. A charged particle may experience charge exchange collisions with neutral particles during its motion as discussed in Chapter **II**. This chapter discusses the solution of the Poisson field equation, Eq.(2.4), for a two-dimensional axisymmetric geometry with cylindrical coordinates. The discretization of Poisson's equation for the two-dimensional axisymmetric geometry with cylindrical coordinates is discussed in section **3.1**. The PIC weighting factor in cylindrical coordinates is described in section **3.2**. Then, calculations performed with and without consideration of charge exchange collisions are given in section **3.3**. Finally, some conclusions based on the two-dimensional model are given in section **3.4**.

3.1. Discretization of Poisson's Equation

Poisson's equation is solved at each computational mesh point shown in Fig. 2.2. Each of those mesh points, (j, k), has an associated volume element as shown in Fig. 3.1 by the dashed lines. Gauss' law is applied to these volume elements to guarantee flux conservation.

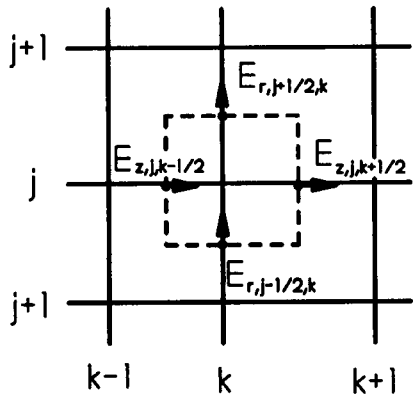

Figure 3.1. Two-dimensional computational interior mesh point and Gauss' law volume.

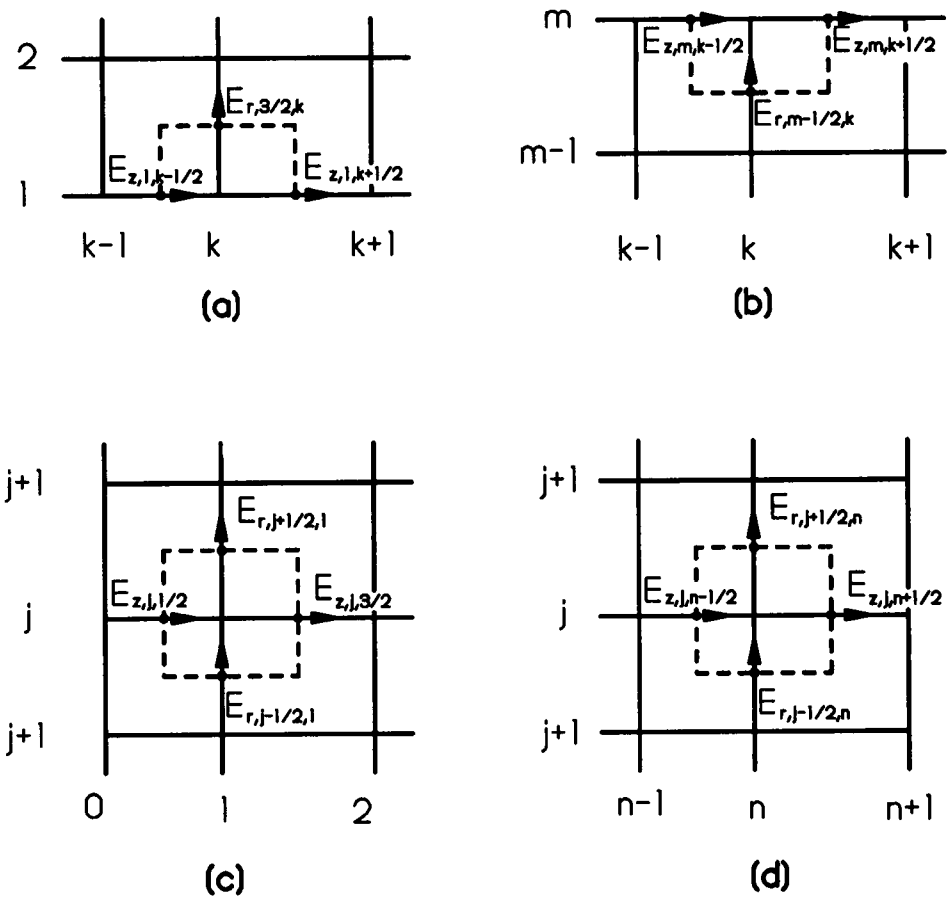

Figure 3.2. Two-dimensional computational boundary mesh points and Gauss' law volumes: (a) $r = 0$; (b) $r = r_{max}$; (c) $z = 0$; and (d) $z = z_{max}$.

To obtain the finite difference form of Poisson's equation at mesh point (j,k), Eq.(2.4) is integrated with a corresponding volume element, dv, centered on (j,k):

$$\iiint_{dv_{jk}} \nabla^2\phi dv = -\iiint_{dv_{jk}} \rho/\epsilon_0 dv. \tag{3.1}$$

By application of Gauss' law, Eq.(3.1) becomes

$$\iint_{dA_{jk}} \nabla\phi \cdot d\mathbf{A} = -\iiint_{dv_{jk}} \rho/\epsilon_0 dv, \tag{3.2}$$

or

$$\iint_{dA_{jk}} \mathbf{E} \cdot d\mathbf{A} = \iiint_{dv_{jk}} \rho/\epsilon_0 dv = Q_{j,k}, \tag{3.3}$$

where it is indicated that the right hand side of Eq.(3.3) is essentially the charge inside the computational cell (for simplicity, the dielectric constant ϵ_0 is absorbed in the definition of the charge). In the calculation, this charge $Q_{j,k}$ is calculated by interpolating the particle charges of the computational particles to the grid. That is,

$$Q_{j,k} = \sum_i S_i(j,k) q_i, \tag{3.4}$$

where q_i is the charge of particle i, and $S_i(j,k)$ is the weighting factor for interpolating the charge of particle i to the grid point (j,k) (see section **3.2**). In Eq.(3.4), the sum is, in principle, over all the computational particles in the calculation. In practice, it is only over those particles with a nonzero shape factor, namely particles that have coordinates between $j-1$ and $j+1$, and between $k-1$ and $k+1$.

The left hand side of Eq.(3.3) is the sum of the flux contributions to the control volume shown in Fig. 3.1 in the r and the z directions. These respective flux contributions may be written as:

$$Q_{r,j,k} = \mathbf{E}_{r,j-\frac{1}{2}} \cdot \hat{\mathbf{a}}_{r,j-\frac{1}{2}} dA_{r,j-\frac{1}{2}} + \mathbf{E}_{r,j+\frac{1}{2}} \cdot \hat{\mathbf{a}}_{r,j+\frac{1}{2}} dA_{r,j+\frac{1}{2}} \tag{3.5}$$

in the r-direction, and

$$Q_{z,j,k} = \mathbf{E}_{z,k-\frac{1}{2}} \cdot \hat{\mathbf{a}}_{z,k-\frac{1}{2}} dA_{z,k-\frac{1}{2}} + \mathbf{E}_{z,k+\frac{1}{2}} \cdot \hat{\mathbf{a}}_{z,k+\frac{1}{2}} dA_{z,k+\frac{1}{2}} \tag{3.6}$$

in the z-direction. The surface elements dA are given by

$$dA_{r,j-\frac{1}{2}} = 2\pi r_{j-\frac{1}{2}}(z_{k+\frac{1}{2}} - z_{k-\frac{1}{2}}), \tag{3.7}$$

$$dA_{r,j+\frac{1}{2}} = 2\pi r_{j+\frac{1}{2}}(z_{k+\frac{1}{2}} - z_{k-\frac{1}{2}}), \tag{3.8}$$

$$\begin{aligned} dA_{z,k-\frac{1}{2}} &= dA_{z,k+\frac{1}{2}} \\ &= \pi(r^2_{j+\frac{1}{2}} - r^2_{j-\frac{1}{2}}), \end{aligned} \tag{3.9}$$

where

$$r_{j+\frac{1}{2}} = \frac{r_{j+1} + r_j}{2}, \tag{3.10a}$$

$$r_{j-\frac{1}{2}} = \frac{r_{j-1} + r_j}{2}, \tag{3.10b}$$

$$z_{k+\frac{1}{2}} = \frac{z_{k+1} + z_k}{2}, \tag{3.10c}$$

and

$$z_{k-\frac{1}{2}} = \frac{z_{k-1} + z_k}{2}. \tag{3.10d}$$

To proceed with the discretization, interior and boundary mesh points are discussed separately.

3.1.1. Interior Mesh Points

Since the normal vectors satisfy the following conditions:

$$\hat{\mathbf{a}}_{r,j+\frac{1}{2}} = -\hat{\mathbf{a}}_{r,j-\frac{1}{2}} = \hat{\mathbf{j}}, \tag{3.11}$$

and

$$\hat{\mathbf{a}}_{z,k+\frac{1}{2}} = -\hat{\mathbf{a}}_{z,k-\frac{1}{2}} = \hat{\mathbf{k}}, \tag{3.12}$$

Eqs.(3.5) and (3.6) become, for $j > 0$,

$$Q_{r,j,k} = 2\pi(z_{k+\frac{1}{2}} - z_{k-\frac{1}{2}})(r_{j+\frac{1}{2}}E_{r,j+\frac{1}{2},k} - r_{j-\frac{1}{2}}E_{r,j-\frac{1}{2},k}), \tag{3.13a}$$

$$Q_{z,j,k} = \pi(r^2_{j+\frac{1}{2}} - r^2_{j-\frac{1}{2}})(E_{z,j,k+\frac{1}{2}} - E_{z,j,k-\frac{1}{2}}). \tag{3.13b}$$

Define

$$(\Delta r^2)_j = r^2_{j+\frac{1}{2}} - r^2_{j-\frac{1}{2}}, \tag{3.14a}$$

and

$$\Delta z_k = z_{k+\frac{1}{2}} - z_{k-\frac{1}{2}}. \tag{3.14b}$$

Then

$$\begin{aligned} Q_{j,k} &= Q_{r,j,k} + Q_{z,j,k} \\ &= 2\pi\Delta z_k(r_{j+\frac{1}{2}}E_{r,j+\frac{1}{2},k} - r_{j-\frac{1}{2}}E_{r,j-\frac{1}{2},k}) + \\ &\qquad \pi(\Delta r^2)_j(E_{z,j,k+\frac{1}{2}} - E_{z,j,k-\frac{1}{2}}). \end{aligned} \tag{3.15}$$

Single-cell differencing is used to express the electric fields in terms of the potentials:

$$E_{r,j+\frac{1}{2},k} = -\frac{\phi_{j+1,k} - \phi_{j,k}}{\Delta r_{j+\frac{1}{2}}}, \tag{3.16a}$$

$$E_{r,j-\frac{1}{2},k} = -\frac{\phi_{j,k} - \phi_{j-1,k}}{\Delta r_{j-\frac{1}{2}}}, \tag{3.16b}$$

$$E_{z,j,k+\frac{1}{2}} = -\frac{\phi_{j,k+1} - \phi_{j,k}}{\Delta z_{k+\frac{1}{2}}}, \tag{3.16c}$$

$$E_{z,j,k-\frac{1}{2}} = -\frac{\phi_{j,k} - \phi_{j,k-1}}{\Delta z_{k-\frac{1}{2}}}, \tag{3.16d}$$

where

$$\Delta z_{k+\frac{1}{2}} = z_{k+1} - z_k \tag{3.17a}$$

and

$$\Delta z_{k-\frac{1}{2}} = z_k - z_{k-1}. \tag{3.17b}$$

With this, the finite difference form of Poisson's equation in $\phi_{j,k}$ is obtained,

$$Q_{j,k} = -2\pi\Delta z_k(r_{j+\frac{1}{2}}\frac{\phi_{j+1,k}-\phi_{j,k}}{\Delta r_{j+\frac{1}{2}}} - r_{j-\frac{1}{2}}\frac{\phi_{j,k}-\phi_{j-1,k}}{\Delta r_{j-\frac{1}{2}}})-$$

$$\pi(\Delta r^2)_j(\frac{\phi_{j,k+1}-\phi_{j,k}}{\Delta z_{k+\frac{1}{2}}} - \frac{\phi_{j,k}-\phi_{j,k-1}}{\Delta z_{k-\frac{1}{2}}}) \tag{3.18}$$

or

$$-Q_{j,k} = a_{j+1,k}\phi_{j+1,k} + a_{j-1,k}\phi_{j-1,k} + a_{j,k+1}\phi_{j,k+1}$$

$$+ a_{j,k-1}\phi_{j,k-1} + a_{j,k}\phi_{j,k}. \tag{3.19}$$

where

$$a_{j+1,k} = 2\pi\Delta z_k r_{j+\frac{1}{2}}, \tag{3.20a}$$

$$a_{j-1,k} = 2\pi\Delta z_k r_{j-\frac{1}{2}}, \tag{3.20b}$$

$$a_{j,k+1} = \pi\frac{(\Delta r^2)_j}{\Delta z_{k+\frac{1}{2}}}, \tag{3.20c}$$

$$a_{j,k-1} = \pi\frac{(\Delta r^2)_j}{\Delta z_{k-\frac{1}{2}}}, \tag{3.20d}$$

and

$$a_{j,k} = -(a_{j+1,k} + a_{j-1,k} + a_{j,k+1} + a_{j,k-1}). \tag{3.20e}$$

3.1.2. Boundary Mesh Points

Case a.) $r = 0$ $(j = 1)$.

For the volume shown by the dashed lines centered on $(j = 1, k)$ in Fig. 3.2a, Eq.(3.15) becomes:

$$Q_{1,k} = 2\pi\Delta z_k r_{\frac{3}{2}} E_{r,\frac{3}{2},k} + \pi(\Delta r^2)_1(E_{z,1,k+\frac{1}{2}} - E_{z,1,k-\frac{1}{2}}), \tag{3.21}$$

where

$$(\Delta r^2)_1 = r_{\frac{3}{2}}^2 - r_1^2 = r_{\frac{3}{2}}^2. \tag{3.22}$$

(Note that $E_{r,1,k} = 0$ in the absence of a line charge at $r = 0$). Hence, the finite difference form of Poisson's equation for the origin is:

$$Q_{1,k} = -2\pi\Delta z_k r_{\frac{3}{2}} \frac{\phi_{2,k} - \phi_{1,k}}{\Delta r_{\frac{3}{2}}} - \pi(\Delta r^2)_1 \left(\frac{\phi_{1,k+1} - \phi_{1,k}}{\Delta z_{k+\frac{1}{2}}} - \frac{\phi_{1,k} - \phi_{1,k-1}}{\Delta z_{k-\frac{1}{2}}}\right), \tag{3.23}$$

or

$$-Q_{1,k} = a_{2,k}\phi_{2,k} + a_{1,k+1}\phi_{1,k+1} + a_{1,k-1}\phi_{1,k-1} + a_{1,k}\phi_{1,k}, \tag{3.24}$$

where

$$a_{2,k} = 2\pi\Delta z_k r_{\frac{3}{2}}, \tag{3.25a}$$

$$a_{1,k+1} = \pi\frac{(\Delta r^2)_1}{\Delta z_{k+\frac{1}{2}}}, \tag{3.25b}$$

$$a_{1,k-1} = \pi\frac{(\Delta r^2)_1}{\Delta z_{k-\frac{1}{2}}}, \tag{3.25c}$$

and

$$a_{1,k} = -(a_{2,k} + a_{1,k+1} + a_{1,k-1}). \tag{3.25d}$$

Case b.) $r = r_{max}$ $(j = m)$.

It is assumed that the boundary condition at $r = r_{max}$ is

$$\frac{\partial\phi}{\partial r} = 0. \tag{3.26}$$

Thus, the differencing equations for the boundary mesh points at $r = r_{max}$ are similar to the ones at $r = 0$ (see Fig. 3.2b):

$$-Q_{m,k} = a_{m-1,k}\phi_{m-1,k} + a_{m,k+1}\phi_{m,k+1} + a_{m,k-1}\phi_{m,k-1} + a_{m,k}\phi_{m,k}, \tag{3.27}$$

where

$$a_{m-1,k} = 2\pi r_{m-\frac{1}{2}} \Delta z_k, \tag{3.28a}$$

$$a_{m,k+1} = \pi \frac{(\Delta^2)_m}{\Delta z_{k+\frac{1}{2}}}, \tag{3.28b}$$

$$a_{m,k-1} = \pi \frac{(\Delta^2)_m}{\Delta z_{k-\frac{1}{2}}}, \tag{3.28c}$$

$$a_{m,k+1} = -(a_{m-1,k} + a_{m,k+1} + a_{m,k-1}), \tag{3.28d}$$

and

$$(\Delta r^2)_m = r_m^2 - r_{m-\frac{1}{2}}^2. \tag{3.29}$$

Case c.) $z = 0$ $(k = 1)$.

It is assumed that there is a neutral plasma existing at the upstream boundary from the screen grid with the plasma potential of ϕ_0. Thus, the finite-difference equations for the mesh points at the upstream boundary are:

$$Q_{j,1} = -2\pi \Delta z_1 (r_{j+\frac{1}{2}} \frac{\phi_{j+1,1} - \phi_{j,1}}{\Delta r_{j+\frac{1}{2}}} - r_{j-\frac{1}{2}} \frac{\phi_{j,1} - \phi_{j-1,1}}{\Delta r_{j-\frac{1}{2}}}) -$$

$$\pi (\Delta r^2)_j (\frac{\phi_{j,2} - \phi_{j,1}}{\Delta z_{\frac{3}{2}}} - \frac{\phi_{j,1} - \phi_{j,0}}{\Delta z_{\frac{1}{2}}}) \tag{3.30}$$

or

$$-Q_{j,1} - \frac{\pi (\Delta r^2)_j}{\Delta z_{\frac{1}{2}}} \phi_0 = a_{j+1,1}\phi_{j+1,1} + a_{j-1,1}\phi_{j-1,1} + a_{j,2}\phi_{j,2} + a_{j,1}\phi_{j,1}, \tag{3.31}$$

where

$$a_{j+1,1} = 2\pi \Delta z_1 r_{j+\frac{1}{2}}, \tag{3.32a}$$

$$a_{j-1,1} = 2\pi \Delta z_1 r_{j-\frac{1}{2}}, \tag{3.32b}$$

$$a_{j,2} = \pi \frac{(\Delta r^2)_j}{\Delta z_{\frac{3}{2}}}, \tag{3.32c}$$

$$a_{j,1} = -(a_{j+1,1} + a_{j-1,1} + a_{j,2}), \tag{3.32d}$$

$$\Delta z_{\frac{1}{2}} = z_1 - z_0, \tag{3.33}$$

and

$$\Delta z_1 = \frac{z_2 - z_0}{2}. \tag{3.34}$$

Case d.) $z = z_{max}$ $(k = n)$.

Several choices can be made for the downstream boundary condition. A fixed potential can be assumed at the downstream end of the computational domain if the potential is known. It may also be assumed that the electric field approaches zero at the boundary. This corresponds to setting the potential derivative equal to zero. It may also be assumed that the plasma approaches charge neutrality at the boundary. This corresponds to setting the second derivative of the potential equal to zero. Each of these assumptions has been used in the calculations discussed in section **3.3**. Different downstream boundary conditions result in different finite-difference equations at the boundary mesh points. The finite-difference equations for these three types of boundary condition are given in the following.

$\phi = \phi_e = 0.$

This boundary condition is of the same type of for the upstream boundary. Therefore, a similar type of finite-difference equation results:

$$-Q_{j,n} - \frac{\pi(\Delta r^2)_j}{\Delta z_{n+\frac{1}{2}}}\phi_e = a_{j+1,n}\phi_{j+1,n} + a_{j-1,n}\phi_{j-1,n} + a_{j,n-1}\phi_{j,n-1} + a_{j,n}\phi_{j,n}. \tag{3.35}$$

where

$$a_{j+1,n} = 2\pi r_{j+\frac{1}{2}} \Delta z_n, \tag{3.36a}$$

$$a_{j-1,n} = 2\pi r_{j-\frac{1}{2}} \Delta z_n, \tag{3.36b}$$

$$a_{j,n-1} = \pi \frac{(\Delta r^2)_j}{\Delta z_{n-\frac{1}{2}}}, \tag{3.36c}$$

$$a_{j,n} = -(a_{j+1,n} + a_{j-1,n} + a_{j,n-1}), \tag{3.36d}$$

$$\Delta z_{n+\frac{1}{2}} = z_e - z_n, \tag{3.37}$$

and

$$\Delta z_n = \frac{z_e - z_{n-1}}{2}. \tag{3.38}$$

$\underline{\partial\phi/\partial z = 0}$.

This type of boundary condition is the same as the one discussed in Cases a.) and b.) in the radial direction. Therefore the finite-difference equation can be written as

$$-Q_{j,n} = a_{j+1,n}\phi_{j+1,n} + a_{j-1,n}\phi_{j-1,n} + a_{j,n-1}\phi_{j,n-1} + a_{j,n}\phi_{j,n}. \tag{3.39}$$

where

$$a_{j+1,n} = 2\pi r_{j+\frac{1}{2}} \Delta z_n, \tag{3.40a}$$

$$a_{j-1,n} = 2\pi r_{j-\frac{1}{2}} \Delta z_n, \tag{3.40b}$$

$$a_{j,n-1} = \pi \frac{(\Delta r^2)_j}{\Delta z_{n+\frac{1}{2}}}, \tag{3.40c}$$

and

$$a_{j,n} = -(a_{j+1,n} + a_{j-1,n} + a_{j,n-1}). \tag{3.40d}$$

$\underline{\partial^2\phi/\partial z^2 = 0}$.

This type of boundary condition has been used in CFD simulation for dealing with open boundary condition (Eraslan 1974). By assuming $\left(\frac{\partial^2\phi}{\partial z^2}\right) = 0$, the

potential ϕ_e, as shown in Fig. 3.2d, can be written as

$$\phi_e^* = \phi_n^* \left(\frac{1}{\Delta z_{n+\frac{1}{2}}} + \frac{1}{\Delta z_{n-\frac{1}{2}}} \right) - \phi_{n-1}^* \frac{1}{\Delta z_{n-\frac{1}{2}}} \tag{3.41}$$

where an asterisk represents a previous timestep. Thus, the ϕ_e is updated every timestep using previous values of ϕ_n and ϕ_{n-1}, and the finite-difference equations for this type of downstream boundary condition are

$$-Q_{j,n} - \frac{\pi(\Delta r^2)_j}{\Delta z_{n+\frac{1}{2}}} \phi_e^* = a_{j+1,n}\phi_{j+1,n} + a_{j-1,n}\phi_{j-1,n} + a_{j,n-1}\phi_{j,n-1} + a_{j,n}\phi_{j,n}. \tag{3.42}$$

where

$$a_{j+1,n} = 2\pi r_{j+\frac{1}{2}} \Delta z_n, \tag{3.43a}$$

$$a_{j-1,n} = 2\pi r_{j-\frac{1}{2}} \Delta z_n, \tag{3.43b}$$

$$a_{j,n-1} = \pi \frac{(\Delta r^2)_j}{\Delta z_{n-\frac{1}{2}}}, \tag{3.43c}$$

and

$$a_{j,n} = -(a_{j+1,n} + a_{j-1,n} + a_{j,n-1}). \tag{3.43d}$$

Case e.) Screen and accelerator grids.

Finally, boundary conditions are specified at the screen and accelerator grids, which have fixed potentials ϕ_s and ϕ_a. Grid points of the computational mesh are chosen such that the boundaries of the physical grids coincide with the computational grid. Therefore, the finite-difference equations are similar to the ones in Cases c.) and d.).

3.1.3. The Final Discretization Equations

In summary, the finite difference equations for all interior and boundary mesh points can be written in matrix form as:

$$\underline{\underline{\mathbf{A}}} \cdot \underline{\psi} = \underline{\mathbf{b}}. \tag{3.44}$$

Here the raised dot denotes matrix multiplication, $\underline{\underline{\mathbf{A}}}$ is the matrix of coefficients, $\underline{\psi}$ is an unknown column vector, and $\underline{\mathbf{b}}$ is a known right-hand side column vector. Schematically, the quantities in Eq.(3.44) can be written as

$$\underline{\underline{\mathbf{A}}} = \begin{pmatrix} A_{1,1} & A_{1,2} & & & & & \\ A_{2,1} & A_{2,2} & A_{2,3} & & & & \\ & A_{3,2} & A_{3,3} & A_{3,4} & & & \\ & & \ddots & \ddots & \ddots & & \\ & & & A_{n-1,n-2} & A_{n-1,n-1} & A_{n-1,n} & \\ & & & & A_{n,n-1} & A_{n,n} \end{pmatrix}, \tag{3.45a}$$

$$\underline{\psi} = \begin{pmatrix} \psi_1 \\ \psi_2 \\ \vdots \\ \psi_k \\ \vdots \\ \psi_n \end{pmatrix}, \tag{3.45b}$$

and

$$\underline{\mathbf{b}} = \begin{pmatrix} s_1 \\ s_2 \\ \vdots \\ s_k \\ \vdots \\ s_n \end{pmatrix}, \tag{3.45c}$$

where n is the maximum value of k. The matrix on the left-hand side of Eq.(3.45a) is a block tridiagonal matrix as shown. These blocks are also sparse, with diagonal blocks containing not more than five nonzero elements in every row, and the off-diagonal blocks only having at most one nonzero element in any row. Each element

ψ_k represents a column vector with components $\phi_{j,k}$ for $j = 1, m$. The elements of the right-hand side of Eq.(3.45c) are vectors with elements

$$s_{j,k} = -Q_{j,k} = -q_{j,k}/\epsilon_0 \tag{3.46}$$

for interior mesh points. For boundary mesh points, an additional term appears, as expressed in Eqs.(3.31), (3.35), and (3.42). For example, for $k = 1$:

$$s_{j,k} = -Q_{j,k} - \phi_0 \frac{\pi(\Delta r^2)_j}{\Delta z_{\frac{1}{2}}}. \tag{3.47}$$

Similarly, additional terms appear near the screen grid, the accelerator grid, and the downstream plasma boundary.

The solution of Eq.(3.44) is obtained by using standard subroutines from the IMSL library which use the *LU* decomposition method. The principle of this method is that the coefficient matrix is rewritten as a product of two matrices,

$$\underline{\underline{\mathbf{L}}} \cdot \underline{\underline{\mathbf{U}}} = \underline{\underline{\mathbf{A}}}, \tag{3.48}$$

where $\underline{\underline{\mathbf{L}}}$ is a *lower triangular* matrix (has elements only on the diagonal and below) and $\underline{\underline{\mathbf{U}}}$ is an *upper triangular* matrix (has elements only on the diagonal and above). Then, Eq.(3.44) becomes

$$\underline{\underline{\mathbf{A}}} \cdot \underline{\psi} = (\underline{\underline{\mathbf{L}}} \cdot \underline{\underline{\mathbf{U}}}) \cdot \underline{\psi} = \underline{\underline{\mathbf{L}}} \cdot (\underline{\underline{\mathbf{U}}} \cdot \underline{\psi}) = \underline{\mathbf{b}}. \tag{3.49}$$

Thus, the solution of Eq.(3.44) is obtained by first solving

$$\underline{\underline{\mathbf{L}}} \cdot \underline{\chi} = \underline{\mathbf{b}} \tag{3.50}$$

for the vector $\underline{\chi}$ and then solving

$$\underline{\underline{\mathbf{U}}} \cdot \underline{\psi} = \underline{\chi} \tag{3.51}$$

for the vector $\underline{\psi}$. The LU decomposition only has to be performed once, because the computational geometry remains unchanged.

3.2. Weighting Factor in Cylindrical Coordinates

Two important steps of the PIC method are to assign the particle charges to their nearest neighbor mesh points and to calculate the forces on the particles from the mesh-defined electric fields. These calculations are called weighting. It is desirable to use the same weighting for both charge density and force calculations in order to avoid a *self-force*, i.e., a particle accelerating itself (Birdsall and Langdon 1985 and Hockney and Eastwood 1989). Different methods for particle-weighting have been used in the literature. One of the most widely-used methods is that of area-weighting (or volume-weighting in three dimensions). However, as shown by Ruyten (1991), this method does not conserve charge-density when applied in cylindrical coordinates. Therefore, an alternative, charge-density-conserving weighting factor is used (Ruyten 1991):

$$S_{r,j}(r_p) = \begin{cases} S^{-}_{r,j}(r_p), & r_{j-1} \le r_p < r_j, \\ S^{+}_{r,j}(r_p), & r_j \le r_p < r_{j+1}, \\ 0, & \text{otherwise}, \end{cases} \tag{3.52}$$

$$= \begin{cases} 1 - \dfrac{3}{2}\left(\dfrac{r_j - r_p}{r_j - r_{j-1}}\right) + \dfrac{1}{2}\left(\dfrac{r_j^2 - r_p^2}{r_j^2 - r_{j+1}^2}\right), & r_{j-1} \le r_p < r_j, \\ \dfrac{3}{2}\left(\dfrac{r_{j+1} - r_p}{r_{j+1} - r_j}\right) - \dfrac{1}{2}\left(\dfrac{r_{j+1}^2 - r_p^2}{r_{j+1}^2 - r_j^2}\right), & r_j \le r_p < r_{j+1}, \\ 0, & \text{otherwise}, \end{cases} \tag{3.53}$$

in the radial direction. An example of this weighting factor is shown in Fig. 3.3.

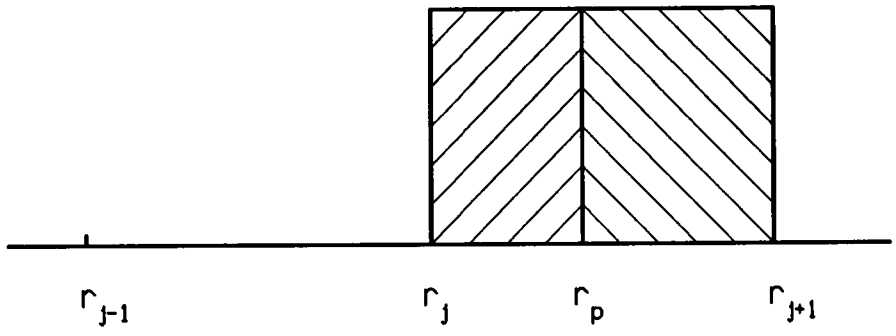

Figure 3.3. Illustration of particle-in-cell weighting for a particle at r_p, located between mesh points r_j and r_{j+1}.

In the z-direction, linear weighting is used, given by

$$S_{z,k}(r_p) = \begin{cases} S^-_{z,k}(z_p), & z_{k-1} \le z_p < z_k, \\ S^+_{z,k}(z_p), & z_k \le z_p < z_{k+1}, \\ 0, & otherwise, \end{cases} \tag{3.54}$$

$$= \begin{cases} 1 - \left(\dfrac{z_k - z_p}{z_k - z_{k-1}}\right), & z_{k-1} \le z_p < z_k, \\ \left(\dfrac{z_{k+1} - z_p}{z_{k+1} - z_k}\right), & z_k \le z_p < z_{k+1}, \\ 0, & \text{otherwise.} \end{cases} \tag{3.55}$$

This weighting is shown in Fig. 3.4. Combining the shape factors in the r and the z directions, the shape factor for mesh point (j,k) takes the product form:

$$S_{j,k}(r_p, z_p) = S_{r,j}(r_p) S_{z,k}(z_p). \tag{3.56}$$

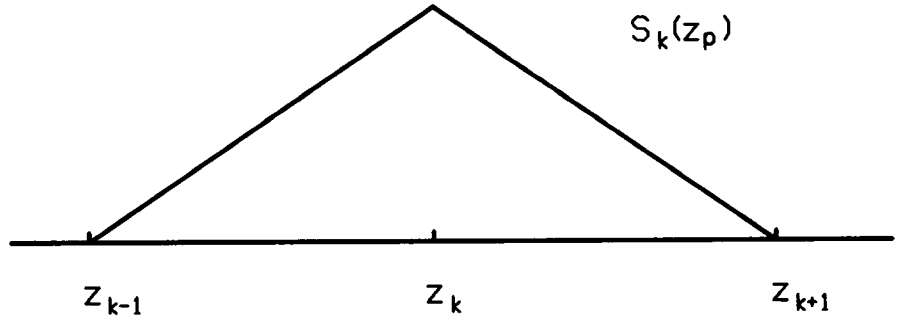

Figure 3.4. PIC linear weighting scheme.

With Eqs.(3.53) and (3.54), this weighting factor becomes

$$\begin{aligned}
q_{j,k} &= q_p \frac{(r_{j+1} - r_p)(z_{k+1} - z_p)}{2(r_{j+1}^2 - r_j^2)(z_{k+1} - z_k)}(2r_{j+1} + 3r_j - r_p), \\
q_{j+1,k} &= q_p \frac{(r_p - r_j)(z_{k+1} - z_p)}{2(r_{j+1}^2 - r_j^2)(z_{k+1} - z_k)}(3r_{j+1} + 2r_j - r_p), \\
q_{j+1,k+1} &= q_p \frac{(r_p - r_j)(z_p - z_k)}{2(r_{j+1}^2 - r_j^2)(z_{k+1} - z_k)}(3r_{j+1} + 2r_j - r_p), \\
q_{j,k+1} &= q_p \frac{(r_{j+1} - r_p)(z_p - z_k)}{2(r_{j+1}^2 - r_j^2)(z_{k+1} - z_k)}(2r_{j+1} + 3r_j - r_p),
\end{aligned} \tag{3.57}$$

where q_p is the particle charge. During each iteration, all particle charges are distributed onto their neighboring mesh points according to Eq.(3.57) to obtain the grid charge from Eq.(3.4). In order to obtain charge-density, these charges are divided by their discretization volumes, shown in Figs. 3.1 and 3.2.

In the next section, example calculations are conducted to demonstrate the capability of this two-dimensional particle simulation model.

3.3. Example Calculations

The examples given in this section include the comparisons between simulations without and with consideration of charge exchange collisions and the parametric studies of the downstream electric potential field.

3.3.1. Geometry and Plasma Conditions

The geometry and plasma conditions were chosen to correspond to the experimental configuration used by Patterson and Verhey (1990) to study sputtering erosion of the accelerator grid in a xenon ion thruster. The screen and accelerator grid radii are 0.95 and 0.55 mm, respectively. The outside radius of the computational domain is 1.11 mm, yielding the desired screen open fraction of 0.67. The thickness of both grids is 0.38 mm, and the distance between two grids is 0.76 mm. The screen grid is at a potential of $1517V$ and the accelerator grid is at a potential of $-331V$. The average discharge voltage is about $27V$, therefore the upstream neutral plasma potential is assumed to be at $+1544V$. Plasma boundary is at about 1 mm upstream from the screen grid.

Ion, electron, and neutral parameters are as follows. It is assumed that a neutral plasma exists at the upstream boundary of the computational domain. The ion density and the mean ion extraction velocity are chosen together to have the desired beam current. In this study, the ion number density and the mean ion extraction velocity are set to be $1.34 \times 10^{18} m^{-3}$ and $400 m/s$, respectively. The electron temperature in this typical plasma is about 1.5 eV and the ion temperature is assumed $1000K$. Downstream plasma conditions are taken to be equal to those of the upstream plasma, except for the ion density. The neutral gas density is assumed uniform throughout the computational domain at a density

of $5 \times 10^{18} m^{-3}$ which corresponds to a neutral background pressure of about $5.2 \times 10^{-4} torr$. Therefore, this assumed neutral number density represents a residual facility background, rather than efflux from the thruster. The geometry of the ion optics system and physical parameters are summarized in Table 3.1.

Table 3.1. Input Parameters for 2D Calculations

Screen hole diameter	(mm)	1.9
Accelerator hole diameter	(mm)	1.1
Thickness of both grids	(mm)	0.38
Grid-to-grid distance	(mm)	0.76
Screen grid open fraction		0.67
Plasma potential	(V)	1544
Screen grid potential	(V)	1517
Accelerator grid potential	(V)	-331
Electron temperature	(eV)	1.5
Ion temperature	(K)	1000
Ion extraction velocity	(m/s)	400
Upstream ion density	(m^{-3})	1.3×10^{18}
Neutral gas density	(m^{-3})	5×10^{18}

3.3.2. Comparisons with and without Charge Exchange Collisions

The calculation was performed on a mesh containing 47 cells in the axial, and 12 cells in the radial directions, using a timestep of 1.8×10^{-9} seconds. At about 9 μsecs (5000 timesteps), the calculation was terminated, at which time the computational domain contained about 50,000 simulation particles. The total *CPU* time was about 3 hours (with IBM RISC SYSTEM/6000/550 computer). Calculations were performed both without and with charge exchange collisions,

results of which are shown in Figs. 3.5, 3.6, and 3.7. Independently, it was confirmed that varying the number of grid points and the time step does not lead to substantially different results.

Fig. 3.5 shows a comparison of the calculated electric potential contours. These contours are determined primarily by the potentials on the grids. However, especially in the downstream region, curvature of these potential contours is due also to the space charge from the extracted ion beam. Because of the presence of the ions, the electric potential inside the ion beam region is more positive than outside the ion beam. Therefore, this potential field tends to force the charge-exchange ions to terminate at the middle portion of the downstream surface of the accelerator grid where the maximum accelerator grid erosion is observed from experiment. Little difference exists in upstream region of accelerator grid between the contours in Figs. 3.5(a) and 3.5(b). However, in the downstream region of accelerator grid, the zero volt plane is closer to the accelerator grid in Fig. 3.5(b) (charge exchange case) than in Fig. 3.5(a). This indicates that the charge exchange ions have an influence on the electric field in the downstream region where the potential gradient is not so great as in the grid region. In both Figs. 3.5(a) and 3.5(b), contour line A shows that there exists a potential hill in the downstream region. For the charge exchange case, this potential hill can prevent those charge exchange ions which are created in the region beyond the hill from striking the accelerator grid.

Fig. 3.6 shows ion number densities for the same calculation (actually, the contours in Fig. 3.6 correspond to the logarithm of the ion density). Both Figs. 3.6(a) and 3.6(b) show the largest ion density on the axis, due to electrostatic focusing of the beam ions. Some differences between the cases without (a) and with (b) consideration of charge exchange collisions can be found in the region

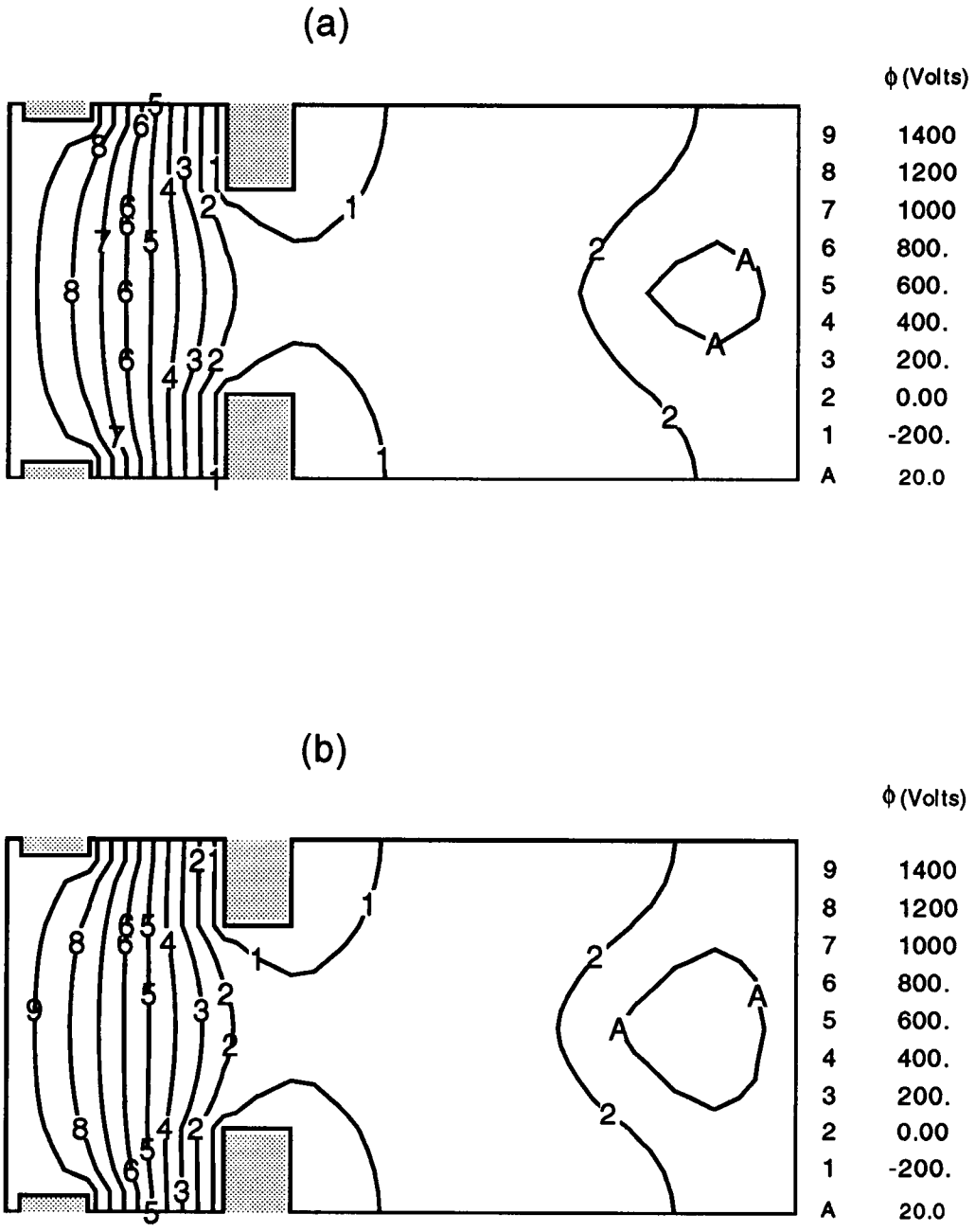

Figure 3.5. Computed electric potential contours without (a) and with (b) charge exchange collisions.

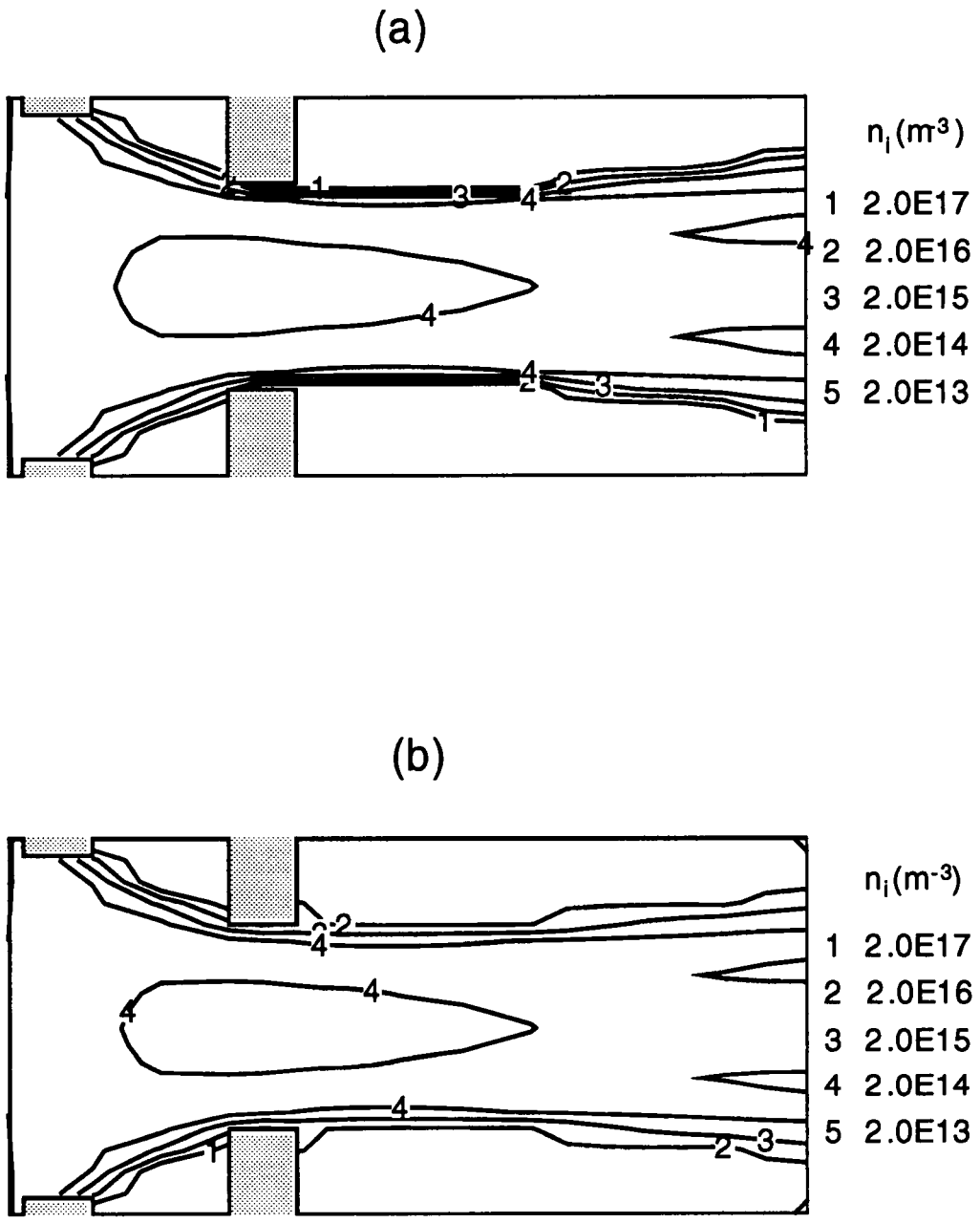

Figure 3.6. Computed ion number density contours without (a) and with (b) charge exchange collisions.

outside the primary ion beam, which shows a higher ion density when charge exchange ions are accounted.

Fig. 3.7 shows average ion velocities without (a) and with (b) consideration of charge exchange collisions. In the absence of charge exchange collisions, all ions are focused through the accelerator grid except those that impinge directly on the upstream surface of the accelerator grid, but the charge-exchange ions — represented mostly by the small arrows outside of the primary ion beam — are focused primarily onto the downstream surface of the accelerator grid.

3.3.3. Comparisons with Different Downstream Conditions

The shape and location of the downstream plasma boundary is important to explain the accelerator grid charge exchange erosion patterns observed in the experiments. Therefore, by choosing different downstream boundary conditions and varying the distance between the accelerator grid and the assumed boundary position, the sensitivity of the downstream electric potential field and the shape and location of the plasma boundary can be assessed

Figs. 3.8 and 3.9 show electric potential contours with different downstream boundary conditions. The assumed boundary positions in Fig. 3.8 and Fig. 3.9 are located at 3 *mm* and 5 *mm* downstream from the accelerator grid, respectively. Comparing Figs. 3.8 and 3.9, it can be seen that if the assumed boundary is too close to the accelerator grid, the shape of the plasma boundary is sensitive to the boundary condition chosen. However, the shape and location of the plasma boundary and the peak value of the potential hill beyond the plasma boundary are not sensitive to the different boundary conditions if the assumed boundary position is far enough from the accelerator grid, as shown in Fig. 3.9.

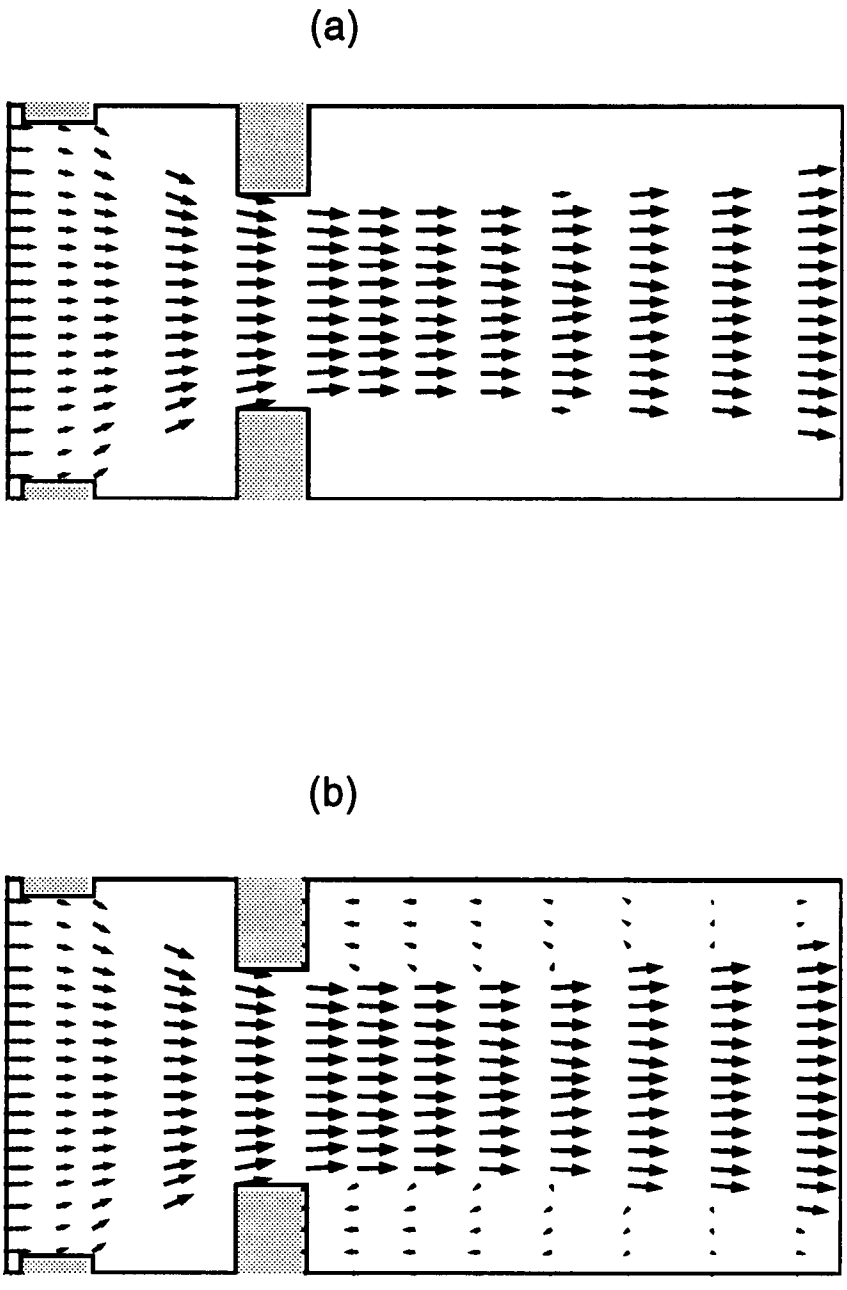

Figure 3.7. Computed average ion velocities without (a) and with (b) charge exchange collisions. The magnitude of the largest vectors is 50,000 m/sec.

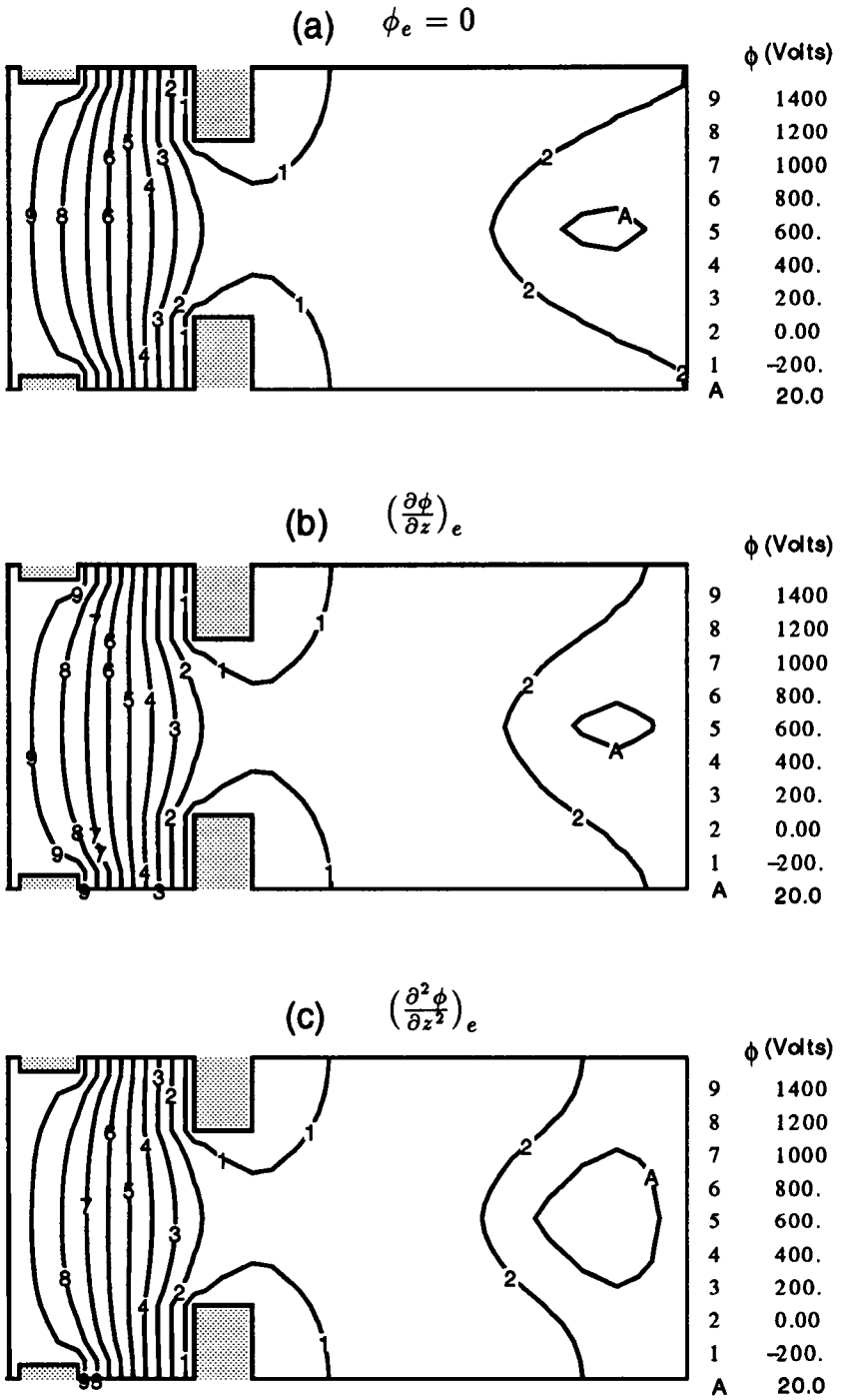

Figure 3.8. Computed electric potential contours for different downstream boundary conditions: (a) $\phi_e = 0$, (b) $(\frac{\partial \phi}{\partial z})_e = 0$, and (c) $(\frac{\partial^2 \phi}{\partial z^2})_e = 0$. The distance between the accelerator grid and assumed boundary position is 3 *mm*.

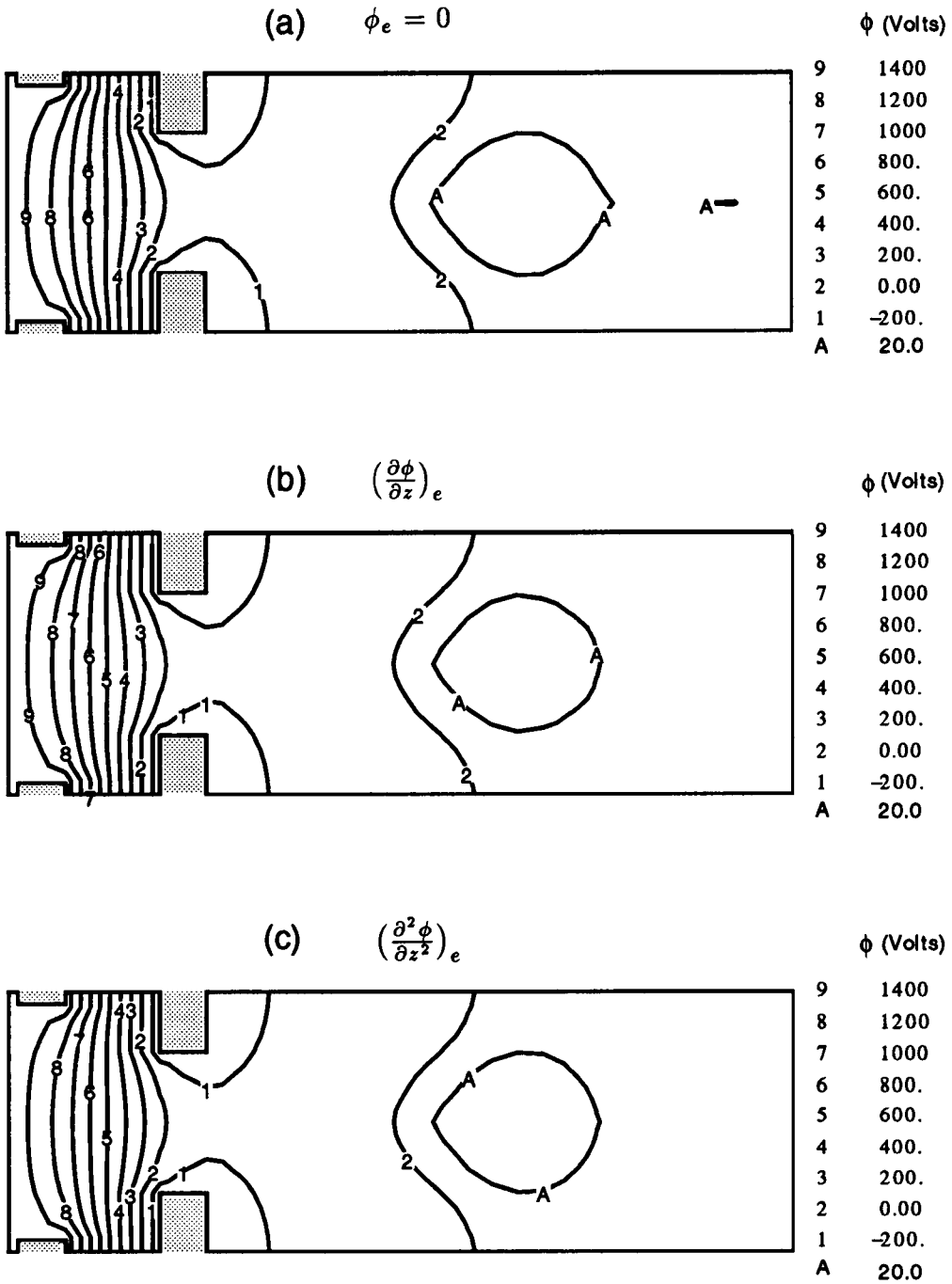

Figure 3.9. Computed electric potential contours for different downstream boundary conditions: (a) $\phi_e = 0$, (b) $(\frac{\partial \phi}{\partial z})_e = 0$, and (c) $(\frac{\partial^2 \phi}{\partial z^2})_e = 0$. The distance between the accelerator grid and assumed boundary position is 5 *mm*.

Only those charge exchange ions which are created in the region between the accelerator grid and the upstream side of the potential hill will strike the accelerator grid and cause sputtering erosion of the accelerator grid. Therefore, it is expected that the erosion rates will not show significant differences for those three cases in Fig. 3.9, (see in Fig. 3.11).

Actually, the assumption that the second derivative of potential is equal to zero means that there is a pseudo-neutral plasma in the downstream region with a possible non-zero electric field. Therefore, Fig. 3.9 indicates that the electric field is approaching zero and the electric potential tends to the downstream plasma potential vary rapidly beyond the potential hill in the downstream plasma region. However, this result is based on the assumption that the electron density is given by Boltzmann distribution,

$$n_e = n_d \exp(-(\phi - \phi_d)/kT_e), \tag{3.58}$$

where n_d and ϕ_d are the downstream plasma number density and electric potential, and n_e and ϕ are the local number density and potential. T_e is the electron temperature and k is the Boltzmann constant. The detailed understanding of the downstream potential fields including the plasma region and inside the plasma will require inclusion of the electron particles in the simulation procedure.

Figs. 3.10 and 3.11 show the erosion rates with the different downstream boundary conditions. Fig. 3.10 and 3.11 correspond to the boundary conditions shown in Fig. 3.8 and 3.9, respectively. In both figures, again, the boundary conditions are: (a) zero electric potential, $\phi = 0$; (b) zero electric field, $\partial\phi/\partial z = 0$; and (c) zero second derivative of electric potential, $\partial^2\phi/\partial z^2 = 0$.

In Fig. 3.10, case (a) is different from the other two cases since the shape of the plasma boundary for case (a) is different than cases (a) and (b), as shown in

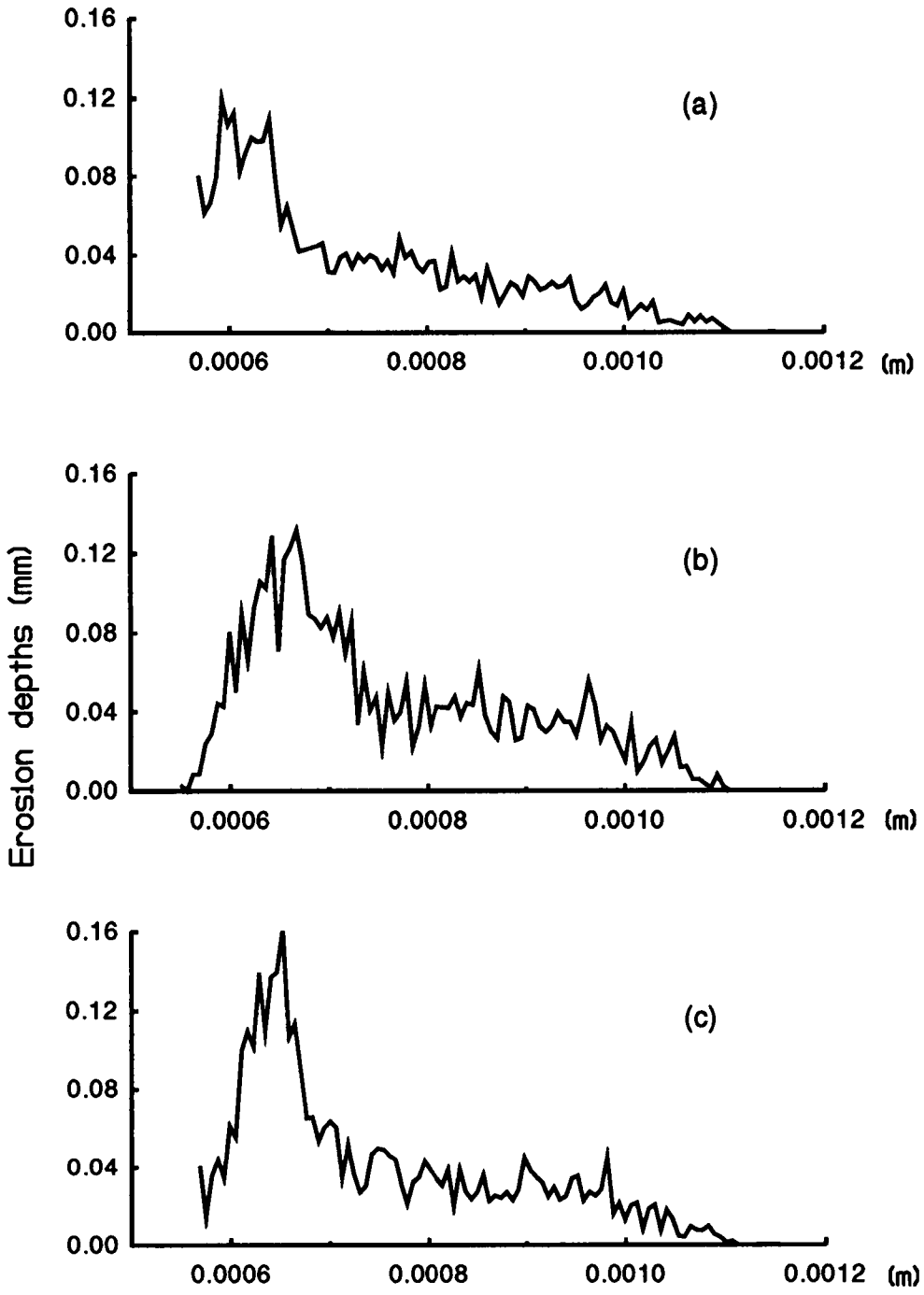

Figure 3.10. Comparison of computed erosion depths per 1000 hrs of operation of the downstream accelerator grid surface as a function of radius for different downstream boundary conditions: (a) $\phi_e = 0$, (b) $(\frac{\partial \phi}{\partial z})_e = 0$, and (c) $(\frac{\partial^2 \phi}{\partial z^2})_e = 0$. The distance between the accelerator grid and the assumed boundary position equals 3 *mm*.

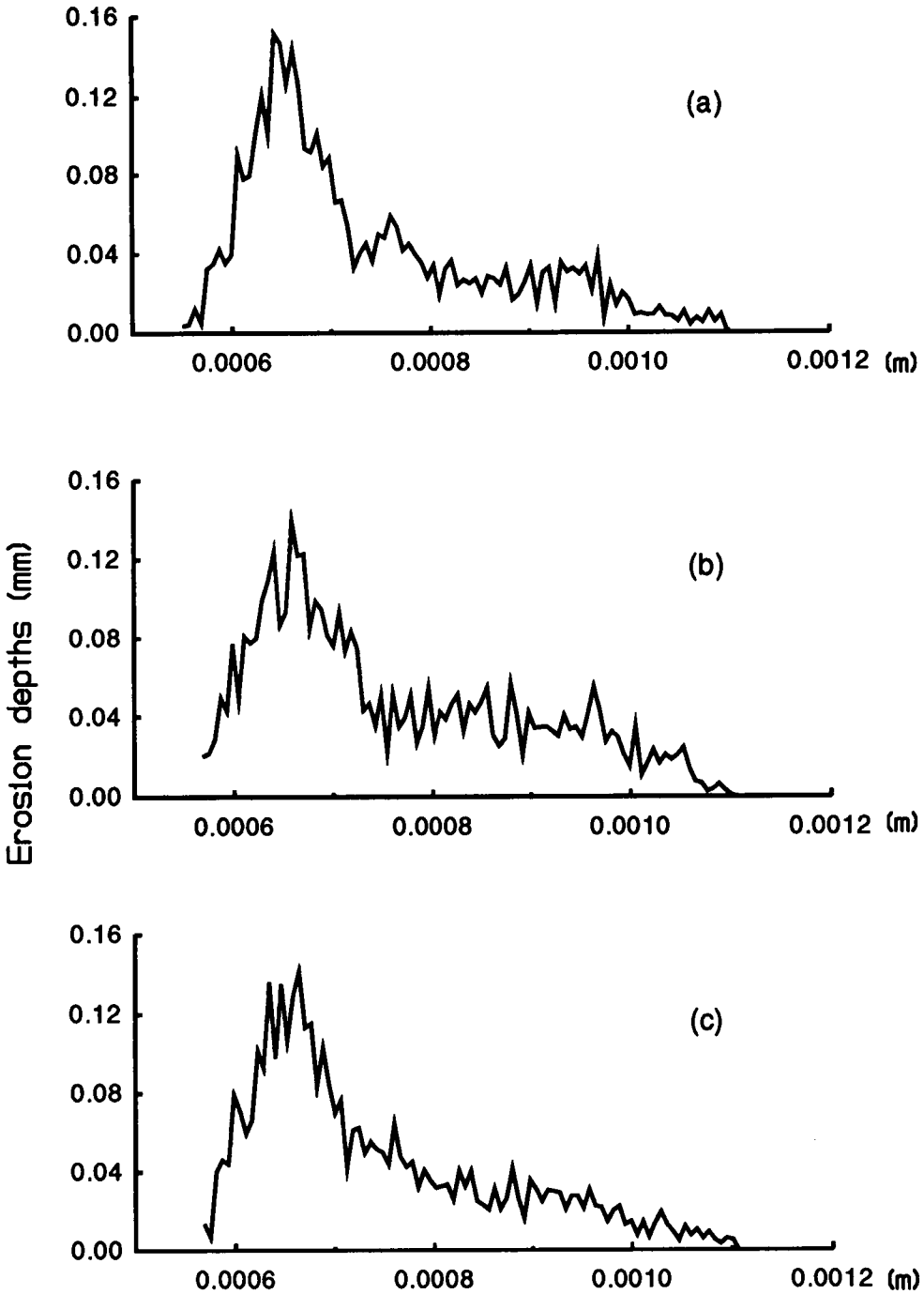

Figure 3.11. Comparison of computed erosion depths per 1000 hrs of operation of the downstream accelerator grid surface as a function of radius for different downstream boundary conditions: (a) $\phi_e = 0$, (b) $(\frac{\partial \phi}{\partial z})_e = 0$, and (c) $(\frac{\partial^2 \phi}{\partial z^2})_e = 0$. The distance between the accelerator grid and the assumed boundary position equals 5 *mm*.

Fig. 3.8. As mentioned above, the erosion patterns of the three cases shown in Fig. 3.11 are expected to be similar because there is not much difference between their electric potential fields.

Fig. 3.12 shows the electric potential contours for different downstream distances between the accelerator grid and the assumed boundary position. Three cases are shown in the figure with distances of: (a) 3 *mm*; (b) *4mm*; and (c) *5mm*. The boundary condition for all three cases is a zero electric potential. Fig. 3.13 shows similar comparisons but with a different downstream boundary condition: the second derivative of electric potential equals to zero. For the assumed potential equal to zero, it can be seen, from Fig. 3.12, that the shape of the plasma boundary and the electric potential contours varies when the distance between the accelerator grid and the assumed boundary position changes. Such differences shown in the potential fields will result in different erosion patterns. Fig. 3.14 shows erosion rates corresponding to the cases shown in Fig. 3.12. However, the shape of the plasma boundary and the contours of the potential hill are not very sensitive when the distance between accelerator grid and the assumed boundary position is changed in Fig. 3.13. Therefore, for the same reason as discussed for Fig. 3.11, the erosion patterns corresponding to the three cases in Fig. 3.13 should not show significant differences. This is given in Fig. 3.15.

The influence of the downstream plasma density on the downstream electric field is shown in Figs. 3.16 and 3.17 with three assumed plasma densities: (a) $10^{13}m^{-3}$, (b) $10^{14}m^{-3}$, and (c) $10^{15}m^{-3}$. Three cases in Fig. 3.16 are calculated with downstream boundary condition $\phi = 0$ while in Fig. 3.17 the downstream boundary condition is $\partial^2\phi/\partial z^2 = 0$. From these two figures, it can be seen that the shape and location of the plasma boundary is not sensitive to the magnitude of the plasma density, but the peak value of the potential hill increases when the plasma

density decreases. Figs. 3.18 and 3.19 are calculated erosion rates corresponding to Figs. 3.16 and 3.17, respectively. The erosion patterns and the peak values are not very sensitive to the magnitude of the downstream plasma density. It should be pointed out here, again, that this conclusion is based on a simulation which does not include a direct simulation of the neutralization process. A full understanding of how the erosion process is influenced by the downstream plasma condition may require the detailed simulation of the neutralization processes and the downstream plasma.

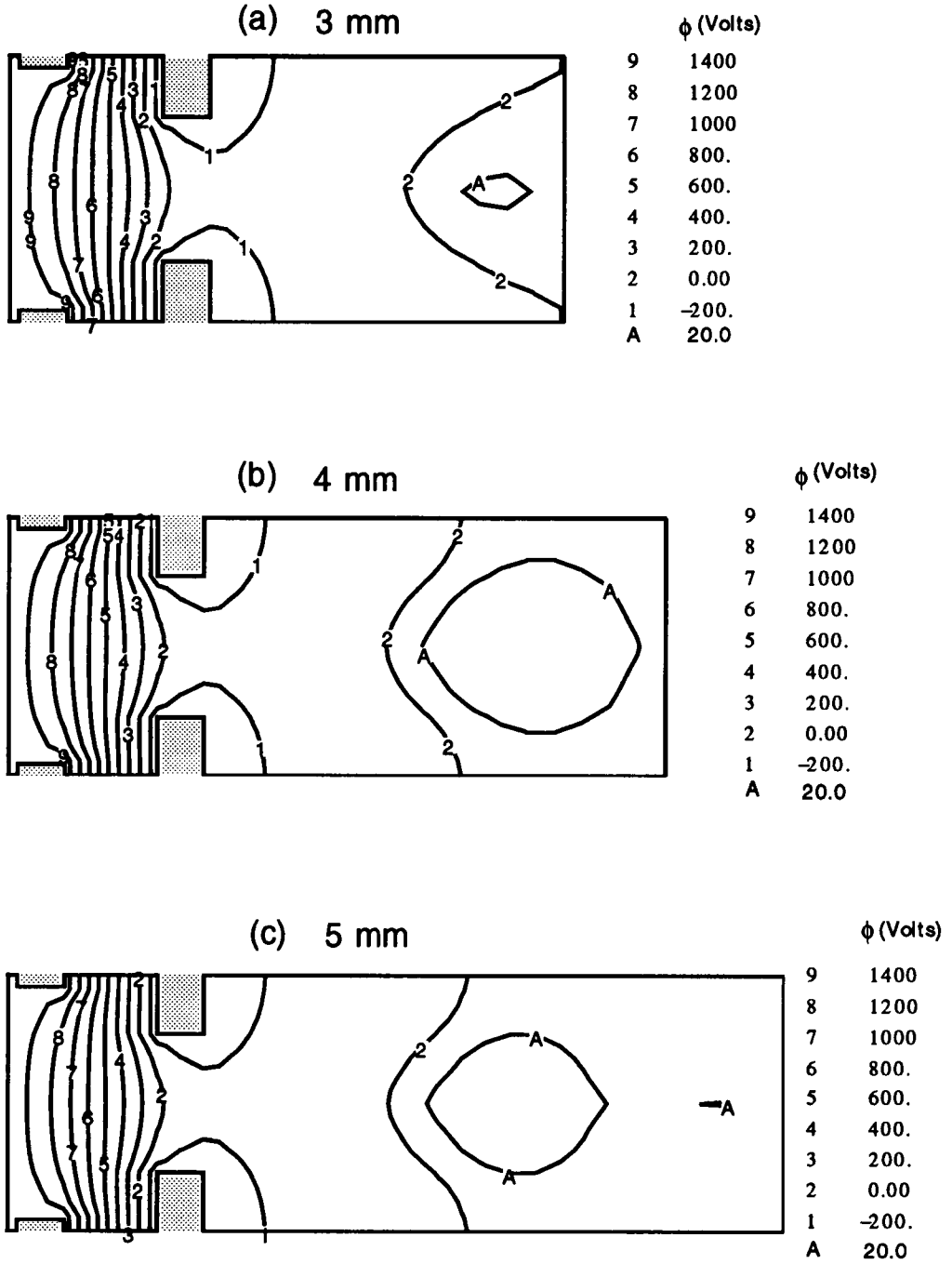

Figure 3.12. Comparison of computed electric potential contours with the distance between the accelerator grid and downstream boundary equal to: (a) 3 *mm*, (b) 4 *mm*, and (c) 5 *mm*. The assumed boundary condition is: $\phi_e = 0$.

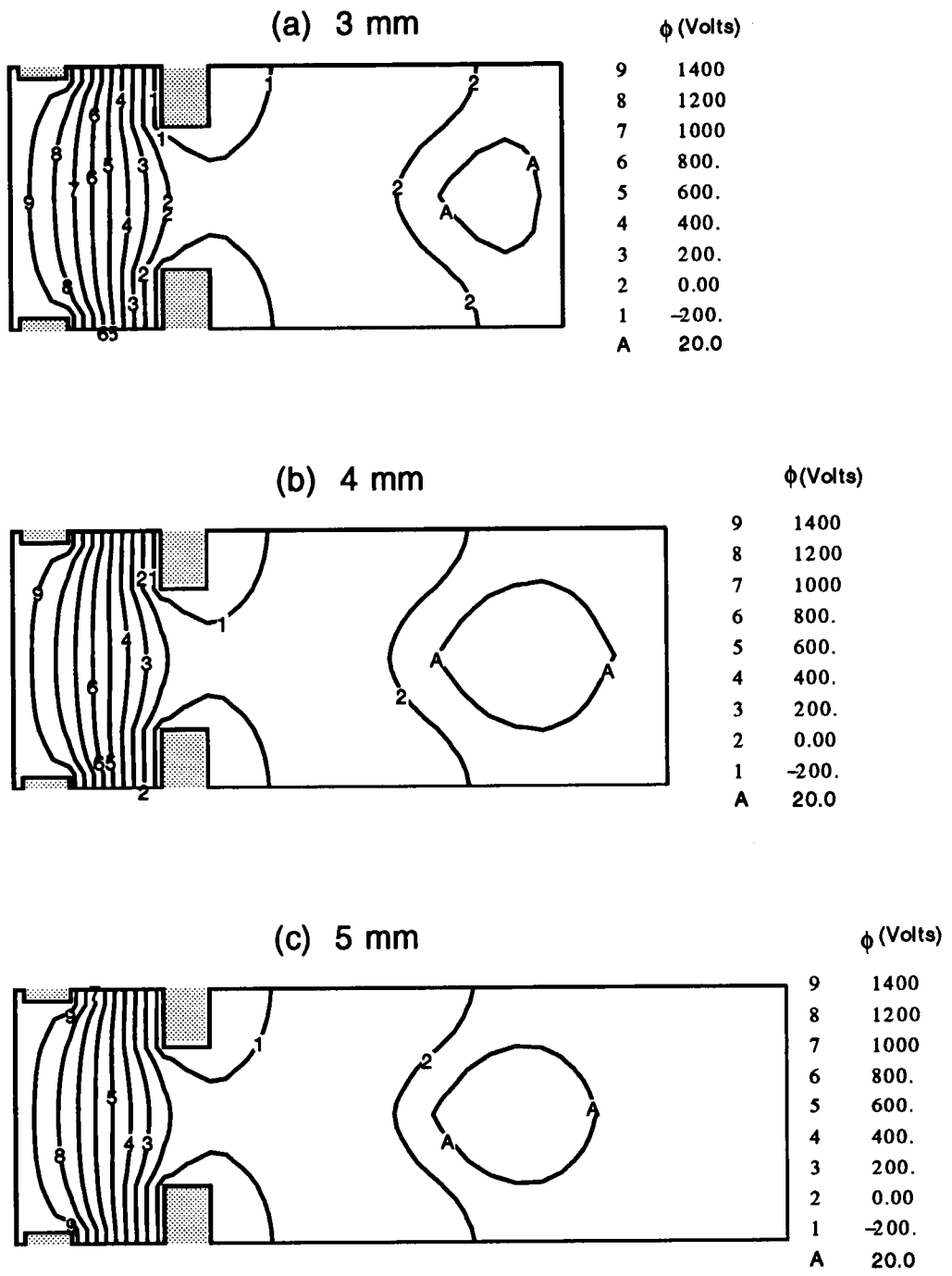

Figure 3.13. Comparison of computed electric potential contours with the distance between the accelerator grid and downstream boundary equal to: (a) 3 *mm*, (b) 4 *mm*, and (c) 5 *mm*. The assumed boundary condition is: $(\frac{\partial^2 \phi}{\partial z^2})_e = 0$.

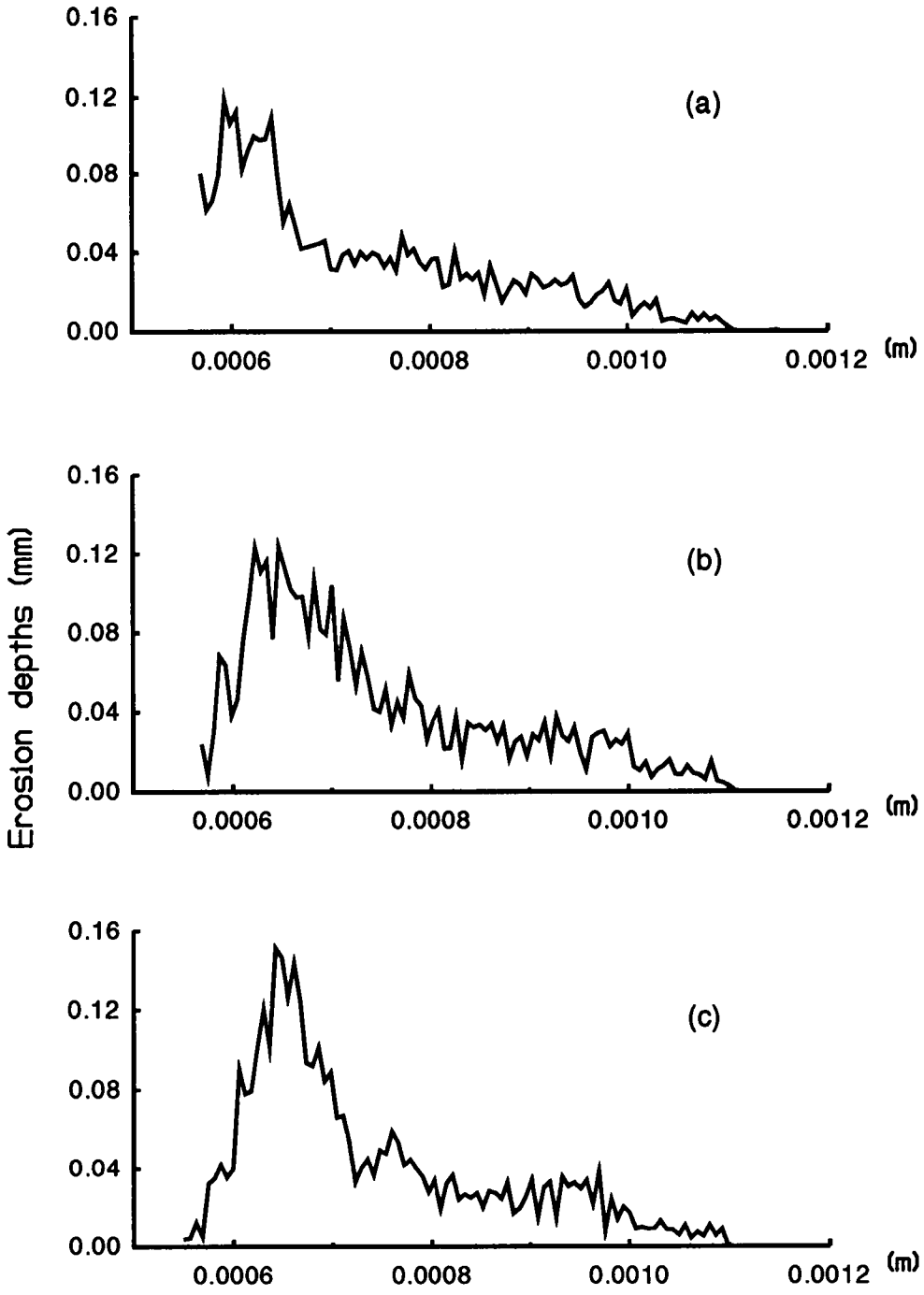

Figure 3.14. Comparison of computed erosion depths per 1000 hrs of operation of the downstream accelerator grid surface as a function of radius for different distances between the accelerator grid and assumed boundary position: (a) 3 *mm*, (b) 4 *mm*, and (c) 5 *mm*. The assumed boundary condition is: $\phi_e = 0$.

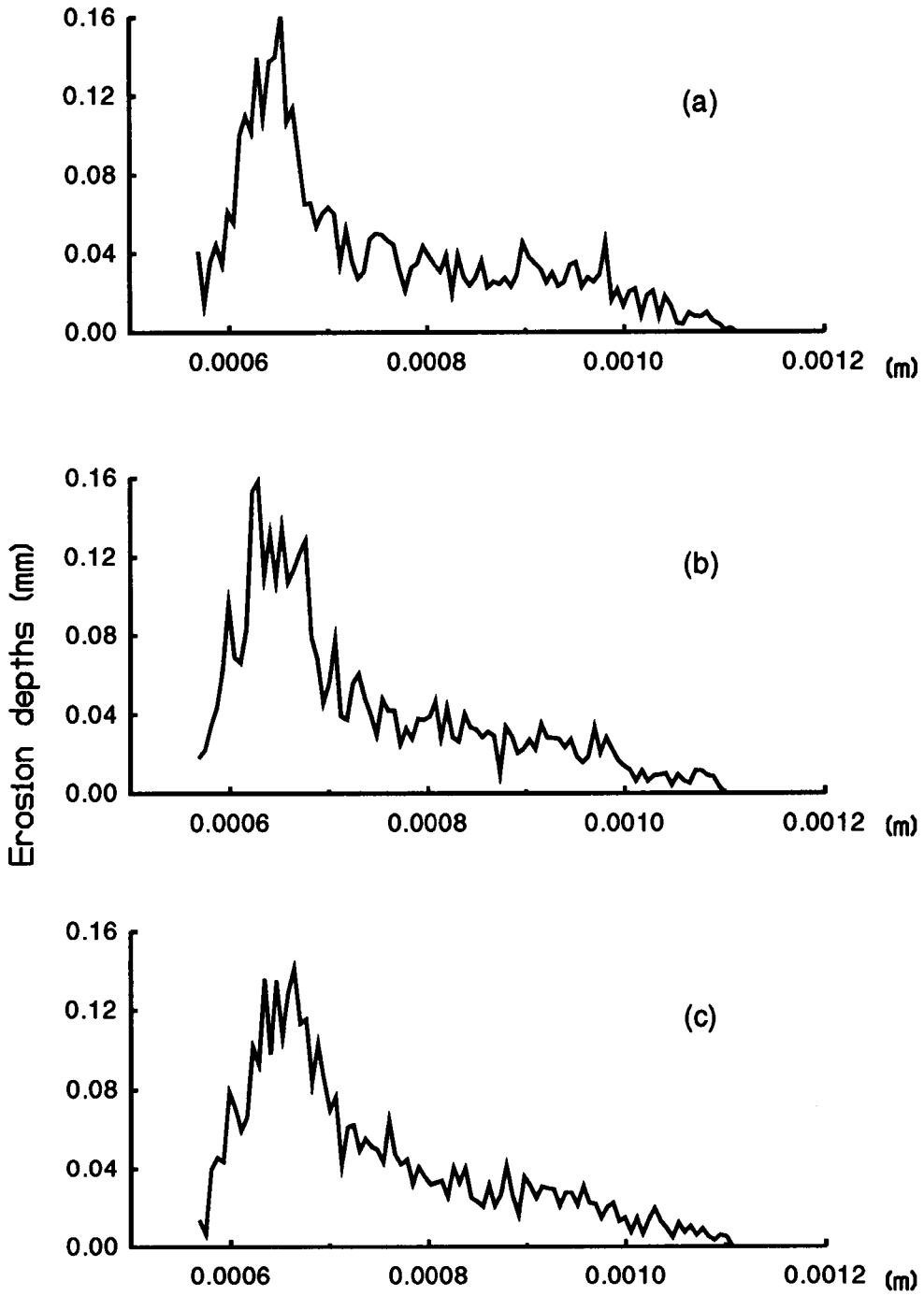

Figure 3.15. Comparison of computed erosion depths per 1000 hrs of operation of the downstream accelerator grid surface as a function of radius for different distances between the accelerator grid and assumed boundary position: (a) 3 *mm*, (b) 4 *mm*, and (c) 5 *mm*. The assumed boundary condition is: $(\frac{\partial^2 \phi}{\partial z^2})_e = 0$.

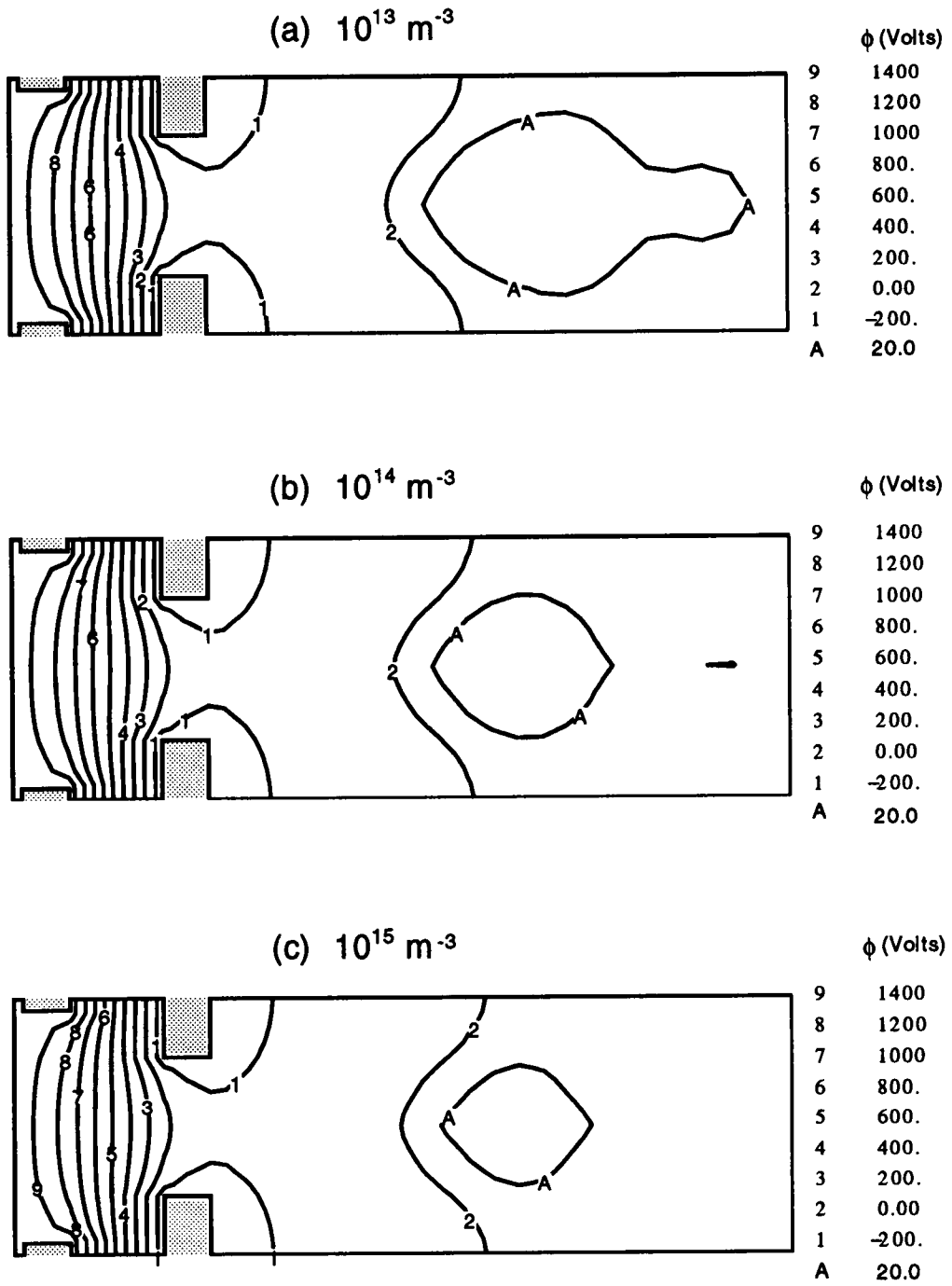

Figure 3.16. Comparison of computed electric potential contours for different downstream plasma densities: (a) $10^{13}m^{-3}$, (b) $10^{14}m^{-3}$, and (c) $10^{15}m^{-3}$. The assumed downstream boundary condition is: $\phi_e = 0$.

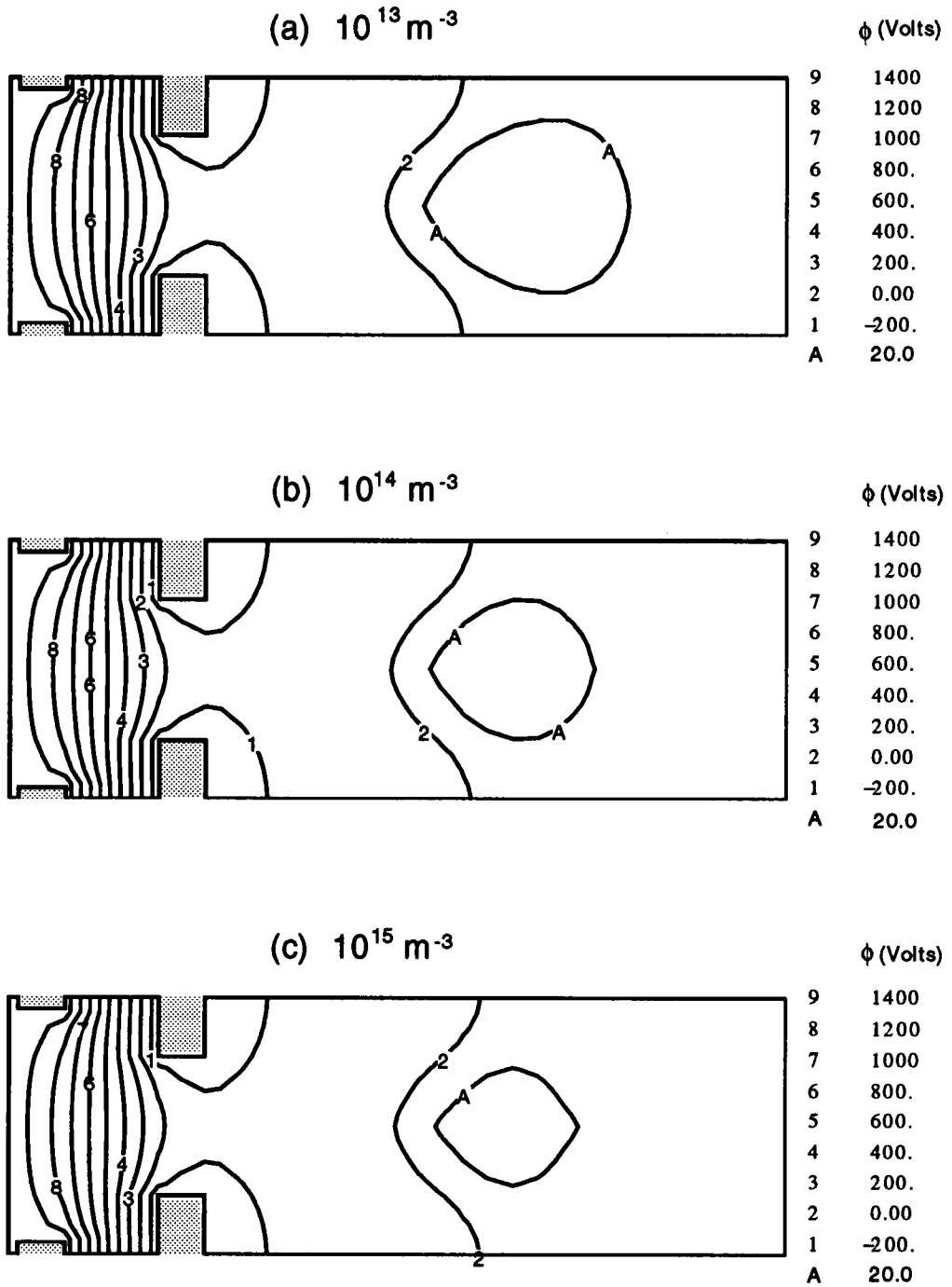

Figure 3.17. Comparison of computed electric potential contours for different downstream plasma densities: (a) $10^{13}m^{-3}$, (b) $10^{14}m^{-3}$, and (c) $10^{15}m^{-3}$. The assumed downstream boundary condition is: $(\frac{\partial^2\phi}{\partial z^2})_e = 0$.

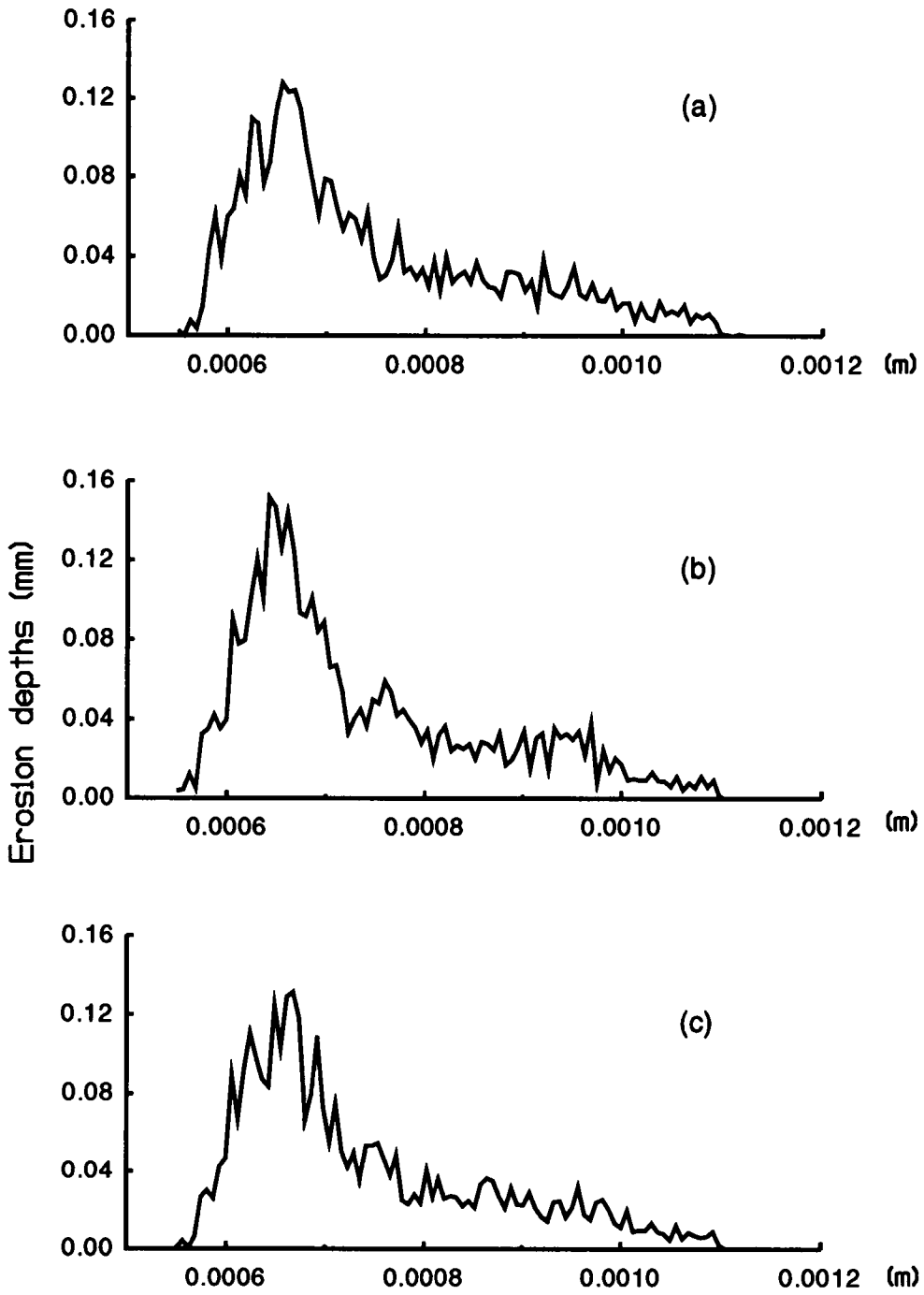

Figure 3.18. Comparison of computed erosion depths per 1000 hrs of operation of the downstream accelerator grid surface as a function of radius for different downstream plasma densities: (a) $10^{13}m^{-3}$, (b) $10^{14}m^{-3}$, and (c) $10^{15}m^{-3}$. The assumed downstream boundary condition is: $\phi_e = 0$.

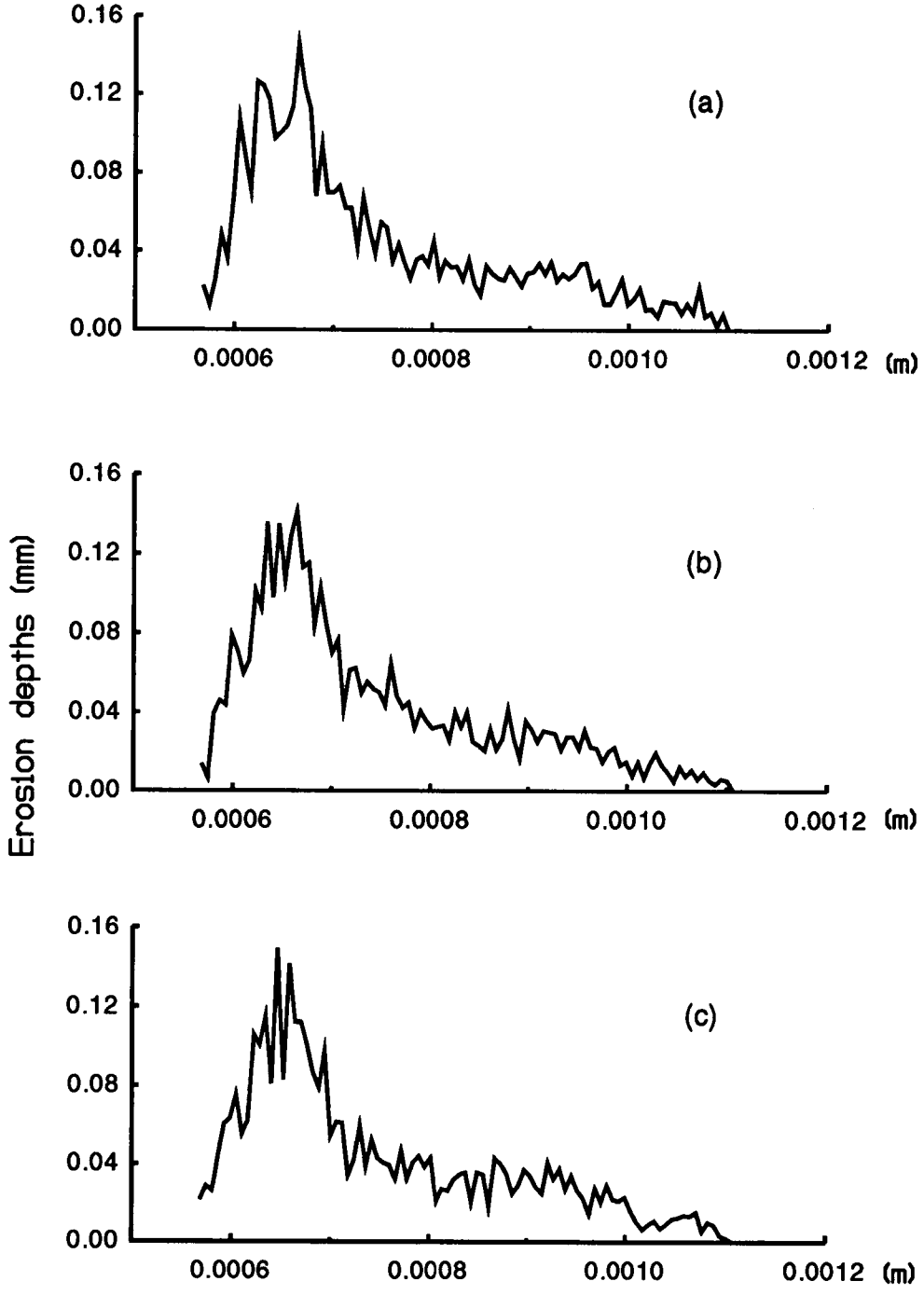

Figure 3.19. Comparison of computed erosion depths per 1000 hrs of operation of the downstream accelerator grid surface as a function of radius for different downstream plasma densities: (a) $10^{13}m^{-3}$, (b) $10^{14}m^{-3}$, and (c) $10^{15}m^{-3}$. The assumed downstream boundary condition is: $(\frac{\partial^2\phi}{\partial z^2})_e = 0$.

3.4. Conclusions for the Two-Dimensional Model

The two-dimensional axisymmetric particle-in-cell and Monte Carlo model is capable of providing details of the ion flow in the exhaust beam and the charge exchange collisions which are known to be responsible for the erosion of the accelerator grid.

The shape and the location of the downstream zero volt electric potential plane is not sensitive to what boundary condition is chosen and where the assumed boundary is located if the assumed downstream boundary is far downstream of the accelerator grid.

The peak value of the downstream potential hill does change with the downstream plasma density but, because of the nature of the electron distribution assumed in this calculation, the difference in the peak values are not so large that the erosion rates show significant differences.

The largest sputtering erosion rate, according to the calculations, occurs some distance away from the grid holes. For the usual hexagonal geometry of the extraction grids, this would seem to imply that the maximum sputtering occurs between grid apertures, rather than at the edges of the apertures, as is found experimentally. Direct confirmation of observed erosion patterns requires a three-dimensional extension of the code, in which the hexagonal symmetry of conventional grid systems is accounted. The next chapter deals with the development of such a three-dimensional model.

CHAPTER IV

THREE-DIMENSIONAL MODEL

Since the actual extraction grid system of an ion engine consists of arrays with many adjacent apertures, the two dimensional model with a single set of apertures is necessarily limited in predicting three-dimensional effects of the system. Such three-dimensional effects are, however, of significant importance for an analysis of grid lifetime. Specifically, experimental observations of grid erosion show that the maximum erosion occurs at the geometric center of a group of adjacent apertures (MacRae and Mercer 1991; Patterson and Verhey 1990; Rawlin 1988; Pawlik and Reader 1967). Therefore, a three-dimensional model is required to take into consideration the geometric effects of the generally hexagonal symmetry of the array of apertures which comprise the screen and accelerator grids. In the following section, the discretization of Poisson's equation for a three-dimensional geometry using Cartesian coordinates is discussed. The PIC weighting factor used in the triangular mesh is described in section **4.2**. In section **4.3**, an example calculation is given and comparisons of sputtering erosion rates between the two-dimensional and three-dimensional models is described. Finally, the conclusions for the three-dimensional model will be given in section **4.4**.

4.1. Discretization of Poisson's Equation

The discretization of Poisson's equation in the z-direction, in Fig. 2.4, is similar to the two-dimensional model described in Chapter III, but the discretization of Poisson's equation in the transverse direction, the xy-plane, is different. Since the computational domain in the transverse direction is irregular, a nonuniform

triangular mesh is used. The type of triangulation used here in the xy-plane is topological regular, i.e., it is topologically equivalent to an equilateral triangle array in which six triangles meet at every interior mesh point. Along with the primary triangle mesh (in the xy-plane), a secondary mesh is introduced by drawing connecting lines between the "center of mass "of every triangle and the center of each of the three sides of the triangle. As a consequence, every mesh point (ij, k) is now assigned a unique twelve-sided polygon volume element which is called the control volume. Fig. 4.1 shows such a control volume and its corresponding volume faces, a dodecagon, surrounding the mesh point (ij, k) in the xy-plane. Fig. 4.2 shows a 3D view.

Actually, the discretization equations of Poisson's equation in the transverse direction are formed by the control-volume-based finite-element method (Patankar 1980); i.e., Poisson's equation is integrated over the control volume shown in Fig. 4.1. This construction of the control volume was proposed by Winslow (1967).

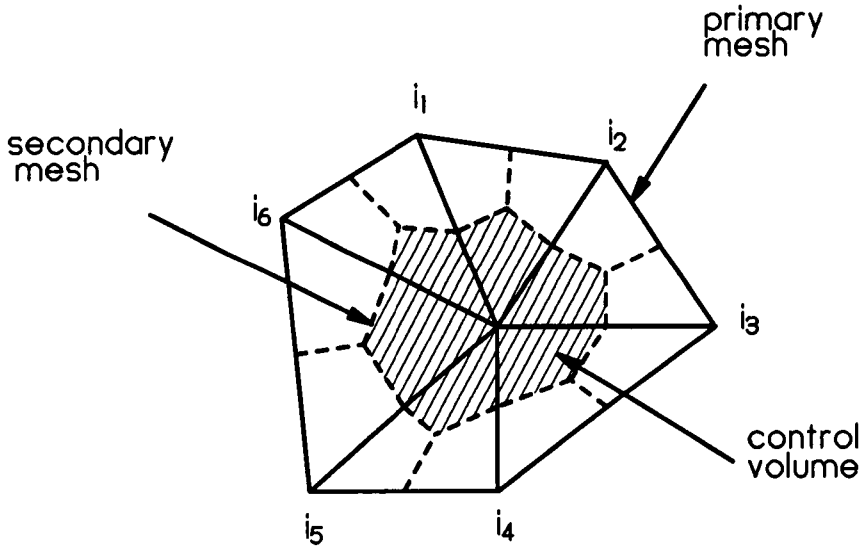

Figure 4.1. Primary and secondary mesh lines.

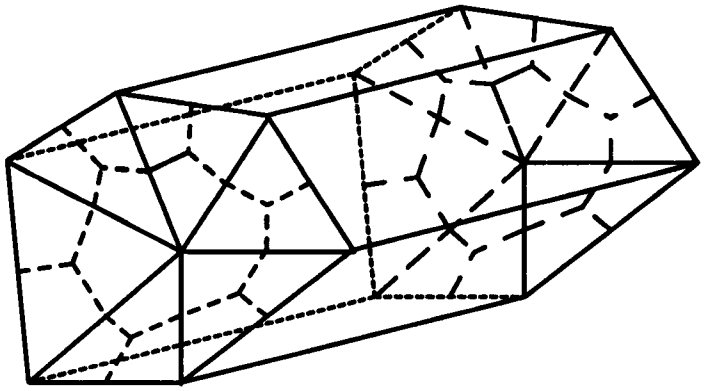

Figure 4.2. Three-dimensional view of Fig. 4.1.

To obtain the discretization equation for Poisson's equation at mesh point (ij,k), Eq.(2.4) is integrated with a corresponding volume element, $dv_{ij,k}$, centered on (ij,k):

$$\iiint_{dv_{ij,k}} \nabla^2\phi dv = -\iiint_{dv_{ij,k}} \frac{\rho}{\epsilon_0} dv \tag{4.1}$$

To guarantee flux conservation, Gauss' law is applied to Eq.(4.1):

$$\iint_{dA_{ij,k}} \nabla\phi \cdot d\mathbf{A} = -\iiint_{dv_{ij,k}} \frac{\rho}{\epsilon_0} dv. \tag{4.2}$$

Since the volume element has two surfaces in the z-direction and twelve surfaces in transverse directions, and

$$\hat{\mathbf{a}}_t \perp \hat{\mathbf{a}}_z, \tag{4.3}$$

where $\hat{\mathbf{a}}_t$ and $\hat{\mathbf{a}}_z$ are normalized area direction vectors in the transverse and z-directions, respectively, Eq.(4.2) can be written as

$$\sum_{l=1}^{12} \nabla\phi_{t,l} \cdot \hat{\mathbf{a}}_{t,l} dA_{t,l} + \sum_{l=1}^{2} \nabla\phi_{z,l} \cdot \hat{\mathbf{a}}_{z,l} dA_{z,l} = -\frac{\rho_{ij,k}}{\epsilon_0} dv_{ij,k}, \tag{4.4}$$

or,

$$R_t + R_z = -Q_{ij,k}, \tag{4.5}$$

where R_t is the total flux in the transverse direction:

$$R_t = \sum_{l=1}^{12} \nabla\phi_{t,l} \cdot \hat{\mathbf{a}}_{t,l} dA_{t,l}, \tag{4.6}$$

R_z is the total flux in the z-direction:

$$R_z = \sum_{l=1}^{2} \nabla\phi_{z,l} \cdot \hat{\mathbf{a}}_{z,l} dA_{z,l}, \tag{4.7}$$

and

$$Q_{ij,k} = \frac{\rho_{ij,k}}{\epsilon_0} dv_{ij,k}. \tag{4.8}$$

The discretization method for these directions will be discussed separately.

4.1.1. Discretization in the Transverse Direction

Winslow's method (Winslow 1967) is used for discretization in the transverse direction. The basic assumptions of the method are: (a) the values of ϕ are defined at triangle vertices; (b) ρ is assumed to be constant over each secondary mesh dodecagon.

(a) Interior mesh points:

To calculate the flux across the control volume faces that fall within the element, a shape function for the electric potential, ϕ, is needed, which describes the variation of ϕ over a triangular element. Since three ϕ values at three mesh points are known for each triangle element, the shape function of ϕ used in this study is assumed to be a linear function of x and y within every triangle:

$$\phi = a + bx + cy, \tag{4.9}$$

where the constants a, b, and c are expressed in terms of the three corner-mesh values of ϕ. Thus each triangle has a constant electric field vector associated with it,

$$\mathbf{E_t} = -\nabla\phi_{t,i_{n+\frac{1}{2}}}, \tag{4.10}$$

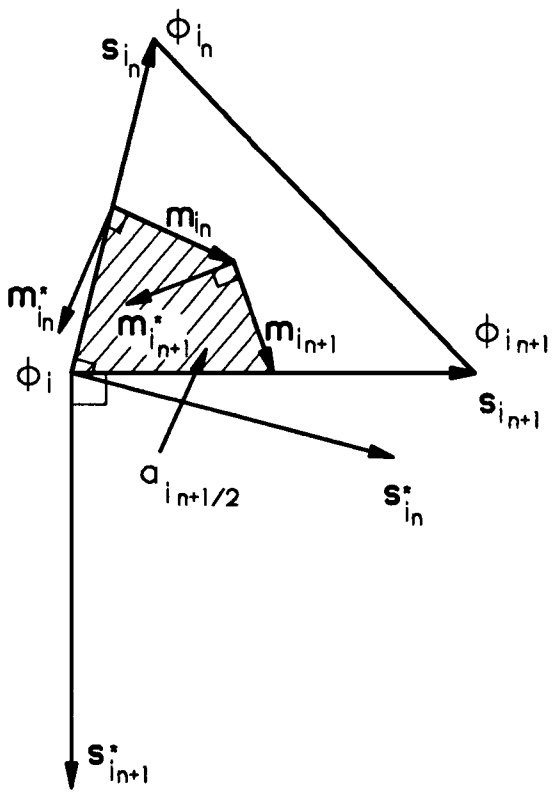

Figure 4.3. The vectors used in the discretization of the Poisson's equation on the triangular mesh.

where the subscript $i_{n+\frac{1}{2}}$ represents the triangle defined by the two side vectors $\mathbf{s}_{i_n}$, $\mathbf{s}_{i_{n+1}}$, with values ϕ_{i_n}, $\phi_{i_{n+1}}$ at the respective vertices as shown in Fig. 4.3. Hence, the gradient $\nabla\phi_{t,i_{n+\frac{1}{2}}}$ inside the triangle with index $i_{n+\frac{1}{2}}$ is uniquely determined by the values of ϕ at the three corner-mesh points of the triangle,

$$\phi_{i_n} - \phi_i = \mathbf{s}_{i_n} \cdot \nabla\phi_{t,i_{n+\frac{1}{2}}} \tag{4.11}$$

$$\phi_{i_{n+1}} - \phi_i = \mathbf{s}_{i_{n+1}} \cdot \nabla\phi_{t,i_{n+\frac{1}{2}}} \tag{4.12}$$

or

$$\begin{pmatrix} s_{i_n,x} & s_{i_n,y} \\ s_{i_{n+1},x} & s_{i_{n+1},y} \end{pmatrix} \begin{pmatrix} \nabla\phi_x \\ \nabla\phi_y \end{pmatrix}_{i_{n+\frac{1}{2}}} = \begin{pmatrix} \Delta\phi_{i_n} \\ \Delta\phi_{i_{n+1}} \end{pmatrix} \tag{4.13}$$

where $s_{i_n,x}$ and $s_{i_n,y}$ are defined as

$$\mathbf{s}_{i_n} = s_{i_n,x}\hat{\mathbf{i}} + s_{i_n,y}\hat{\mathbf{j}}, \tag{4.14}$$

$\nabla\phi_x$ and $\nabla\phi_y$ are defined as

$$\nabla\phi = \nabla\phi_x\hat{\mathbf{i}} + \nabla\phi_y\hat{\mathbf{j}}, \tag{4.15}$$

and

$$\Delta\phi_{i_n} = \phi_{i_n} - \phi_i. \tag{4.16}$$

Thus, the $\nabla\phi_{t,i_{n+\frac{1}{2}}}$ for each triangle can be obtained from Eq.(4.13):

$$\nabla\phi_{t,i_{n+\frac{1}{2}}} = \frac{\Delta\phi_{i_{n+1}}(-s_{i_n,y}\hat{\mathbf{i}} + s_{i_n,x}\hat{\mathbf{j}}) - \Delta\phi_{i_n}(-s_{i_{n+1},y}\hat{\mathbf{i}} + s_{i_{n+1},x}\hat{\mathbf{j}})}{s_{i_n,x}s_{i_{n+1},y} - s_{i_n,y}s_{i_{n+1},x}}. \tag{4.17}$$

Define

$$\mathbf{s}^* = s_y\hat{\mathbf{i}} - s_x\hat{\mathbf{j}}; \tag{4.18}$$

then

$$\mathbf{s}^*_{\mathbf{i_n}} = s_{i_n,y}\hat{\mathbf{i}} - s_{i_n,x}\hat{\mathbf{j}} \tag{4.19}$$

$$\mathbf{s}^*_{\mathbf{i_{n+1}}} = s_{i_{n+1},y}\hat{\mathbf{i}} - s_{i_{n+1},x}\hat{\mathbf{j}} \tag{4.20}$$

and Eq.(4.17) becomes

$$\nabla\phi_{t,i_{n+\frac{1}{2}}} = \frac{\Delta\phi_{i_n}\mathbf{s}^*_{i_{n+1}} - \Delta\phi_{i_{n+1}}\mathbf{s}^*_{i_n}}{\mathbf{s}_{i_n}\cdot\mathbf{s}^*_{i_{n+1}}}. \tag{4.21}$$

Hence, the flux, in the transverse direction, can be written as

$$R_t = \sum_{n=1}^{6} \nabla\phi_{t,i_{n+\frac{1}{2}}}\cdot\hat{\mathbf{a}}_{t,i_{n+\frac{1}{2}}}dA_{t,i_{n+\frac{1}{2}}}, \tag{4.22}$$

where

$$\hat{\mathbf{a}}_{t,i_{n+\frac{1}{2}}}dA_{t,i_{n+\frac{1}{2}}} = -dz_k(\mathbf{m}^*_{i_n} + \mathbf{m}^*_{i_{n+1}}) \tag{4.23}$$

and

$$\mathbf{m}^*_{i_n} = m_{i_n,y}\hat{\mathbf{i}} - m_{i_{n+1},y}\hat{\mathbf{j}}. \tag{4.24}$$

Since

$$\mathbf{m}_{i_n} + \mathbf{m}_{i_{n+1}} = \frac{1}{2}(\mathbf{s}_{i_{n+1}} - \mathbf{s}_{i_n}) \tag{4.25}$$

then

$$\mathbf{m}^*_{i_n} + \mathbf{m}^*_{i_{n+1}} = \frac{1}{2}(\mathbf{s}^*_{i_{n+1}} - \mathbf{s}^*_{i_n}). \tag{4.26}$$

Define

$$R_{t,i_{n+\frac{1}{2}}} = \nabla\phi_{t,i_{n+\frac{1}{2}}} \cdot \hat{\mathbf{a}}_{t,i_{n+\frac{1}{2}}} dA_{t,i_{n+\frac{1}{2}}}, \tag{4.27}$$

where $R_{t,i_{n+\frac{1}{2}}}$ is the flux contribution from the triangle $i_{n+\frac{1}{2}}$ shown in Fig. 4.3 to the secondary mesh volume element. Substitution of Eqs.(4.21), (4.23), and (4.26) into Eq.(4.27) then gives:

$$\begin{aligned} R_{t,i_{n+\frac{1}{2}}} &= -\frac{dz_k}{2}\nabla\phi_{t,i_{n+\frac{1}{2}}} \cdot (\mathbf{s}^*_{i_{n+1}} - \mathbf{s}^*_{i_n}) \\ &= -\frac{dz_k}{2}\frac{\Delta\phi_{i_n}\mathbf{s}^*_{i_{n+1}} - \Delta\phi_{i_{n+1}}\mathbf{s}^*_{i_n}}{\mathbf{s}_{i_n} \cdot \mathbf{s}^*_{i_{n+1}}} \cdot (\mathbf{s}^*_{i_{n+1}} - \mathbf{s}^*_{i_n}) \\ &= \frac{dz_k}{2}\frac{\Delta\phi_{i_n}\mathbf{s}_{i_{n+1}} \cdot (\mathbf{s}_{i_{n+1}} - \mathbf{s}_{i_n}) - \Delta\phi_{i_{n+1}}\mathbf{s}_{i_n} \cdot (\mathbf{s}_{i_{n+1}} - \mathbf{s}_{i_n})}{\mathbf{s}^*_{i_n} \cdot \mathbf{s}_{i_{n+1}}}, \end{aligned} \tag{4.28}$$

where the relations

$$\mathbf{u}^* \cdot \mathbf{v}^* = \mathbf{u} \cdot \mathbf{v} \tag{4.29}$$

and

$$\mathbf{u} \cdot \mathbf{v}^* = -\mathbf{u}^* \cdot \mathbf{v} \tag{4.30}$$

have been used.

Hence, the total flux in the transverse direction, R_t, to the finite volume $dv_{ij,k}$ centered at (ij,k) is equal to

$$R_t = \frac{dz_k}{2}\sum_{n=1}^{6}\frac{\Delta\phi_{i_n}\mathbf{s}_{i_{n+1}} \cdot (\mathbf{s}_{i_{n+1}} - \mathbf{s}_{i_n}) - \Delta\phi_{i_{n+1}}\mathbf{s}_{i_n} \cdot (\mathbf{s}_{i_{n+1}} - \mathbf{s}_{i_n})}{\mathbf{s}^*_{i_n} \cdot \mathbf{s}_{i_{n+1}}}. \tag{4.31}$$

Since the sum is cyclic, Eq.(4.31) can be rewritten as

$$R_t = \frac{dz_k}{2} \sum_{n=1}^{6} \left[\frac{\mathbf{s}_{i_{n+1}} \cdot (\mathbf{s}_{i_{n+1}} - \mathbf{s}_{i_n})}{\mathbf{s}^*_{i_n} \cdot \mathbf{s}_{i_{n+1}}} - \frac{\mathbf{s}_{i_{n-1}} \cdot (\mathbf{s}_{i_n} - \mathbf{s}_{i_{n-1}})}{\mathbf{s}^*_{i_{n-1}} \cdot \mathbf{s}_{i_n}} \right] \Delta\phi_{i_n}. \tag{4.32}$$

Note that this expression for the flux involves seven values of the electric potential, namely at the seven primary mesh points in Fig. 4.1.

(b) Transverse boundary mesh points:

There are two types of boundary mesh points in the transverse direction. Fig. 4.4(a) shows one of the three corners of the computational domain, and Fig. 4.4(b) shows the boundary mesh point not at the corners. For the case shown in Fig. 4.4(a), since $\mathbf{E}$ is required to be perpendicular to lines $0-1$ and $0-2$,

$$\int_{1\prime-0-2\prime} \mathbf{E} \cdot d\mathbf{s} = 0. \tag{4.33}$$

The same thing occurs for the boundary points shown in Fig. 4.4(b),

$$\int_{1'-0-4'} \mathbf{E} \cdot d\mathbf{s} = 0. \tag{4.34}$$

Eqs.(4.33) and (4.34) mean that the difference equations for ϕ at the boundary points are identical to those for interior points, except that only contributions from interior triangles are taken into account. That is, the corresponding sums in Eq.(4.32) are only from $n = 1$ to $n = 2$ in Fig. 4.4(a), and from $n = 1$ to $n = 4$ in Fig. 4.4(b).

4.1.2. Discretization in z-Direction

Similar to the two-dimensional model, the flux contribution from the z-direction is given by the following equation:

$$R_z = \nabla\phi_{z,k-1} \cdot \hat{\mathbf{a}}_{z,k-1} dA_{z,k-1} + \nabla\phi_{z,k+1} \cdot \hat{\mathbf{a}}_{z,k+1} dA_{z,k+1}. \tag{4.35}$$

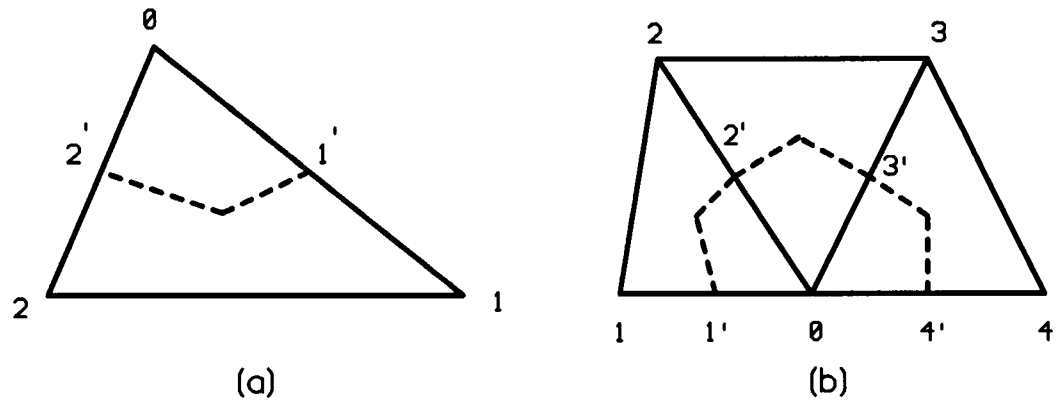

Figure 4.4. Boundary mesh points with neighboring interior mesh points, and secondary polygon: (a) boundary point with two interior mesh points and (b) boundary point with four interior mesh points.

Since

$$-\hat{\mathbf{a}}_{z,k-1} = \hat{\mathbf{a}}_{z,k+1} = \hat{\mathbf{k}}, \tag{4.36}$$

$$dA_{z,k-1} = dA_{z,k+1} = \sum_{n=1}^{6} a_{i_{n+\frac{1}{2}}}, \tag{4.37}$$

$$\nabla\phi_{z,k-1} = \frac{\phi_{ij,k} - \phi_{ij,k-1}}{dz_{k-1}}\hat{\mathbf{k}}, \tag{4.38}$$

and

$$\nabla\phi_{z,k+1} = \frac{\phi_{ij,k+1} - \phi_{ij,k}}{dz_{k+1}}\hat{\mathbf{k}}, \tag{4.39}$$

where $a_{i_{n+\frac{1}{2}}}$ is the area shown in Fig. 4.3, then, Eq.(4.35) becomes

$$R_z = dA_{z,k}\left(\frac{1}{dz_{k-1}}(\phi_{ij,k-1} - \phi_{ij,k}) + \frac{1}{dz_{k+1}}(\phi_{ij,k+1} - \phi_{ij,k})\right). \tag{4.40}$$

4.1.3. The Final Discretization Equations

By substituting Eqs.(4.32) and (4.40) into Eq.(4.5), the discretization equation of Poisson's equation at mesh point (ij,k) can be written as

$$\sum_{n=1}^{6} w_{t,n}\Delta\phi_{n,k} + \sum_{n=1}^{2} w_{z,n}(\phi_{ij,k+(-1)^n} - \phi_{ij,k}) = -Q_{ij,k} \tag{4.41}$$

where

$$w_{t,n} = \frac{dz_k}{2}\left(\frac{\mathbf{s}_{i_{n+1}} \cdot (\mathbf{s}_{i_{n+1}} - \mathbf{s}_{i_n})}{\mathbf{s}^*_{i_n} \cdot \mathbf{s}_{i_{n+1}}} - \frac{\mathbf{s}_{i_{n-1}} \cdot (\mathbf{s}_{i_n} - \mathbf{s}_{i_{n-1}})}{\mathbf{s}^*_{i_{n-1}} \cdot \mathbf{s}_{i_n}}\right), \tag{4.42}$$

$$w_{z,n} = dA_{z,k}\frac{1}{dz_{k+(-1)^n}}, \tag{4.43}$$

and

$$dv_{ij,k} = dz_k dA_{z,k}, \tag{4.44}$$

where

$$dA_{z,k} = \sum_{n=1}^{6} a_{i_{n+\frac{1}{2}}}. \tag{4.45}$$

In summary, the finite difference equations for all interior and boundary mesh points can be written in matrix form:

$$\begin{pmatrix} A_{1,1} & A_{1,2} & & & & & & & \\ A_{2,1} & A_{2,2} & A_{2,3} & & & & & & \\ & A_{3,2} & A_{3,3} & A_{3,4} & & & & & \\ & & \ddots & \ddots & \ddots & & & & \\ & & & A_{k,k-1} & A_{k,k} & A_{k,k+1} & & & \\ & & & & \ddots & \ddots & \ddots & & \\ & & & & & A_{n-1,n-2} & A_{n-1,n-1} & A_{n-1,n} & \\ & & & & & & A_{n,n-1} & A_{n,n} \end{pmatrix} \cdot \begin{pmatrix} \psi_1 \\ \psi_2 \\ \psi_3 \\ \vdots \\ \psi_k \\ \vdots \\ \psi_{n-1} \\ \psi_n \end{pmatrix}$$

$$= \begin{pmatrix} s_1 \\ s_2 \\ s_3 \\ \vdots \\ s_k \\ \vdots \\ s_{n-1} \\ s_n \end{pmatrix} \tag{4.46}$$

where n is the maximum of k.

In this matrix equation, the matrix on the left-hand side of Eq.(4.46) is a block tridiagonal matrix as shown. These blocks are also sparse, the diagonal

blocks containing not more than seven nonzero elements in every row, and the off-diagonal blocks only having one nonzero element in any row. Each element ψ_k represents a column vector with components $\phi_{ij,k}$ for $ij = 1, m$, where m is the maximum of ij. The elements of the right-hand side of Eq.(4.46) are vectors with elements

$$s_{ij,k} = -Q_{ij,k}, \qquad ij = 1, m. \tag{4.47}$$

At the far upstream and far downstream positions, and at the screen and accelerator grid boundaries, the right-hand side of Eq.(4.46) also contains values of the boundary potentials, similar as for the axisymetric calculation in Chapter **III** (see Eqs.(3.31), (3.35), and (3.42)).

The same solution procedure is employed as for the axisymmetric case, described in section **3.1.3**. However, a significant difference exists between the sizes of the respective arrays. Namely, whereas, for the axisymmetric calculation, the size of the blocks is equal to the number of transverse (radial) grid points N, the size of the blocks for the 3D calculation is $\frac{1}{2}N^2$. Therefore, a large fraction of the *CPU* time is spent on solving Poisson's equation at each time iteration.

4.2. Weighting Factor for the Triangular Mesh

For the three-dimensional model, area weighting is used for particle-to-grid interpolation. This area weighting is performed as indicated in Fig. 4.5:

$$\begin{aligned} q_A &= q_p \frac{a}{\text{area}} \\ q_B &= q_p \frac{b}{\text{area}} \\ q_C &= q_p \frac{c}{\text{area}} \end{aligned} \tag{4.48}$$

where q_p is the particle charge and

$$\text{area} = a + b + c. \tag{4.49}$$

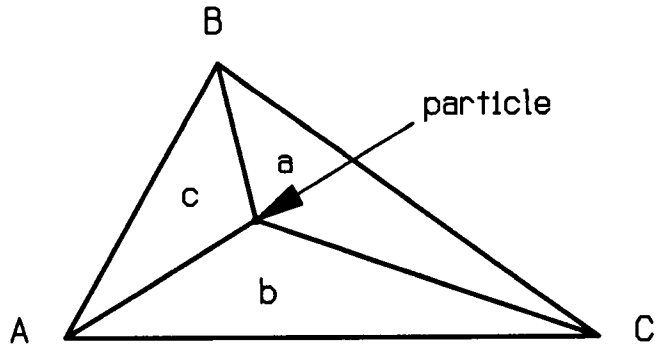

Figure 4.5. Area weighting for the triangle mesh element. Areas are assigned to grid points; *i.e.*, area a to grid A, b to B, and c to C.

4.3. Example Calculations

For the most part, the two-dimensional and three-dimensional models give similar results for average velocity distributions, ion number densities, and potential variations along the ion beam axis. Production of charge exchange ions is also similar for the two models. Therefore, the calculation results shown in this section will concentrate primarily on the erosion of the accelerator grid and on the transverse potential contours that give rise to the pitted erosion patterns of the hexagonal aperture array which were observed in experiments.

The calculation was performed on a mesh containing 162 grid points in the transverse, and 42 grid points in the axial directions, using a timestep of 1.1×10^{-9} seconds. The calculation was terminated after 5000 timesteps, at which time the computational domain contained about 60,000 simulation particles. The total *CPU* time was about 9 hours (with IBM RISC SYSTEM/6000/550 computer).

4.3.1. Geometry and Plasma Conditions

The geometry parameters of the computational domain and the potentials of the plasma and electrodes were chosen to correspond the experimental configura-

Table 4.1 Parameters using in 3D calculations

Screen hole diameter	(mm)	1.91
Accelerator hole diameter	(mm)	1.52
Thickness of both grids	(mm)	0.51
Grid-to-grid distance	(mm)	1.0
Screen grid open fraction		0.67
Plasma potential	(V)	1828
Screen grid potential	(V)	1800
Accelerator grid potential	(V)	-510
Electron temperature	(eV)	1.5
Ion temperature	(K)	1000
Ion extraction velocity	(m/s)	400
Upstream ion density	(m^{-3})	$1x10^{18}$
Neutral gas density	(m^{-3})	$5x10^{18}$

tion used by Rawlin (1988), except the beam current used in the calculation which was one order of magnitude less than Rawlin's. These input parameters used in the calculations are given in Table 4.1. Again, the calculations were performed for operation of the thruster using xenon propellant.

Next, the comparison of calculated and experimentally observed sputtering erosion is shown first. Then the calculated transverse electric potential contours are given. These explicitly show how the pitted erosion pattern is a direct consequence of this transverse electric field distribution in the downstream region of the thruster. Finally, comparison of two- and three-dimensional models of grid erosion is given.

4.3.2. Comparison of Calculated and Experimentally Observed Grid Erosion

Several xenon ion thruster lifetime experiments (Patterson and Verhey 1990, Rawlin 1988, and Brewer 1970) have shown that accelerator grid erosion is the most likely limitation of ion engine lifetime. Significant grid erosion occurred at the downstream surface of the accelerator grid, as shown in Figs. 4.6 and 4.7, taken from Patterson and Verhey (1990) and Rawlin (1988). From Figs. 4.6 and 4.7, it can be seen that the maximum grid erosion occurs at the geometry centers between apertures and the erosion holes are triangular in shape. Such grid erosion is caused by the charge exchange ions which are created in the deceleration region inside the ion beam plume and, therefore, are accelerated back toward the accelerator grid and strike its downstream surface.

The calculated sputtering erosion of the downstream surface of the accelerator grid, using the three-dimensional particle simulation code for a background neutral density of $5 \times 10^{18} m^{-3}$, is shown in Fig. 4.8 (to aid in the visual interpretation, several actual cross-sections are shown together). The values shown are the total number of molybdenum atoms sputtered by xenon ions per area during the 5.5 microseconds of computation. In Fig. 4.8, the concentration of sputtering between grid apertures is clearly visible. The roughly triangular shape and orientation of these erosion contours are the same as shown in Figs. 4.6 (Patterson and Verhey 1990) and 4.7 (Rawlin 1988). As discussed in the next section **4.3.3.**, this pitted erosion pattern is the result of focusing of the charge exchange ions by the transverse electric field in the downstream deceleration region of the thruster. Although the assumed background neutral number density is certainly not as low as one would like to obtain in an ideal ground test (and is certainly significantly

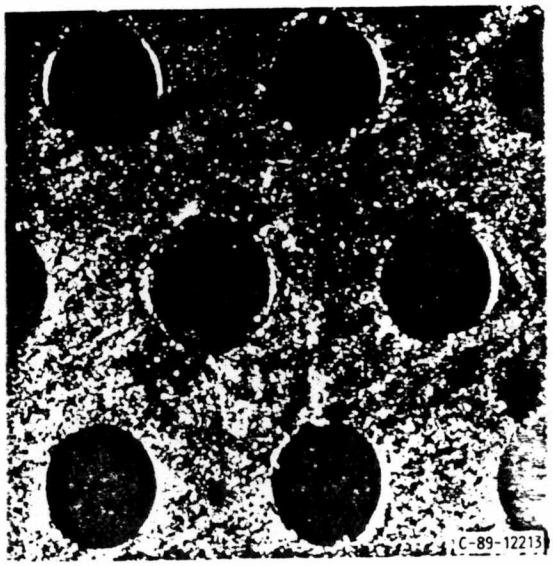

A) Upstream Surface, Pre-Lifetest.

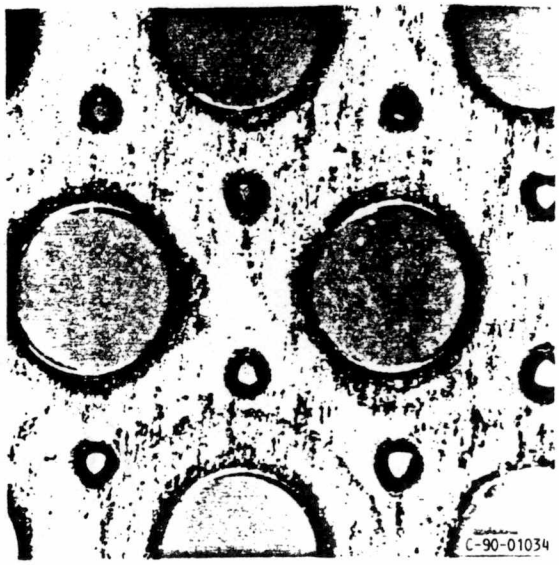

B) Upstream Surface, Post-Lifetest.

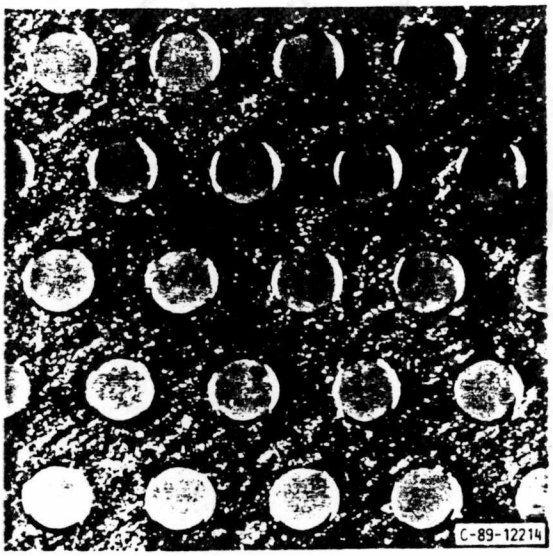

C) Downstream Surface, Pre-Lifetest.

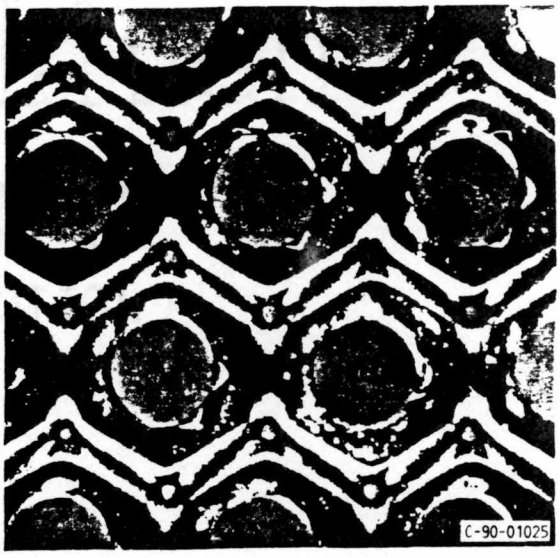

D) Downstream Surface, Post-Lifetest.

Figure 4.6. Experimentally observed grid erosion on the downstream surface of the accelerator grid, center holes (from Patterson and Verhey 1990).

(a) DOWNSTREAM SIDE, BEFORE TEST.

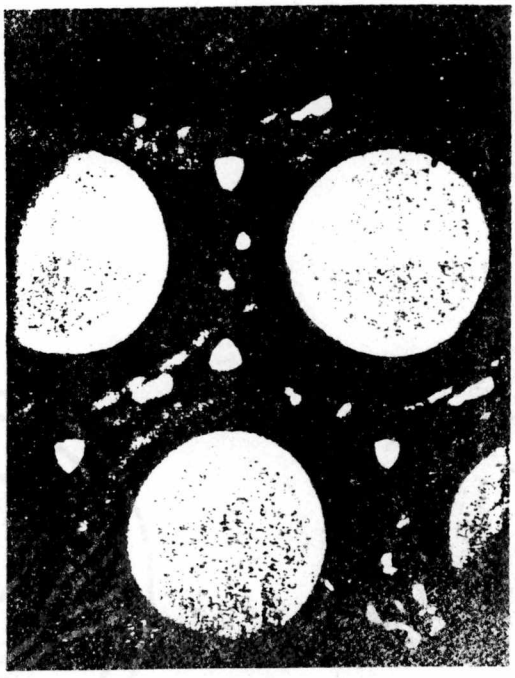

(b) DOWNSTREAM SIDE, AFTER TEST.

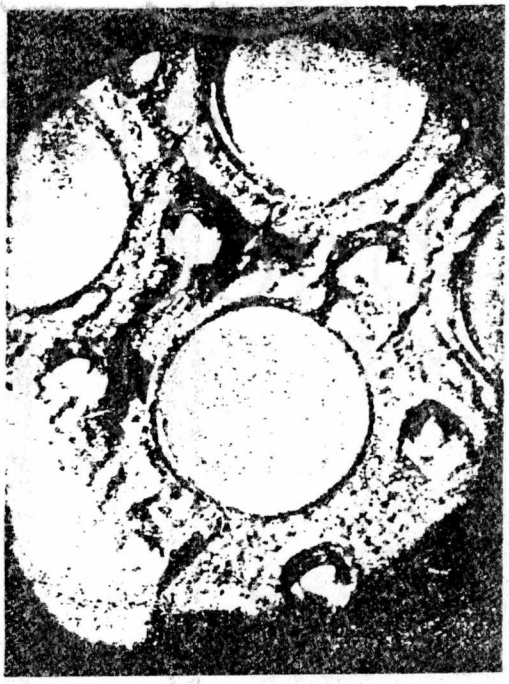

(c) UPSTREAM SIDE, AFTER TEST.

Figure 4.7. Experimentally observed grid erosion on the downstream surface of the accelerator grid, center holes (from Rawlin 1988).

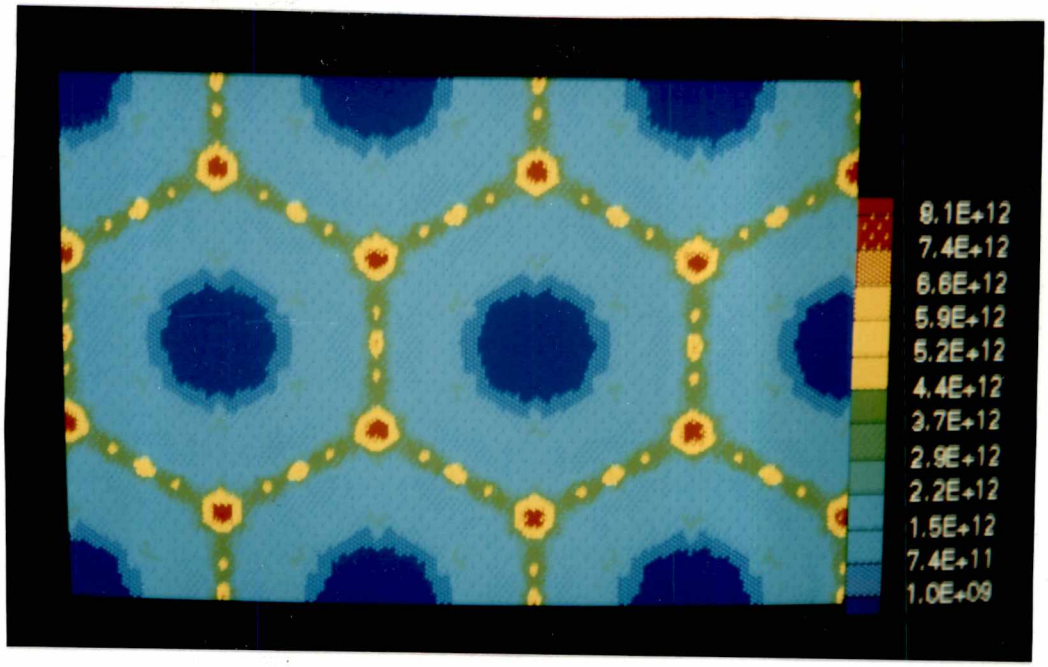

Figure 4.8. Calculated erosion contours on the downstream surface of the accelerator grid (values are number of atoms per square meter per 5.5 μsec). Note the concentration of sputtering between apertures.

higher than in an actual space application), it is still low enough that most charge exchange ions are created in the region far downstream from the accelerator grid. This clearly indicates that the highest sputtering erosion should take place on the downstream surface of the accelerator grid.

In addition to the erosion on the downstream side of the accelerator grid, a smaller amount of sputtering also occurs on the interior and the upstream surfaces of the accelerator grid.

A comparison with other numerical simulation of grid erosion was not possible since the author was unable to find any in the literature.

4.3.3. Calculated Transverse Electric Potential Contours

The electric potential contours at different transverse cross-sections along the thruster axis are shown in Fig. 4.9. To aid in the visual interpretation of these results, each of the following figures is a composite of six of the basic computational cross-sections (as shown in Fig. 2.3), arranged symmetrically around the geometric center of three adjacent apertures (thus, each of the three corners of the equilateral triangles constitutes one one-sixth of an aperture cross-section).

Fig.4.9a shows the potential contours 0.02 *mm* upstream from the screen grid. The electric potential gradient shown in this figure is focusing beam ions through the screen grid aperture. The typical electric potential contours inside the screen grid aperture is shown in Fig. 4.9b. It can be seen that the beam ions are continuously focused through the apertures and the potential gradient in the transverse direction at the screen grid is much greater than in the upstream region of the screen grid.

The transverse electric potential gradient changes its direction somewhere between the screen and accelerator grids. This is shown in the progression of Figs. 4.9c, 4.9d, and 4.9e proceeding from 0.3825 *mm*, 0.2550 *mm*, and 0.1275 *mm* upstream from the accelerator grid. In Fig. 4.9c, the electric potential gradient is about 378 Volts and tends to focus the beam ions toward the axis of the apertures. While the electric potential gradient shown in Fig. 4.9d still shows the tendency to force the ions toward the axis of the apertures, the potential gradient has dropped to about 91 Volts. The complete opposite electric potential gradient appears in Fig. 4.9e because it is closer to the accelerator grid and because of the existence of the positive ions. Therefore, the transverse electric field changes its direction from focusing to diverging the ion beams somewhere between the screen and accelerator

grids.

The typical electric potential contours inside the accelerator grid aperture is shown in Fig. 4.9f. The potential gradient does not show a very large value. Thus, if a charge exchange ion is created inside the aperture, it will not cause too much damage to the accelerator grid.

The transverse electric potential contours downstream region of the accelerator grid are shown in Figs. 4.9g — 4.9n. As shown in these figures, the downstream electric potential fields influence the performance of thrusters in two ways. First, the transverse electric potential tends to diverge the ion beams that decrease the axial velocity component and hence the thrust of the engine. Second, the effect on slow charge exchange ions by such electric fields is to accelerate these ions back upstream toward the grids and to focus them onto the geometric centers between apertures. This accounts for the pitted erosion spots that are observed to occur between apertures, and explains the sputtering erosion patterns observed in the experiments (Pawlik and Reader 1967, Rawlin 1988, and Patterson and Verhey 1990) for the downstream surface of the accelerator grid.

4.3.4. Comparisons of Two- and Three-Dimensional Models

Sputtering Erosion Rates

To do the comparison between two-dimensional and three-dimensional models, the same geometry and plasma conditions in Table 4.1 are used for both models. The only exception is that, to achieve the same open fractions, the outside diameter of the two-dimensional computational domain is 2.33 mm, whereas, in the three-dimensional calculation, the center-to-center distance between two adjacent apertures is 2.45 mm.

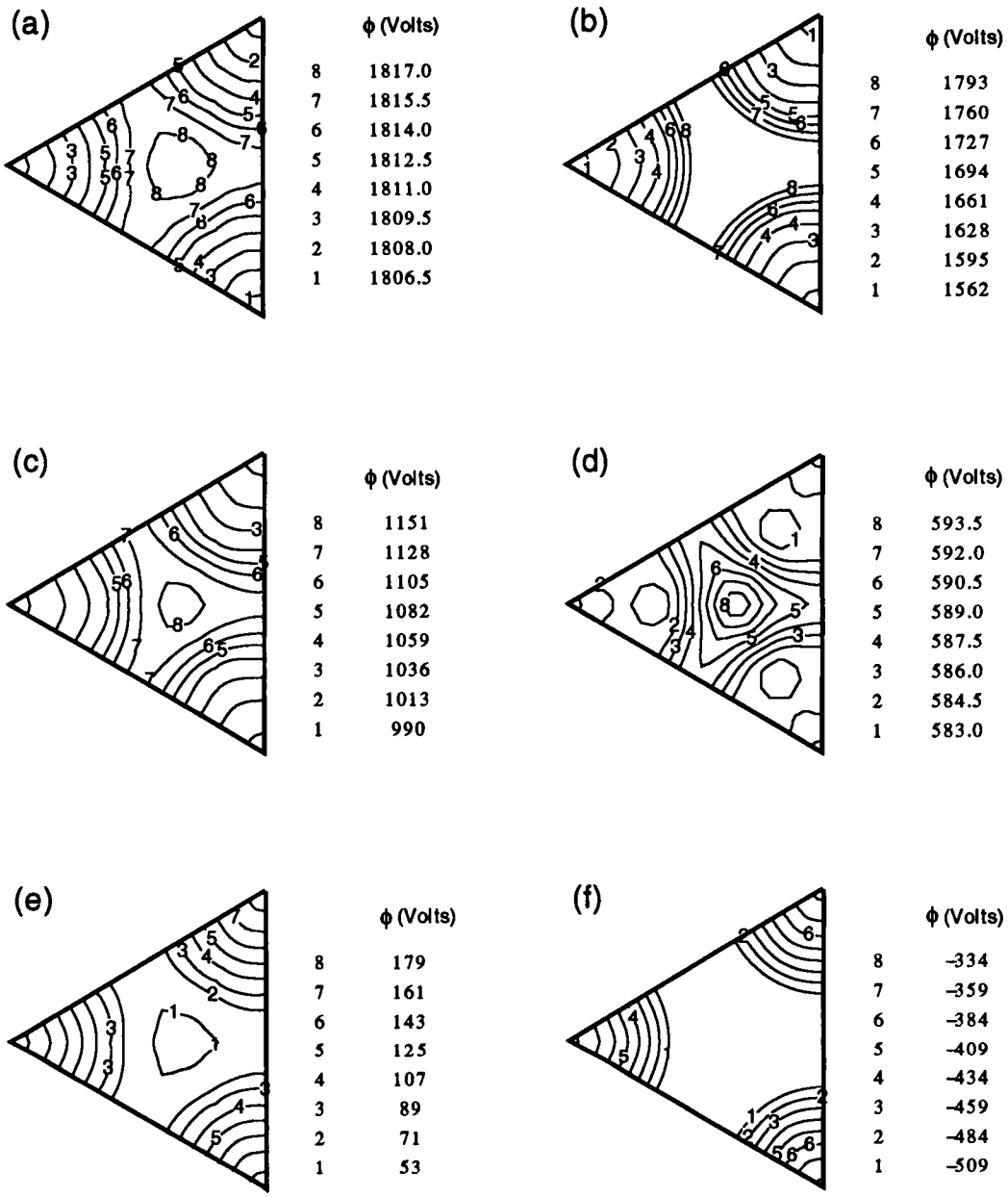

Figure 4.9. Transverse electric potential contours between accelerator grid apertures. (a) 0.02 *mm* upstream from the screen grid. (b) The middle way of the screen grid. (c) 0.75 *mm*, (d) 0.50 *mm*, and (e) 0.25 *mm* upstream from the accelerator grid. (f) The middle way of the accelerator grid.

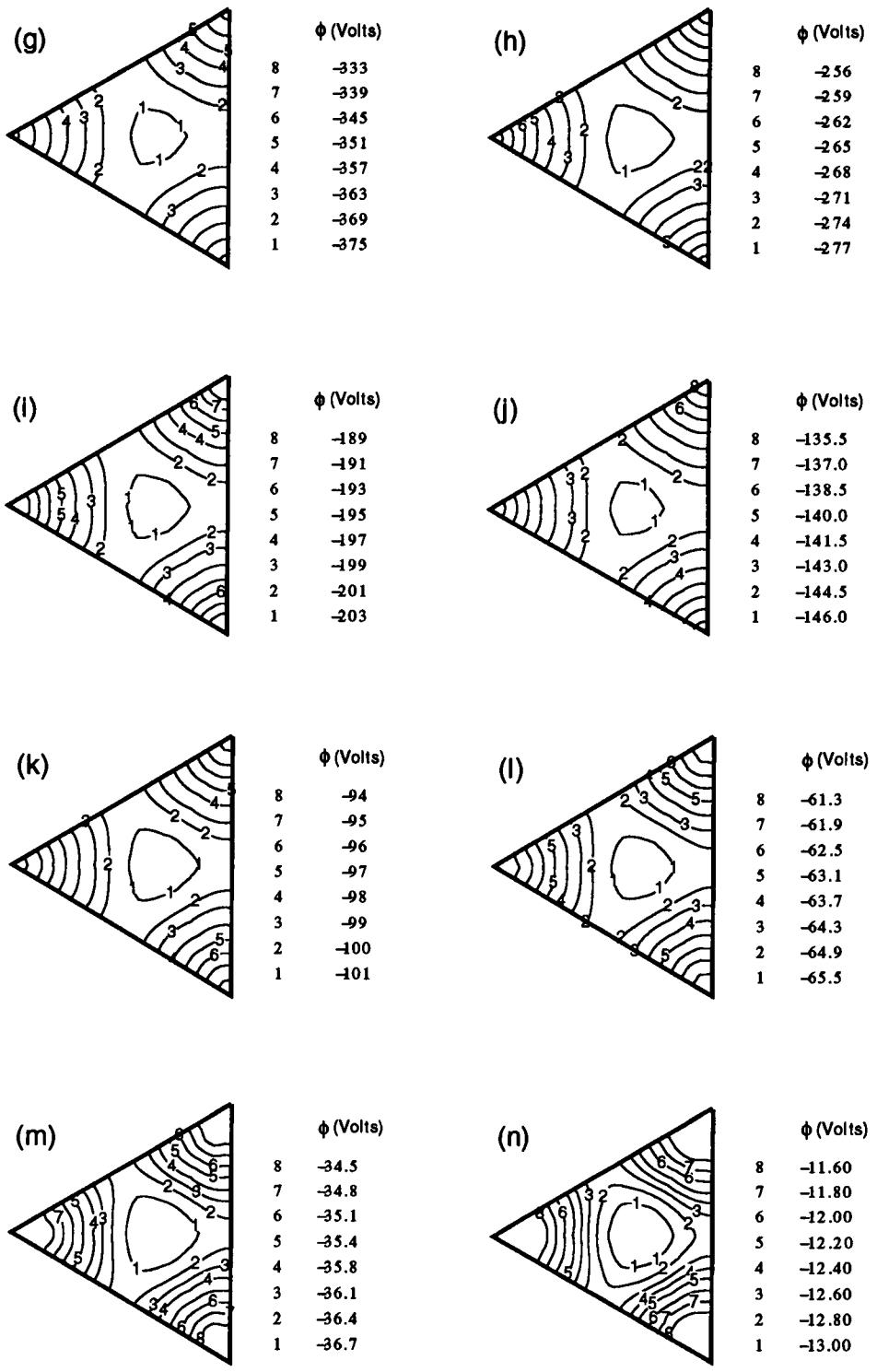

Figure 4.9. (continued). (g) 0.5 *mm*, (h) 1.0 *mm*, (i) 1.5 *mm*, (j) 2.0 *mm*, (k) 2.5 *mm*, (l) 3.0 *mm*, (m) 3.5 *mm*, and (n) 4.0 *mm* downstream from the accelerator grid.

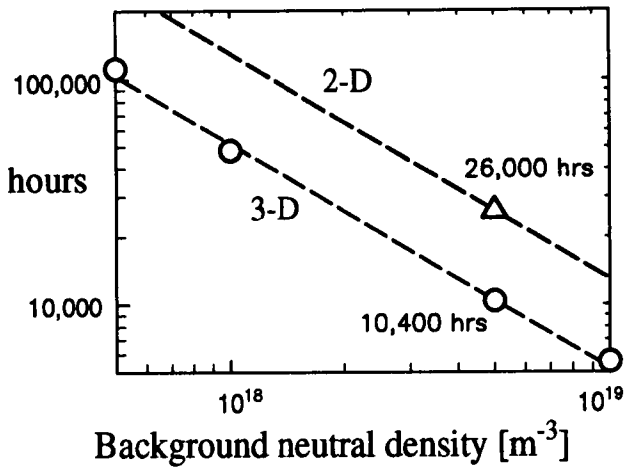

Figure 4.10. Wear-through lifetimes of the accelerator grid as a function of background neutral number density, for both the two- and three-dimensional models. The dashed lines indicate a pure inverse relationship.

For identical thruster operating conditions, both models predict about the same mass loss rate per accelerator grid aperture, 0.61 and 0.66 mg per 1000 hours of operation for the two-dimensional and three-dimensional models, respectively. In the three-dimensional model, the minimum wear-through time of the accelerator grid (which is calculated from the mass loss rate of the downstream surface assuming no geometry changes) is a factor of 2.5 shorter than in the two-dimensional model, namely 10,400 hours versus 26,000 hours. This shorter wear-through time is a direct reflection of the concentration of sputtering between grid apertures (pitting) calculated by the three-dimensional model.

Effect of Neutral Background Density

The effect of a varying background neutral density on the erosion rate was studied using both two-dimensional and three-dimensional models. Specifically, Fig. 4.10 shows the minimum wear-through time of the accelerator grid (obtained as explained above) for several values of this background neutral number density.

The straight, dashed lines in the figure represent simple inverse relationships between the lifetime and the neutral background density. For the three-dimensional data, this straight line is seen to fit the data well over the range of densities considered. Since the production of charge exchange ions is directly proportional to the neutral background density and the density of charge exchange ions is much smaller than that of the primary beam ions, a linear relationship between neutral density and background density is expected. However, it should be noted that one approximation made in the models is that of a constant background neutral density.

4.4. Conclusions for the Three-Dimensional Model

A fully three-dimensional, multi-aperture model is required to accurately account for the pitted erosion pattern observed in experiments. It has been explicitly shown how this pitted erosion pattern is a direct consequence of the transverse electric field distribution in the downstream region of the thruster. Because of this focusing of charge exchange ions in the three-dimensional model, the calculated wear-through lifetime of the accelerator grid is two to three times shorter than that predicted by the two-dimensional model.

CHAPTER V

SUMMARY AND RECOMMENDATIONS

5.1. Summary

Electrostatic ion thruster research in the United States has been conducted for more than 30 years. Ion propulsion, with specific impulse in the 2,000 to 10,000 sec range, appears to meet the needs of interplanetary missions and orbit transfer missions where fast delivery is not essential. Because the total mission time accomplished by ion propulsion is long, the engine lifetime is one of the critical issues for using ion propulsion. This lifetime issue has been addressed recently by the ground tests conducted at NASA Lewis Research Center (Patterson and Verhey 1990 and Rawlin 1988), is which it was demonstrated that the grid erosion due to charge exchange is the most likely limitation of ion engine lifetime.

Therefore, the motivation of the present study was to develop a numerical simulation model to obtain a better understanding of the mechanism of the charge exchange grid erosion. The three-dimensional model developed in this study has demonstrated the capability to predict the pitted sputtering erosion pattern of the accelerator grid which was observed in the experiments. This three-dimensional model has also explicitly shown that such a pitted sputtering erosion pattern is the direct reflection of the transverse electric field distribution in the downstream deceleration region of the thruster, which, in turn, is determined by the geometry of the hexagonal array of grid apertures.

During this study, a two-dimensional model was also developed to simulate a single set of apertures in an accelerator grid system. Although the two-dimensional model can not produce the pitted sputtering erosion pattern for a grid system consisting of an array of apertures with the usual hexagonal geometry, it can provide a qualitative description of the ion flow and the charge exchange collision processes. Besides, since the two-dimensional model requires less computer resources than the three-dimensional one, it is useful for a qualitative study of the accelerator system.

Two key simulation methods were used in both the two- and three- dimensional models. One is the particle-in-cell method which is used to simulate the ion flow. The other is the Monte Carlo method which is used to simulate the charge exchange collisions. This numerical particle simulation method has proven to be a powerful tool for the study of very low density ion thrusters.

5.2. Recommendations

The numerical model, based on the particle-in-cell and Monte Carlo techniques, has been shown to be capable of modeling the ion flow and the grid erosion in an ion engine, both qualitatively and quantitatively. However, several modifications to the code are suggested to obtain an improved understanding of the accelerator grid erosion.

Essentially, the charge exchange erosion pattern is determined by the electric field in the downstream region of the thruster. Thus, a more complete understanding of the neutralization process and, therefore, the downstream plasma conditions, would lead to a better model of the erosion process. This may require direct simulation of the downstream plasma. To simulate the plasma, electrons must be included in the model explicitly. Thus, the downstream plasma sheath

region, the interaction between ion beams and the downstream plasma, and the electric potential field inside the plasma would be simulated explicitly.

Similarly, direct simulation of the propellant neutral flow may provide more insight into what percentage of the sputtering yield is contributed by the neutral background residual atoms. In other words, a quantitative study of the accelerator grid erosion would be facilitated by a direct simulation of the neutral flow from the thruster. Since the ion thruster is a very low density device with Knudsen numbers that are usually greater than 10 the neutral flow can be simulated using the Direct Simulation Monte Carlo method (Bird 1976).

Finally, the upstream plasma sheath region could be simulated more carefully. Modeling this plasma sheath is a difficult problem as Bohm first recognized more than forty years ago. Application of the direct particle simulation approach to this problem, including simulation of both ions and electrons, might overcome many of the difficulties in modeling the plasma sheath.

BIBLIOGRAPHY

BIBLIOGRAPHY

Anderson, J. R., "The Divergence Characteristics of Constrained-Sheath Optics for Use with 5-eV Atomic Oxygen Sources," NASA Report CR-182238, Jan. 1989.

Aston, G., Kaufman, H. R., and Wilbur, P. J., "Ion Beam Divergence Characteristics of Two-Grid Accelerator Systems," *AIAA Journal*, Vol. 16, No. 5, May 1978, pp. 516–524.

Beattie, J. R., "A Model for Predicting the Wearout Lifetime of the LeRC/Hughes 30 cm Mercury Ion Thruster, " AIAA Paper 79-2079, October 1979.

Beattie, J. R., Matossian, J. N., and Robson, R. R. "Status of Xenon Ion Propulsion Technology," *Journal of Propulsion and Power*, Vol. 6, No. 2, 1990, pp. 145–150.

Bird, G. A., "Nonequilibrium Radiation During Re-entry at 10 km/sec," AIAA Paper 87-1543, 1987.

Bird, G. A., *Molecular Gas Dynamics*, Oxford University Press, London, 1976.

Birdsall, C. K. and Langdon, A. B., *Plasma Physics via Computer Simulation,* McGraw-Hill, New York, 1981.

Bohm, D., "Minimum Ionic Kinetic Energy for a Stable Sheath, " in The Characteristics of Electrical Discharges in Magnetic Fields, edited by A. Guthrie and R. K. Wakerling, McGraw-Hill, New York, 1949, pp. 77-86.

Bogart, C. D. and Richley, E. A., "A space-charge-flow computer program, " Lewis Research Center NASA TN D-3394, April, 1966.

Brewer, G. R., *Ion Propulsion*, Gordon and Breach, 1970.

Buneman, O., "Dissipation of Currents in Ionized Media, " *Phys. Rev.*, Vol. 115, pp. 503-517, 1959.

Carruth M. R., Jr. and Kuo, Y. S., "Ion Thruster Plume Effects on Spacecraft Surfaces," AIAA paper 80-1228, June 1980.

Dawson, J. M., "One-Dimensional Plasma Model, " *Phys. Fluids,* Vol. 5, pp. 445-459, 1962.

Eraslan, A. H., "A transient, Two-Dimensional Discrete-Element Model for Far-Field Analysis of Thermal Discharges in Coastal Regions, " Progress in Astronautics and Aeronautics, Vol. 36, 1975.

General Mill's Report, "Sputtering Yield Data in the 100-600 eV Energy Range," General Mills Report 2309, General Mills, Inc., Minneapolis, Minn., July 15, 1962; similar data may be found in Matsunami *et al.*, Nagoya Inst. of Plasma Physics, Report IPPJ-AM-32, 1983.

Hamza, V., "Numerical solution of axially symmetric Poisson equation: theory and application to ion thrustor analysis, " NASA TN D-1711, May, 1963.

Hamza, V. and Richley, E. A., "Numerical solution of two-dimensional Poisson equation: Theory and application to electrostatic-ion-engine analysis, " NASA Lewis Research Center TN D-1323, October 1962.

Hasted, J. B., *Physics of Atomic Collisions*, Butterworths, London, 1964, p. 416.

Hayakawa, Y., "Three Dimensional Analysis of Ion Beam Trajectories," AIAA Paper 90-2648, July 1990.

Hill, P. G. and Peterson, C. R., *Mechanics and Thermodynamics of Propulsion*, Addison-Wesley, 1965.

Hockney, R. W. and Eastwood, J. W., *Computer Simulation Using Particles*, Adam Hilger, Bristol and New York, 1989.

Hollway, D. L., "An electrolytic-tank equipment for the determination of electron trajectories, potential and gradient, "I.E.E. Proc. **103**, 155-160, Paper 1837 M, March, 1965.

Hyman J., Jr. *et al.*, "Formation of Ion Beams from Plasma Sources: Part I," *AIAA Journal*, Vol. 2, No. 10, Oct. 1964, pp. 1739–1748.

Kaufman, H. R., "Accelerator-System Solutions for Broad-Beam Ion Sources," *AIAA Journal*, Vol. 15, No. 7, July 1977, pp. 1025–1034.

Kaufman, H. R., "Performance Correlation for Electron-Bombardment Ion Sources, " NASA TN D-3041, 1965.

Kaufman, H. R. and Robinson, R. S., "Low Specific Impulse Electric Thrusters," NASA CR-174678, July, 1984.

Kerslake, W. R., "Charge-Exchange Effects on the Accelerator Impingement of an Electron-Bombardment Ion Rocket," NASA TN D-1757, May 1963.

Kerslake, W. R., "Accelerator Grid Tests of an Electron-Bombardment Ion Rocket," NASA TN D-1168, Feb. 1962.

Kerslake, W. R. and Pawlik, E. V., "Additional Studies of Screen and Accelerator Grids for Electron-Bombardment Ion Thrusters, " NASA TN D-1411, 1963.

King, H. J., Eckardt, W. O., Ward, J. W., and Knechtli, R. C., "Electron-Bombardment Thrusters Using Liquid-Mercury Cathode, " *J. Spacecraft and Rockets* 4, 599, May 1967.

Kirstein, P. T. and Hornsby, J. S., "A Fortran program for the numerical analysis of curvilinear electrode systems with an emitting surface, " Center of European Nuclear Research Rept. 63-16, 1963.

Lathem, W. C., "Ion Accelerator Designs for Kaufman Thrusters, " AIAA Paper 69-261, March 1969.

Lathem, W. C., "A New Technique for Simulating Space-Charge Potential Distributions, " *J. Spacecraft and Rockets*, Vol. 5, No. 6, pp. 737-738, June 1968a.

Lathem, W. C., "Approximate Analysis of the Effects of Electrode Misalinements on Thrust Vector Control in Kaufman Thrusters, " AIAA Paper 68-89, Jan. 1968b.

Loukochkov, V. S., "Electrolytic tank with current leading elements for studying space charge distribution in electron tubes," LeVide **11**, 328-337, September-October, 1956.

MacRae, G. S. and Mercer, C. R., "Laser Interferometric Measurement of Ion Electrode Shape and Charge Exchange Erosion, " AIAA Paper 91-2121.

Maloy, J. E., Poeschel, R. L., and Dulgeroff, C. R., "Characteristics of 30-centimeter Mercury Ion Thrusters, " NASA TM-81706, April 1981.

Mickelson W. R. and Kaufman, H. R., "Status of Electrostatic Thrusters for Space Propulsion," NASA TN D-2172, May 1964.

Oates, G. C., *Aerothermodynamics of Gas Turbine and Rocket Propulsion*, AIAA Education Series, 1984

Patankar, S. V., *Numerical Heat Transfer and Fluid Flow*, Hemisphere, 1980.

Patterson, M. J., "Performance Characteristics of Ring-Cusp Thrusters with Xenon Propellant," AIAA Paper 86-1392, June 1986.

Patterson, M. J. and Verhey, T. R., "5kW Xenon Ion Thruster Lifetest, " AIAA Paper 90-2543, July 1990.

Pawlik, E. V., Margosian P. M., and Staggs, J. F., "A Technique for Obtaining Plasma-Sheath Configurations and Ion Optics for an Electron-Bombardment Ion Thruster," NASA TN D-2804, May 1965.

Pawlik, E. V. and Reader, P. D., "Accelerator grid durability tests of mercury electro-bombardment ion thrusters, " NASA TN D-4054, July 1967.

Peng, X., Keefer, D., and Ruyten, W. M.,"Plasma Particle Simulation of Electrostatic Ion Thrusters," AIAA paper 90-2647, July 1990.

Peng, X., Ruyten, W. M., and Keefer, D., "Plasma Particle Simulation of Electrostatic Ion Thrusters," *AIAA Journal of Propulsion and Power*, Vol. 6, No. 6, November/December 1991a, to be published.

Peng, X., Ruyten, W. M., and Keefer, D., "Three-dimensional particle simulation of grid erosion in ion thrusters," Paper 91-119, 22nd International Electric Propulsion Conference, Viareggio, Italy, October 14-17, 1991b.

Peng, X., Ruyten, W. M., and Keefer, D., "Comparison of 2-D and 3-D Models of Grid Erosion in an Ion Thruster," AIAA paper 91-2120, June 1991c.

Peng, X., Ruyten, W. M., and Keefer, D., "Monte Carlo Simulation of Ion-Neutral Charge Exchange Collisions and Grid Erosion in an Ion Thruster," AIAA paper 91-0607, Jan. 1991d.

Rawlin, V. K., "Internal Erosion Rates of a 10-kW Xenon Ion Thruster, " AIAA Paper 88-2912, July 1988.

Rawlin, V. K. and Mantenieks, M. A., "Effect of Facility Background Gases on Internal Erosion of the 30 cm Hg Ion Thruster, " AIAA Paper 78-665.

Rawlin, V. K. and Patterson, M. J., "Performance of 30 cm Xenon Ion Thrusters, " AIAA-85-2009, Sept. 1985.

Reynolds, T. W., "Procedure for Estimating Effects of Ion Beam Interaction with Spacecraft," NASA TM X-68043, April 1972.

Ruyten, W. M., private communication, 1989.

Skullerud, H. R., "The Stochastic Computer Simulation of Ion Motion in a Gas Subjected to a Constant Electric Field," *Brit. J. Appl. Phys. (J. Phys. D)*, Ser. 2, Vol. 1, p. 1567, 1968.

Staggs, J. F., "An electrolytic tank analog for two-dimensional analysis of electrostatic-thruster optics, "NASA TN D-2803, May, 1965.

Staggs, J. F., Gula, W. P., and Kerslake, W. R., "The Distribution of Neutral Atoms and Charge-Exchange Ions Downstream of an Ion Thruster," AIAA Paper 67-82, Jan. 1967.

Staggs, J. F., Richley, E. A., and Gula, W. P., "Ion Extractor System Design, " *AIAA Journal*, Vol. 5, No. 2 Feb. 1967, pp. 359-360.

Van Duzer, T. and Brewer, G. R., "Space charge simulation in an electrolytic tank, " J. Appl. Phys. *30*, 291-301, March, 1959.

Wilbur, P. J., "Advanced Electric Propulsion Research," NASA Annual Report CR-185237, April 1990, p. 11.

Winslow, A. M., "Numerical Solution of the Quasilinear Poisson Equation in a Nonuniform Triangle Mesh, " *J. Computational Physics, 2*, 149-172, 1967.

VITA

Xiaohang (Jeff) Peng was born in Tianjing, China on November 10, 1959. He attended elementary and high schools in Beijing, China. In July 1982 he graduated from The Tsinghua University, Beijing, China, where he received the Bachelor of Science degree in Nuclear Engineering. In August 1982, he entered the graduate school of the Academia Sinica, China, where he received the degree of Master of Science in Mechanical Engineering in 1985.

In September 1985, he came to The University of Tennessee Space Institute as a graduate research assistant. While working towards the Ph.D., he received his second Master of Science degree in Mechanical Engineering in August, 1985. This dissertation work was carried out in pursuit of a Doctor of Philosophy degree in Mechanical Engineering, and was completed in November 1991.

He began to work for The University of Tennessee–Calspan Center for Space Transportation and Applied Research as a research engineer in September 1991.

He was married to Quan Zhang in August, 1985, and has a three-and-a-half year old daughter, Barbara Mong-Mong, and a one year old son, Aaron Yuan.